MASTER ERASMUS MUNDUS
QUALITY IN ANALYTICAL LABORATORIES

MAGNETIC NANOPARTICLES FOR

BIOSENSING AND IMMUNOPRECIPITATION

Research Master Thesis

By QFB. Christian Hazael Pérez Beltrán

Supervised by:

Dr. José María Palacios Santander

Dra. Ana María dos Santos Rosa Da Costa

ABSTRACT

Our world is rapidly changing and its future is on our hands. Great effort is being done against overexploitation of natural resources, uncontrolled hunting and pollution. A great concerning fact is due to pollution which is causing a continuous greenhouse effect and new cancer cases every single day. Nowadays, it is possible to improve the detection of lethal elements in the environment, to fight against cancer in a smarter manner, with less pain and with more efficiency but, more important, to use the same low-cost, fast and environmentally friendly tool for these purposes and more. This reality is thanks to previous works and findings regarding the Magnetic Nanoparticles (MNPs), which are employable in a wide variety of applications such as magnetic recording media, resonance imaging, heavy metals ions removal and biomedicine (specifically in the hyperthermic treatment of malignant cells, site-specific drug delivery and separation of proteins and cell population). MNPs have special properties such as superparamagnetic, high field irreversibility, high saturation field, extra anisotropy contributions or shifted loops after field cooling, biocompatibility, long durability, low toxicity and cost.

In this context, this project intends 1) to develop through a novel synthesis method, a biosensor capable to detect mercury in water by irreversible inhibition of the enzyme Horseradish Peroxidase attached onto the surface of different coated MNPs being able to approximate its detections to those limits stablished by the Environmental Protecting Agency of the United States of America; and 2) to use these high valuable nanoparticles as an immunoprecipitation vehicle through the attachment of a polyclonal antibody onto the surface of functionalized MNPs, selective against a suppressor protein.

MNPs of about 10 nm were obtained within one minute via co-precipitation method enhanced by high power ultrasound. Experimental design has been used in order to optimize the preparation process from hours to just one minute.
The composition, structure, size and morphology analyses of these MNPs have been carried out through X-ray diffraction, Fourier transform infrared spectroscopy, thermogravimetric analysis and scanning electron microscopy showing the correct achievement of the MNPs. Moreover, different coating agents have been tested in order to functionalize MNPs surface with the aim of attaching later biomolecules, such as enzymes and antibodies.

Key words: *Magnetic Nanoparticles (MNPs), Environmental Control, Biosensor, Irreversible Inhibition, Biomedicine, Immunoprecipitation, Sonocatalysis, Green Analytical Chemistry, Design of experiments.*

DECLARATION

Dr. José María Palacios Santander
Department of Analytical Chemistry
University of Cádiz, Spain.

and

Dra. AnaMaría dos Santos Rosa da Costa
Department of Chemistry and Pharmacy
Faculty of Science and Technology
University of Algarve, Portugal

Declare:

That the present work entitled **"Application of Magnetic Nanoparticles for biosensing and immunoprecipitation"** has been performed by Christian Hazael Pérez Beltrán at the laboratories of the Department of the Analytical Chemistry of the University of Cadiz, Spain, and those of the Department of Chemistry and Pharmacy of the University of Algarve, Portugal, under our supervision. Consequently, we confirm the high quality of this work in order to be submitted for its defense authorizing its dissemination.

Faro, Portugal, September 2019

Dr. José María Palacios Santander	*Dra. Ana María dos Santos Rosa da Costa*
Name of supervisor	Name of supervisor

ACKNOWLEDGMENTS

"It is not joy that makes us grateful; it is gratitude that makes us joyful", David Steinall. In this regard, it makes me truly glad being able to thank God for blessing and giving me the wellness day after day in order to conclude this work; and also for making me coincide with admirable and awesome people who supported me throughout this incredible experience; since the EMQAL consortium to my classmates and professors of the master, to whom I extend my deepest and sincere gratitude and thanks.

In first place I would like to express my appreciation to two remarkable persons, **Dr. José Maria Palacios Santander** and **Dra. Ana Maria dos Santos Rosa da Costa**, who constantly guided, supervised, supported and helped me, whose teachings and insights helped me to become a more critic person learning to see the whole picture. Your human kindness is what I admire the most from you. Thank you!

I also recognize the support provided by **Dr. Miguel Palma Lovillo** all along the entire master course to deal with the bureaucratic processes, whose selfless aid gave me a valuable lesson of helping others without expecting anything in return.

A very important part of this work was the people within the different departments, those from the Department of Analytical Chemistry from the University of Cádiz, from the Institute of Science and Technology of materials from University of Habana, the people from the Department of Biomedical Sciences and Medicine from the University of Algarve, especially **Dr. Juan José García Guzmán, Dr. David López Iglesias** from UCA, **Dr. Osvaldo L. Estévez Hernández** from UH and **Dra. Bibiana Ferreira** from UAlg. Thanks for your time, patience and teachings but more than that, for the willingness you had to share your experience in the best possible manner. There were a lot of people involved during this research that mentioning all of them will be an entire chapter, I sincerely apologize but I want to let you know that I will always keep you all in my heart.

I must thank to my home institution the **University Autonomous of Sinaloa**, to its current Rector, **Dr. Juan Eulogio Guerra Liera** and all the people involved, for trusting and giving me the opportunity to experience this lifetime adventure which would not have been possible without the provided economic support.

Special thanks to **Ma. Fernanda Meza Araujo**, my best friend and wife whose moral support, comprehension and sacrifices during the good and difficult times throughout this experience meant a lot to me. Everything was easier with you by my side.

And last, but not least, I want to express my thankfulness to my parents **IBQ Filomeno Pérez Pérez** and **Dra. Rosario Beltrán Ruiz.** Without your help this adventure would not have been possible. Thank you for your words when I needed, thank you for everything.

Sincerely, from the bottom of my heart, thank you all. You were a key factor in the development of this work.

INDEX

Figure Index

1. Introduction

Overview

Since 2005 Nanoscience and Nanotechnology were predicted to have a huge and important impact in all aspects of our lives[1]. Nowadays this prediction became a reality and marked the beginning of a new era. They are changing our lifestyle in the fields of energy, food, electronics, textile, agriculture, cosmetics, environment, medicine, construction, engineering, transport and telecommunications[2].

Nanoscience can be defined as the study of materials in the nanometer scale which is commonly considered to be a size below one micrometer; on the other hand nanotechnology refers to a multidisciplinary field that aims the production, manipulation, use and characterization of nanomaterials[3], which are defined by the National Science Foundation and the National Nanotechnology Initiative (NNI) as, all types of materials found at the nanoscale with a unit size ranging from 1 to 100 nm, in which, unique optic, magnetic, electronic and structural characteristics are generated[4]. Some examples of nano-sized structures are nanorods, nanowires, nanotubes, nanobelts, nanoribbons, nanofibers, quantum dots, hollow spheres and nanoparticles[4–8] as shown in **Figure 1**.
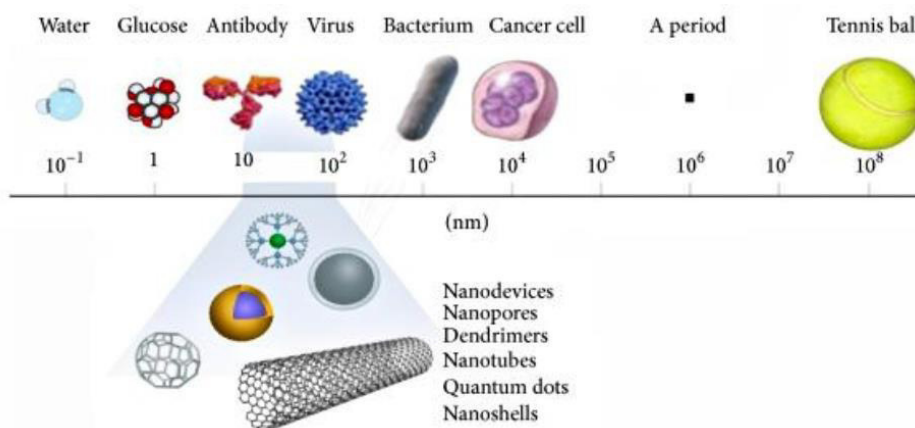
Figure 1. Size comparison in the nanometric scale.

All of these nanosized structures can be naturally occurring or chemically, mechanically, physically, and biologically synthesized. Regarding their chemical composition, they can be classified into various categories such as: metal-based materials, metal oxide nanomaterials, carbon-based nanomaterials, dendrimers, quantum dots and nanocomposites.[9]

Among all these different nanostructures and chemical compositions there are some specific metal oxide nanoparticles which are grabbing a lot of attention nowadays, they are called Magnetic Nanoparticles (MNPs).

A fundamental aspect of such MNPs, which is crucial for their proper applicability, is their synthesis. This step is considered as the most important one, for the reason that the characteristics of MNPs are directly related to the methods of synthesis due to the different sort of variables involved in each of them. There are several conventional methods reported on the literature for MNPs, however they are being replaced or enhanced by novel techniques, as is the case of the co-precipitation method boosted by high power ultrasound. This is a powerful technique capable of drastically reducing the synthesis time from hours to just minutes and consequently it reduces the applied energy and costs. Due to these facts and to the reduction in the use of solvents, high power ultrasound is recognized as an environmentally friendly technique.

MNPs have been already employed in electrochemical biosensors as nanosized supports for the immobilization of analytical biomolecules[10]. The immobilization of enzymes on the surface of these nanoparticles offers numerous advantages including enhancement of the enzymatic activity and reduction of the mass-transfer processes associated with the recognition of substrates by enzymes. MNPs also provide a favorable microenvironment for electrochemical devices where enzymes may exchange electrons directly with the transducer, improving the sensitivity and selectivity of electrochemical biosensors.

Thus, considering the potential advantages of such biosensors using MNPs with specific enzymes attached onto them, dangerous heavy metals can be detected in waters. Mercury even at small concentrations is lethal for living beings and highly risky for the environment, since it affects the central nervous system, kidney and livers; it can be easily accumulated into the surface and ground water but hardly removable from them. In this regard, mercury must not be found in any kind of waters above its maximum allowable limit of 2ppb or 2µg/L stablished by the Environmental Protection Agency (EPA)[11].

Not only do heavy metals induce the malfunction of organs, but also cause cancer due to long-term exposure. During cancer progression, transcription factors (TP) which are responsible for some vital processes of cells are inactivated. This inactivation is typically performed by phosphorylation by a number of protein kinases (e.g., protein

kinase B (PKB or AKT), IkB kinase (IKK), and dual-specificity tyrosine phosphorylation-regulated kinases (DYRK)).

TP activity can also be affected by modification including deacetylation and ubiquitination where *tribbles* (TRIB) pseudokinases act as modulators of substrate ubiquitination[12–14].

Nowadays, efforts are being done to develop TRIB2 as a biomarker in order to detect the presence and progression of human melanoma with specific antibodies. With nanoparticles help, antibodies, drugs, enzymes or nucleotides can be bounded onto their surface and guided to an organ, tissue, or tumor using an external magnetic field[15,16].

As a result of the up growing importance of these topics, the present study aims to obtain MNPs through the conventional co-precipitation method assisted by high power ultrasound and to utilize them for bio-sensing and immunoprecipitation.

In order to ensure the achievement of these aims, specific objectives were stablished:

1. To synthesize MNPs by two methods: (A) conventional co-precipitation method assisted with high power ultrasound, and (B) co-precipitation from partially reduced ferric chloride aqueous solutions.
2. To find out the best synthesis conditions for method (A) through the experimental design in order to get desirable sizes.
3. To functionalize the optimized MNPs with different coating agents.
4. To characterize the optimized and functionalized MNPs.
5. To apply these MNPs in order to detect mercury in waters through enzyme irreversible inhibition.
6. To coat the MNPs with a polyclonal antibody against human TRIB2 protein.
7. To try these MNPs as a proof of concept experiment as immunoprecipitation agents against TRIB2 protein from lysates obtained from cells overexpressing it.

1.1. Magnetic nanoparticles (MNPs)

MNPs or also called magnetic iron oxides have been studied widely for more than thirty years, since their very first synthesis performed by Massart on 1981[17]. Nevertheless, it was from the last decade when MNPs started to gain more attention directly related with nanotechnology, and in consequence, their uses have increased exponentially due to their very unique physical and chemical properties such as superparamagnetism, high field irreversibility, high saturation field, extra anisotropy contributions or shifted loops after field cooling, their biocompatibility, long durability, low toxicity and low cost[18–20]. These properties depend on the size of the particles, their morphology and the structure of the material.

All these characteristics have been considered for different applications such as magnetic recording media[21], ferro fluids[22], magnetic resonance imaging[23,24], heavy metals ions removal[25], and biomedicine (specifically in the hyperthermic treatment of malignant cells[26], site-specific drug delivery[27] and separation of proteins and cell population[28]).

MNPs can either occur naturally or be synthetically produced, but nowadays MNPs are mainly obtained through different sort of synthetic methods. Within the employed techniques for their synthesis, the most common are chemical vapor deposition[29], thermal oxidation[30], polyol process[31], hydrothermal[32], solvothermal[33] methods and iron salts co-precipitation[34,35].

The conventional co-precipitation method without stabilizers was first described by Massart[17] and involves the use of iron salts in a molar ratio of 2 Fe^{3+} to 1 Fe^{2+}; these precursors might be $FeCl_2$, $FeCl_3$, $Fe_2(SO_4)_3$, $FeSO_4$, $Fe(NO_3)_3$[36] and should be mixed in alkaline aqueous solution under nitrogen atmosphere and continuous stirring at 80°C. The chemical reaction that takes place in this system is the next one:

$$Fe^{2+} + Fe^{3+} \, 8OH^- \rightarrow Fe_3O_4 + 4H_2O \qquad \textbf{(1)}$$
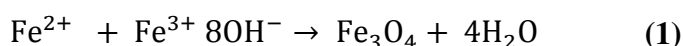
This method is the most common route for magnetite production due to its simplicity and efficiency; nevertheless it presents some drawbacks or difficulties such as: 1) the particle size control, 2) broad size distribution, 3) time consuming and 4) the resultant mixture of nanoparticle phases, which could be ferrihydrite, akagenite (FeOOH), Fe(OH), hematite or maghemite[37–40].

Due to these problems, novel procedures are being developed in order to overcome these difficulties.

1.2. Sonochemistry

Sonochemistry is defined as the use of ultrasound power with frequencies between 20 kHz and 2 MHz to provide chemical, thermal and physical effects in solution[41]; these different frequencies are applied through an ultrasound probe that lead to different properties in the liquid. Thus, the proper selection of the frequency range will be done depending on the final objective. Low frequencies (20–80 kHz) lead to physical effects such as micro convection, shock-waves, and microjects, among others; meanwhile high frequencies (150–2000 kHz) promote chemical effects and the formation of hydroxyl radical species.

So, putting in contact a medium with ultrasound power is a synonym of having enhanced physico-chemical effects such as the increase in kinetics of chemicals reactions, changes in reaction mechanisms, emulsification effects, crystallization, precipitation, etc[42,43].

Talking about ultrasound power is talking about frequencies producing ultrasound waves which originate the acoustic cavitation phenomenon and is responsible for all these generated effects. During the decompression phase of these power ultrasound waves, the molecules of a liquid might be affected by forces strong enough to destabilize Van Der Waals interactions and separate them from each other. Right after, some very small cavities are formed in the medium, these cavities tend to expand until the pressure is low enough to support their growth. At this stage any component of the reaction mixture may evaporate into the void and reduce the negative pressure bias between the interior of the cavity and the surrounding liquid. After some compression and decompression cycles, the cavity can be sustained by vapors and convert into a bubble with a life time enough to reach macroscopic dimensions, or implode violently instead, producing hot spots with extreme conditions of temperature (>5000 K) and pressure (>1000 atm) with a really fast cooling rate of 10^{10} K·s^{-1} [44–46].

Through using the sonochemical approach and taking advantage of these exceptional conditions, a variety of new and unusual nanostructured materials, inaccessible by conventional methods can be obtained; for instance a more uniform size distribution can be achieved, as well as nanoparticles with higher surface area and improve phase purity.

This is the reason why high frequency ultrasound has gained much attraction for many applications[41], especially in the sonochemical syntheses, where several green successful examples have been reported[47–51] with a low economic and time expense[52,53] as shown in **Figure 2**[54].
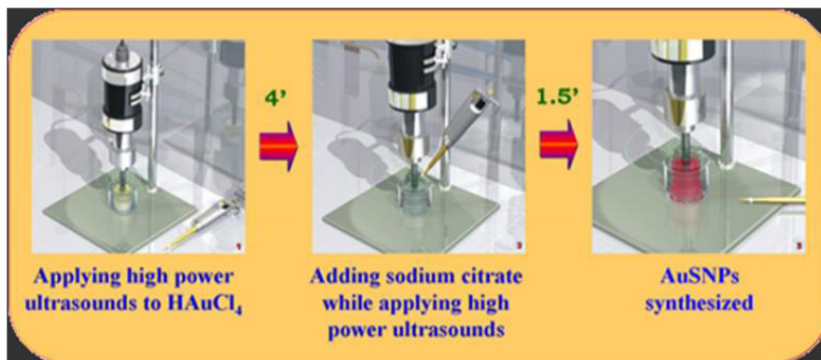
Figure 2. Sonochemical synthesis of nanoparticles

1.3. Green Analytical Chemistry

Since the introduction of the "green chemistry" concept, around the 90's by Paul T. Anastas defined as the design of chemical products and processes that reduce or eliminate the use and generation of hazardous substances[55], this idea has gained a lot of importance and has become a transversal topic in all the fields of chemistry, such as organic, pharmaceutic, clinical or analytical, where consciousness about taking care of the environment and green methods that fulfill the 12 principles of Green Analytical Chemistry (**Table 1**) have been created [56].

1	S	Select direct analytical technique.
2	I	Integrate analytical processes and operations.
3	G	Generate as little waste as possible and treat it properly.
4	N	Never waste energy.
5	I	Implement automation and miniaturization of methods.
6	F	Favor reagents obtained from renewable source.
7	I	Increase safety for operator.
8	C	Carry out *in situ* measurements.
9	A	Avoid derivatization.
10	N	Note that the sample number and size should be minimal.
11	C	Choose multi-analyte or multiparameter method.
12	E	Eliminate or replace toxic reagents.

Table 1. Twelve principles of Green Analytical Chemistry.

Sonochemical synthesis of nanoparticles is considered as a green approach due to: 1) the reduction of the use of non-green solvents during the sample preparation; 2) the amount of reagents is drastically reduced during the synthesis; 3) the minimization of the consumed energy; 4) the safety of the method and 5) for being environmentally friendly producing small quantities of residues [56,57]. Thus as a result of the huge impact of green chemistry and all these advantages of sonochemical synthesis, several studies have been successfully reported [8,54,58–61].

1.4. Functionalization of MNPs

The functionalization of the iron oxide nanoparticles is crucial to obtain magnetic colloidal ferrofluids that are stable against aggregation in both biological medium and a magnetic field. The stability of a magnetic colloidal suspension results from the equilibrium between attractive and repulsive forces. Theoretically, four kinds of forces can contribute to the interparticle potential in the system: Van der Waals forces, electrostatic repulsive forces, magnetic dipolar forces and steric repulsion forces[62].

Developing coating strategies, chemically improves the stability of the magnetic nanoparticles. The nature of the coating has to be optimized to simplify the process and to effectively prevent any aggregation and sedimentation of the superparamagnetic nanoparticles. The surface of MNPs can be stabilized in an aqueous dispersion by the adsorption of different coating agents such as polymers (e.g. polydopamine and chitosan), carboxylic acids (e.g. citric acid, isonipecotic acid and 3-mercaptopropionic acid), phosphates (e.g. dihexadecyl phosphate, polyvinylalcohol phosphate(PVAP)) among many others[63]. The coating agents must be chosen according to the final application of the MNPs.

Dopamine (DA) is a catecholamine neurotransmitter related to many physiological processes and neurophysiological disorders such as schizophrenia, Parkinson's and Alzheimer's diseases, as well as several social and addiction behaviors[64,65].

In addition to its biomedical relevance, DA has been recently proposed as a novel organic coating material. DA can be self-polymerized **(Figure 3)** in aerated basic solutions, forming an adherent poly(dopamine) (PDA) film over a wide variety of organic and inorganic surfaces[66,67]. The reactive quinones at the surface of PDA films could be used as anchoring points for further chemical modification and/or immobilization of biologically active macromolecules (antibodies, enzymes, etc.)[66].
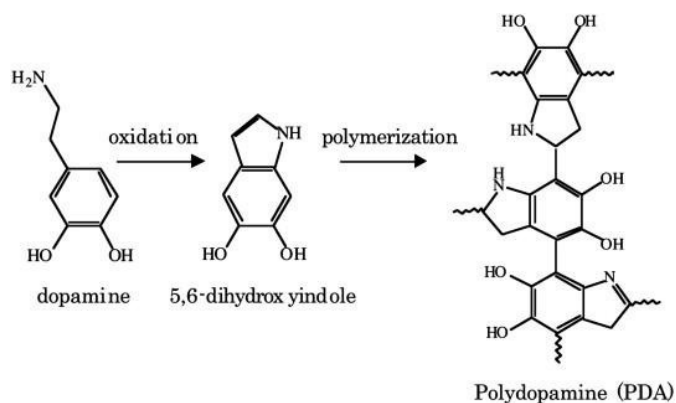
Figure 3. Self-polymerization of Dopamine

Chitosan is a nontoxic, alkaline and hydrophilic copolymer of *N*-acetyl-glucosamine and glucosamine units linked by β-(1,4)-glycosidic bonds (**Figure 4**), and has good biocompatibility, biodegradability, mucoadhesivity and low toxicity.

Chitosan has three types of reactive functional groups, which are amino groups, primary and secondary hydroxyl groups at the C-2, C-3, and C-6 positions, respectively. These groups allow a variety of chemical modifications of chitosan that include, among others, acylation, *N*-phthaloylation, tosylation, reductive alkylation, *O*-carboxymethylation, *N*-carboxyalkylation, silylation and graft copolymerization[68].
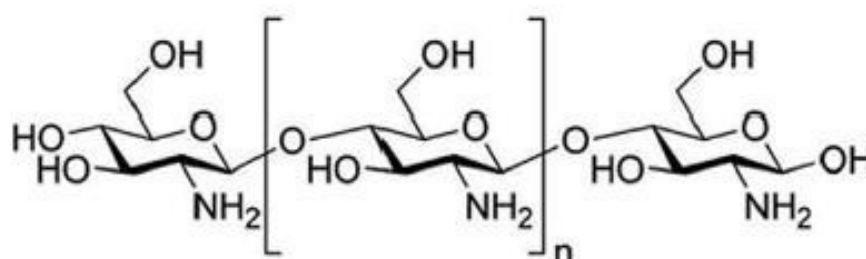
Figure 4. Chemical structure of chitosan

Carboxylic acids (**Figure 5**) are organic compounds containing a highly polar functional group (carboxyl (COOH))[69]. They are of crucial importance to develop stable MNPs under physiological conditions (blood pH≈7.2-7.4, salt concentration≈0.15M)[70] to be used in biomedicine.

Carboxylates may be adsorbed on the surface of the MNPs by coordinating via the carboxylate functionality. In the case of polycarboxylic acids, such as citric acid, coordination via
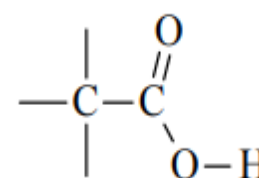
Figure 5. Chemical structure of a carboxylic acid.

one or two of the carboxylate functionalities may occur, depending upon steric necessity and the curvature of the surface. This leaves at least one carboxylic acid group exposed to the solvent, which should be responsible for making the surface hydrophilic and negatively charged[62]. Nonetheless, there are compounds with only one of these functional groups (e.g. isonipecotic and mercaptopronionic acid) which, depending on the final purpose, it is desired to leave it free in order to further attach other molecules to it. In this sense, it is expected that the linkage process would be coordinated by the other available functional groups (-NH and –SH, respectively) as reported in other researches[71,72].

1.5. Characterization techniques

MNPs must be morphologically and structurally characterized. The morphological characterization techniques (Dynamic Light Scattering and Scanning Electron Microscopy), are used to elucidate the shape and size of the nanocrystals.

On the other hand, the structural characterization techniques (X-ray diffraction, fourier transform infrared spectroscopy and thermogravimetric analysis) are used to confirm and determine the MNPs phase (composition) as well as the surface content, in case any exists.

1.5.1. Dynamic Light Scattering (DLS)

DLS also called photon correlation spectroscopy (PCS) or quasi-elastic light scattering (QELS) analysis is a common technique performed as a routine in order to have a first contact with the sizes of the MNPs.

However, this size is larger than the obtained by other techniques because the hydrodynamic radius is taken into account [62,73]. A light from a laser diode is coupled to the sample through an optical beam splitter in a probe assembly. The interface between the sample and the probe is a sapphire window at the probe tip. The sapphire window 1) reflects the original laser back through the beam splitter to a photodetector, to act as a reference signal for detection, offering heterodyne detection; and 2) let the laser pass through it in order to be scattered by the particles which are in suspension but moving under Brownian motion. The laser is frequency-shifted according to the Doppler effect relative to the velocity of the particle. Light is scattered in all directions including 180 degrees backwards. This scattered, frequency-shifted light is transmitted through the sapphire window to the optical splitter in the probe to the photodetector. These signals

of various frequencies combine with the reflected signal of un-shifted frequency (Controlled Reference) to generate a wide spectrum of heterodyne difference frequencies.

The power spectrum of the interference signal is calculated with dedicated high speed FFT (Fast Fourier Transform) digital signal processors. The power spectrum is then inverted to give the particle size distribution[74],[75]. The general scheme of this technique is shown in **Figure 6.**
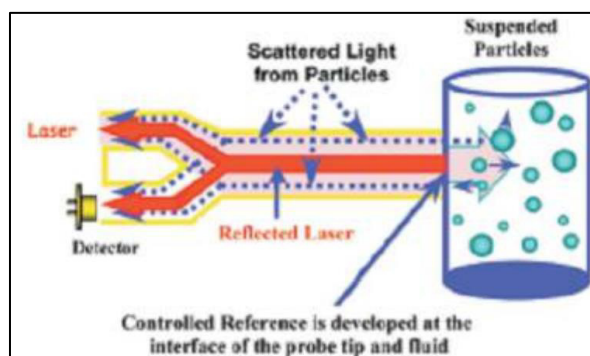
Figure 6. Scheme of DLS.

1.5.2. Electron Microscopy (EM)

EM is one of the most used techniques to scan across the surface of the specimen and gather information about it. This technique has replaced the light source with high energy electron beam which produces large numbers of signals. EM splits mainly in two sorts of methodologies, Scanning Electron Microscopy (SEM) and Transmission Electron Microscopy (TEM). These techniques chase different objectives which are directly related to the electron beam source. SEM provides information on morphology, surface characteristics, compositional information and atomic arrangement, while TEM allows observing the internal structure of solids and gives access to microstructural or ultrastructural details.

The general mechanism of the electron microscope is to make an accelerated beam of electrons influence, from energies ranging from hundreds of eV to dozens of KeV, on a sample. Such electron beam, before reaching the sample, passes through a series of apertures and magnetic lenses that allow focusing on the surface of the sample. **Figure 7** shows the specific SEM mechanism, where the electron gun emits a beam of accelerated electrons between 5 and 30 keV. The condensing lenses and the objective lens direct and focus the electron beam so that an electron beam as small as possible is incident on the sample.

Next, the scan coils sweep this fine beam of electrons over the sample, point by point and line by line. The secondary electrons that are ripped out of the sample are collected and amplified for each position of the probe by the secondary electron detector. Finally, it is represented on a screen where the brightest areas represent the zones of the sample from which more secondary electrons have been removed, and as the process is carried out, point by point, the result is an image.
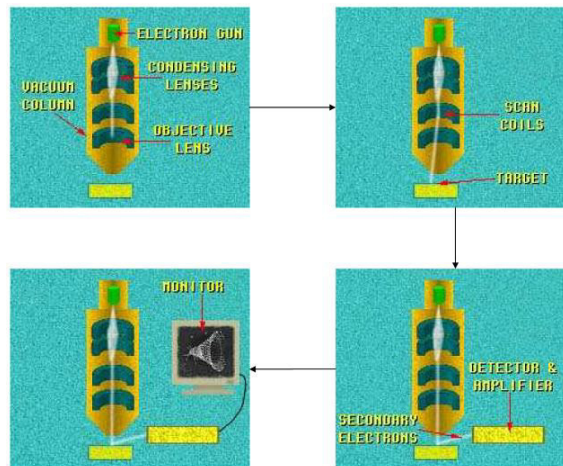
Figure 7. Scheme of SEM mechanism

On the other hand, TEM mechanism is almost the same, and it is represented on **Figure 8**, where again, a series of lenses focuses the high energy electron beam to form a small spot, or probe, incident upon a thin, electron-transparent sample. The aim of the lens system is to provide enough demagnification of the finite-sized electron source in order to form an atomic-scale probe at the sample. The objective lens provides the final, and largest, demagnification step. Scan coils are arranged to scan the probe over the sample in a raster.
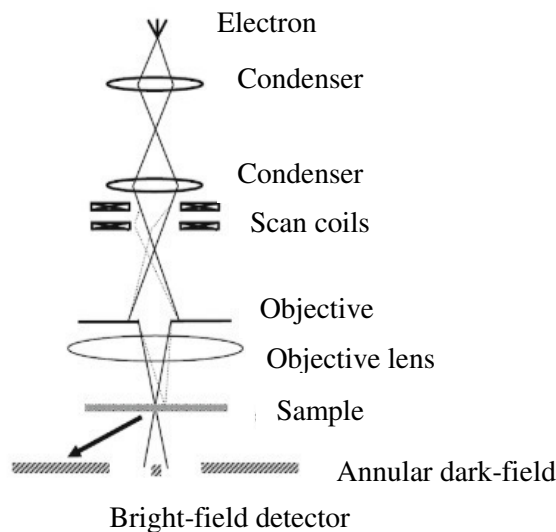
Figure 8. Scheme of TEM technique

Finally, and where the main difference lies on between SEM and TEM, is the detection of the scattered electrons, which are in this case the elastic and inelastic scattered electrons as shown in **Figure 9**. Once detected, they are plotted as a function of probe position to form a magnified image.[75]
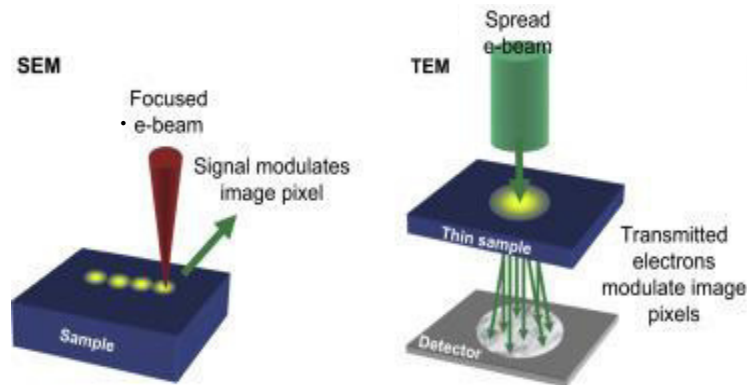
Figure 9. Main difference among SEM and TEM techniques.

TEM has a subdivision named Scanning Transmission Electron Microscopy (STEM) in which the electron beam is focused to a fine spot (with the typical spot size 0.05 – 0.2 nm) and then scanned over the sample in a raster illumination system constructed so that the sample is illuminated at each point with the beam parallel to the optical axis as shown in **Figure 10**. The rastering of the beam across the sample makes STEM suitable for analytical techniques such as Z-contrast annular dark-field imaging (ADF), and spectroscopic mapping by energy dispersive X-ray (EDX) spectroscopy[76].
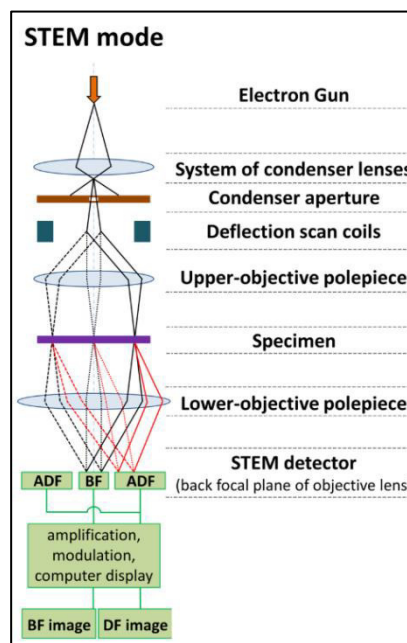
Figure 10. Scheme of STEM mode

1.5.3. X-Ray Diffraction (XRD)

All materials are built-up of individual atoms and nearly all materials have some degree of order or periodicity in the arrangement of those atoms called crystallinity.

A crystal is a solid composed of atoms arranged in a pattern, which is periodic in three-dimensional directions. With help of XRD crystalline phases can be identified, quantified, and their atomic structure can also be determined.

When a X-ray beam reaches a solid material, part of that beam is scattered in all directions because of the associated electrons with the atoms or ions that it finds on the path, but the rest of them can promote the diffraction phenomenon, which takes place if there is an ordered arrangement of the atoms and if the conditions that are given by the Bragg's Law are fulfilled. It relates the wavelength of the X-rays and the interatomic distance with the angle of the diffracted beam incidence. The general scheme of this technique is shown in **Figure 11.**
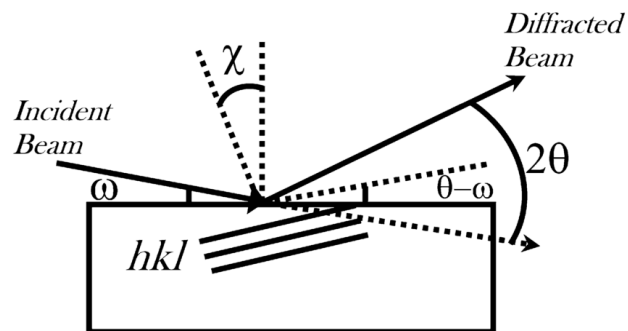
Figure 11. Scheme of XRD technique.

The diffractograms provide information about the crystallinity of the sample, the phases that are present and allow estimating the crystallite or grain size of the sample by applying the Scherrer equation[77] (equation 2).

$$\tau = \frac{K\lambda}{\beta \cos\theta} \qquad (2)$$

Where: $\boldsymbol{\tau}$: means size of the ordered (crystalline) domains, $\boldsymbol{K}$: dimensionless shape factor (typically about 0.9, but varies with the actual shape of the crystallite), λ: X-ray wavelength, $\boldsymbol{\beta}$: line broadening at half the maximum intensity (FWHM) and $\boldsymbol{\theta}$: Bragg angle.

1.5.4. Fourier Transform Infrared Spectroscopy (FTIR)

Vibrational spectroscopies, such as infrared spectroscopy, are known to be a versatile and rapid technique to capture a snapshot of the overall chemical structures in a measured sample. FTIR can provide a direct means to observe the interactions occurring at the surface during adsorption and to determine the structure of the adsorbed species.

FTIR spectroscopy mainly consists of a source, beam splitter, a fixed mirror and a moving mirror. The source emits light in the IR region (0.8-15.38 μm)[78] when electricity passes through it. The beam splitter divides the incident IR light into two. The mirrors are aligned so as to reflect the light waves in a direction that would allow recombination of the waves at the beam splitter.

The movable mirror is capable of moving along the axis, away from and towards the beam splitter. One part of the light passes through the beam splitter and is reflected by a stationary mirror back to the beam splitter. The other part of the light is reflected on to the moving mirror, which in turn reflects the light back to the beam splitter. The two reflected beams from the mirrors recombine at the beam splitter.

The difference in distance travelled by the two light beams, created due to the movement of the mirror, is called the optical path difference (OPD) or optical retardation. The recombined beam passes through the sample and is finally detected by the detector[79]. The general scheme of this technique is shown in **Figure 12.**
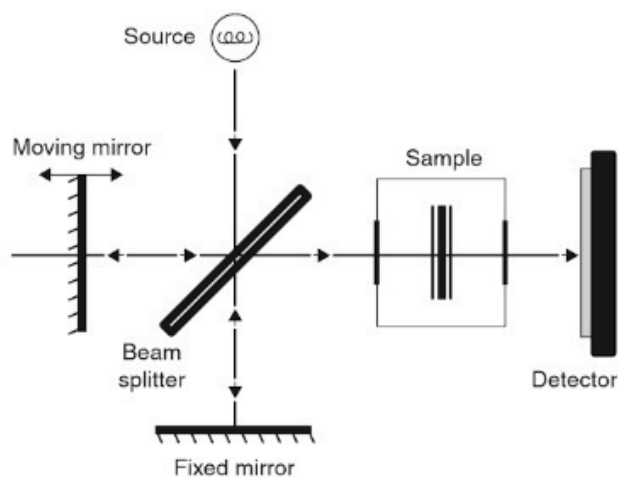
Figure 12. Scheme of FTIR technique.

1.5.5. Thermogravimetric Analysis (TGA)

Thermogravimetric analysis (TGA) is an analytical technique used to determine the composition of materials and to predict their thermal stability and its fraction of volatile components by monitoring the weight/mass change (loss or gain) that occurs as the

sample is heated at a constant rate with a Thermo Gravimetric Analyzer (TGA) or thermobalance[80], as shown in **Figure 13.**
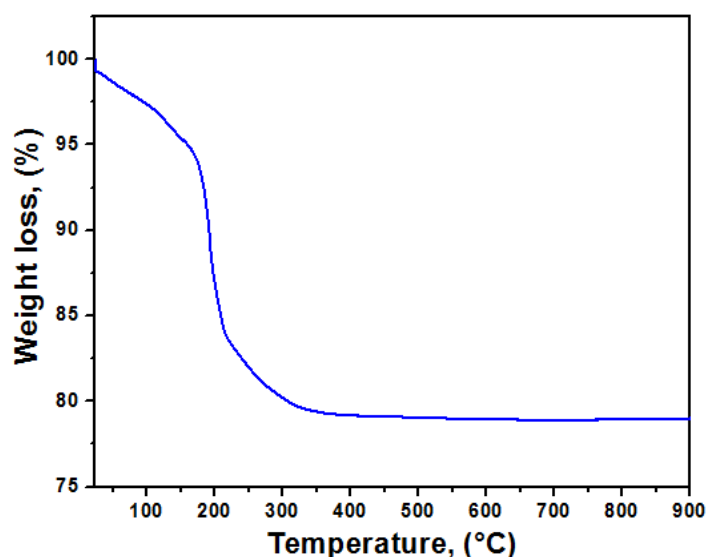
Figure 13. Thermogram of a sample showing the weight loss (%) as temperature is increased.

1.6. Experimental design

Experimental design or Design of experiments (DOE) is a very useful statistic tool that whenever possible, should be used during the research projects. It consists of an efficient procedure for planning some experiments, so that the obtained data can be representative and analyzed in order to get valid and objective information about the entire system[81]. It is possible to classify DOE according to different criteria. One of them is when we are interested in identifying the sources of variation in the behavior which is being studied, and another one, in identifying the cause-effect relationship[82].

If the objective is to study simultaneously the effect of two or more factors on some behavior, factorial design can be used. The resulting combinations of categorical predictors are known as treatments. Thus, the simplest factorial design contains at least four treatments since there can be two categorical predictors each with two levels.

The main advantage of this type of design is that the effects of the categorical predictors and their possible interactions can be simultaneously measured[83].

Interaction means that the effect of a categorical predictor over the response variable might depend on the particular level of another categorical predictor[84].

When DOE is applied the use of replication, randomization and blocking should be performed, in order to achieve a valid interpretation of the results, avoid confounding effects as well as experimental errors[83].

Our observations/experiments must be sufficiently replicated so that we can obtain consistent results. In addition to this requirement, our replications have to be statistically independent that one data point cannot predict another. The factors that cannot be observed are known as confounding factors and the may influence the behavior of interest, thus randomization is applied in order to ensure that every experimental unit has the same probability of being selected.

Blocking or matching consists of gathering the experimental units together into larger units according to a common characteristic; in this way statistically unwanted sources of variation can be removed by dividing inter-individual variation into variation between and within blocks.[85–87]

DOE specifically response surface methodology (RSM) has been used for different applications just like enzymatic esterification[88], selection of nutrient levels[89] and in the syntheses of nanoparticles[60] within others. This lies in its main advantage which consists in reducing the number of experiments that need to be carried out[90] and with such information, understanding of the interacting factors is obtained, as well as their optimization during the synthesis of nanomaterials[91-92].

1.7. Enzymatic inhibition of Horseradish Peroxidase (HRP)

The Population Division of the United Nations Department of Economic and Social Affairs (UN DESA) states that in 2011, the global population surpassed 7 billion and it is expected to reach 9 billion by 2045. This predictable population growth is also related to the eminent increment of industrial, mining and agricultural activities which may lead to more intense water pollution mainly by heavy metals.

Despite some heavy metals (iron, copper, manganese and zinc) in small quantities are essential for a healthy life, some others even at low concentrations can cause serious problems such as those affecting the central nervous system (Hg^{2+}, Pb^{2+}, As^{3+}); the kidneys or liver (Cu^{2+}, Cd^{2+}, Hg^{2+}, Pb^{2+}); or skin, bones, or teeth (Ni^{2+}, Cu^{2+}, Cd^{2+}, Cr^{2+})[93]. The long-term exposure to them may also have carcinogenic effects in humans and animals[94].

Since they are widespread pollutants which are released into the surface and ground water, it is important their monitoring as a critical issue in environmental protection, as well as disease prevention and treatment[95]. This is the reason why EPA of the United States of America fixed the maximum allowable concentration limits for mercury which are 2ppb or 2µg/L, equal to 10nM in water for human consumption[11].

Recent progress in nanotechnology has created a huge potential to build highly sensitive and low cost electrochemical (bio) sensors for heavy metals detection used in industry, medicine, biology, environmental and food chemistry. In particular MNPs are used for the immobilization of enzymes on their surfaces which also provides favorable microenvironment for electrochemical devices, where enzymes may exchange electrons directly with the transducer, improving the sensitivity and selectivity of electrochemical biosensors[96]. In this sense, the best mechanism to work with a biosensor whose target is a heavy metal, specifically mercury, is to take advantage of mercury toxicity, as it inhibits the enzymatic activity of HRP among others[97]. This enzyme is a peroxidase type which is present in the horseradish plant, and it is used in different organic and inorganic oxidation experiments.

The HRP enzyme uses hydrogen peroxide as an oxidizing agent to produce an oxidation-reduction reaction of a colored substrate which is measurable by spectrophotometric methods, determining the change of color of these chromogenic substrates. The responsible of this catalytic process is the heme group of the enzyme, which generates highly oxidizing intermediaries that are reduced to oxidize the substrate[98]. In order to follow up the HRP activity it is necessary to use a substrate of the peroxidase which acts as electron donor. When these components are oxidized by the enzyme in presence of peroxide, a characteristic change can be detected with spectrophotometry measuring the absorbance at a specific wavelength that varies according to the employed chromogenic substrate[99].

In this specific case, the colored component which is used to follow up the HRP activity is 2,2´-azino-bis(3-ethylbenzothiazoline-6-sulfonic acid) (ABTS) that in the presence of hydrogen peroxide, undergoes oxidation to the ABTS radical[100]. The formed radical can be quantified within the wavelength range from 400 to 800 nm, as its spectrum presents two absorption bands, one of them around 417 nm and another one at 735 nm.
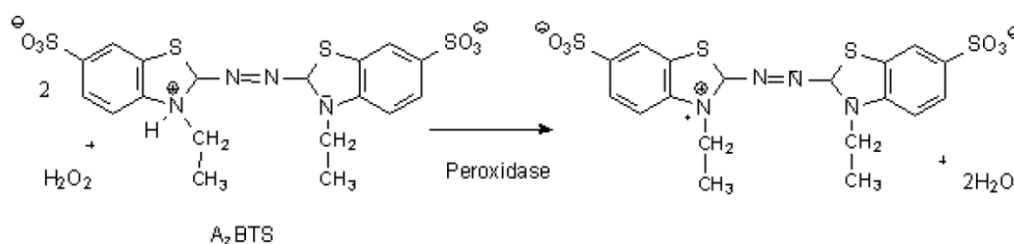
Figure 14. Production of ABTS from the enzymatic oxidation due to peroxidase.

Thus, this will be useful to indirectly find the mercury concentration by the inhibition of the HRP enzyme. This fact means that: 1) in the absence of mercury, the obtained absorbance values will be notorious, whilst 2) in the presence of mercury the absorbance values will decrease on account of the enzyme inhibition. So, with these variations of the absorbance values and color, it is possible to indirectly determine the mercury concentrations in the samples.

1.8. Medical application of MNPs

The quickly growing area of nanotechnology has led to important advances in material sciences, and non-invasive diagnostic methods have led to the development of a new class of drug delivery and therapeutic modalities. Among these materials, MNPs have shown to be a great contender in several areas of biomedical and clinical research.

Some of the reasons refer to their low general toxicity and high biocompatibility due to the existence of metabolic pathways for iron oxide magnetic nanoparticles absorption, decomposition and excretion by cells in human body[101–103]. Since MNPs can be monitored using their magnetic fields with magnetic field detectors, they have been used in medicine and biomedicine for applications such as biomolecular separations[104], treatment of hyperthermia in cancer[105], as contrast agents in magnetic resonance imaging (MRI)[106,107] and targeted drug delivery (TDD)[108]. TDD systems are reported to improve the bioavailability of poorly water-soluble drugs and boost the therapeutic efficacy of cancer treatments through the use of sophisticated target-selective nanomedicines based on carriers and carrier conjugates with different biologically active molecules[109].

1.8.1. Cancer

According to the International Agency for Research on Cancer (IARC) from the World Health Organization (WHO), the global cancer burden is estimated to have risen to 18.1 million new cases and 9.6 million deaths in 2018. One in 5 men and one in 6 women worldwide develop cancer during their lifetime, and one in 8 men and one in 11 women die from the disease[110]. Due to this big concerning fact, researchers and clinicians worldwide are developing new materials and strategies to be used in cancer therapy[111]. This effort will be determinant to minimize the side effects of conventional chemotherapy, prevent and detect cancer during earlier stages.

1.8.2. Tribbles 2 (TRIB2)

Protein kinases and phosphorylation modulate all aspects of eukaryotic cell biology and, together with members of the ubiquitin system, have become highly significant for mechanistic drug targeting[112].

The three TRIB pseudokinases (TRIB1, TRIB2, and TRIB3) represent a prominent subbranch of eukaryotic pseudoenzymes. TRIB proteins derive their name from the single metazoan fly gene "Tribbles" (*Trbl*), which encodes a pseudokinase with developmental roles in this model genetic organism. These proteins are fundamental regulators of cell cycle, differentiation, metabolism, proliferation and cell stress. They also fold to position protein "substrates" and control the E3 ligase-dependent ubiquitination of the eukaryotic protein kinase; and integrate and modulate signals flowing into and through canonical mitogen-activated protein kinase (MAPK) and AKT modules[14].

Recent data confirmed that TRIB2 protein expression is also cell cycle-regulated in human cells, positioning it as a potential modulator of CDC25 phosphatases, which it degrades through a ubiquitin- and proteasome-dependent mechanism[113]. However, the TRIB gene family in humans has been implicated in many different cancers, but especially in melanoma[114], lung[115], liver[116], and acute leukemias[117]

The main mechanism of these diseases is still in process of being dissected. Nonetheless, a major mechanistic function of TRIBs in cancer cells appears to be the inappropriate association of TRIB proteins with substrate degradation and stability networks, leading to a subsequent imbalance in timely regulation of crucial transcriptional networks. For example, TRIB2-mediated degradation of the transcription factors forkhead box O (FoxO) is known to have an oncogenic role in the development of melanoma. FoxO transcription factors are evolutionarily conserved proteins that coordinate gene expression programs known to control a variety of cellular processes such as cell cycle, apoptosis, DNA repair and protection from oxidative stress[114].

In this context, the present research aims to detect the presence of TRIB2 in an osteosarcoma cell line using MNPs functionalized with different coating agents and anti-TRIB2 antibody employing immunoprecipitation, sodium dodecyl sulfate polyacrylamide gel electrophoresis (SDS-PAGE) and Western Blot as supporting immunological techniques.

2. Experimental

2.1. Instrumentation

All the instrumentation and software used during this research is listed on the table below. The first column shows the name of the equipment or software; the second column shows the name of the company, and the third column indicates the purpose of each device.

Name	Company	Purpose
Statgraphics Centurion XVI statistical software	StatPoint Technologies Inc, Warrenton, Virginia, USA	Optimization of the synthesis through experimental design
Software Origin Pro 8 SR0	OriginLab Corporation, Northampton, MA, USA	Data treatment
Software DigitalMicrograph	Gatan Inc, USA	
Q700 Sonicator	QSonica Sonicators, Newtown, Connecticut, USA	MNPs synthesis Method A
Nanotrac Wave II Q	Microtrac, GmbH, Germany	Characterization stage
Nova NanoSEM 450	FEI, ThermoFisher, USA	
Talos F200X TEM	FEI, Thermo Fisher, USA	
D8 Advance-A25 Twin-twin	Bruker, USA	
IR Affinity-1S WL	Shimadzu, Japan	
FTIR Tensor 27	Bruker, USA	
TGA Q50 V20.13	TA Instruments, USA	
UV-Vis spectrophotometer model V-650	PG Instruments, UK	Enzymatic Inhibition studies
Nutating mixer	Labnet International, New Jersey	Total protein extraction
Centrifuge VWR CT15RE	Hitachi Coki, Japan	
Micro plate reader GloMax, Multi detection system.	Promega, Spain.	Total protein quantification
Bio-Rad power source	Bio-Rad, USA.	SDS-page Running process
Thermo Shaker TS-100	BioSan, USA	SDS-page Sample preparation
Software Chemidoc, Lab 4.0	Bio-Rad, USA	Protein detection
Molecular Imager, Chemidoc	Bio-Rad, USA	Protein detection

Table 2. List of software and pieces of equipment used during this research.

2.2. Materials

During the present research several materials were used in each of the different stages. Such materials are presented in the following table, where their name, purity (when applicable), enterprise and purpose are mentioned.

Name	Purity/Concentration	Company	Purpose
Ferrous chloride tetrahydrate $(FeCl_2 \cdot 4H_2O)$	$\geq 99\ \%$	Merck, Germany	MNPs synthesis Method A
Ferric chloride hexahydrate $(FeCl_3 \cdot 6H_2O)$	98-102 %	Panreac Quimica, Spain	
Ammonia solution (NH_3)	30 % (w/w)	Panreac Quimica, Spain	
Dopamine hydrochloride $(C_8H_{11}NO_2)$	-	Sigma-Aldrich, Germany	Functionalization of MNPs

3-Mercaptopropionic acid $(C_3H_6O_2S)$	$\geq 99\ \%$	Sigma-Aldrich, Germany	synthesized by Method A
Isonipecotic acid $(C_6H_{11}NO_2)$	$97\ \%$	Sigma-Aldrich, Germany	
Citric acid (anhydrous) $(C_6H_8O_7)$	$\geq 99.5\ \%$	Fluka Analytical, USA	
Horseradish Peroxidase (HRP)	-	Sigma-Aldrich, USA	Biosensor
Mercury(II) chloride $(HgCl_2)$	$\geq 99.5\ \%$	Sigma-Aldrich, USA.	
2,2´-Azino-bis(3-ethylbenzothiazoline-6-sulfonic acid) diammonium salt $(C_{18}H_{18}N_4O_6S_4)$ (ABTS)	$\geq 98\ \%$	Sigma-Aldrich, USA	Enzymatic inhibition studies
Hydrogen peroxide	$30\ \%$	Panreac Quimica, Spain	
Ultrapure water	-	Millipore, USA	Solvent
Ethanol	$96\ \%$	Alcoholes del sur, Spain	Solvent
Acetone	-	Alcoholes del sur, Spain	Solvent
Ferric chloride hexahydrate $(FeCl_3 \cdot 6H_2O)$		Panreac Quimica, Spain	MNPs synthesis Method B
Ammonia solution (NH_3)	$25\ \%$ w/w	Panreac Quimica, Spain	
Sodium sulfite (Na_2SO_3)	$98\ \%$	Fisher Chemical, UK	
Hydrochloric acid (HCl)	$37\ \%$ w/w	Analar	
Sodium citrate tribasic dehydrate $(C_6H_9Na_3O_9)$	$99\ \%$	Sigma-Aldrich, Spain	Functionalization of MNPs synthesized by Method A and B
Chitosan $(C_6H_{11}NO_4)_n$	$\geq 75\ \%$ (deacetylated)	Sigma-Aldrich, Portugal	
N-Ethyl-N′-(3-dimethylaminopropyl)carbodiimide hydrochloride (EDAC)	$> 98\ \%$	Sigma-Aldrich, Japan	
Tris	-	Fisher Scientific, China	CST Buffer used in protein extraction
Sodium chloride (NaCl)	$\geq 99.5\ \%$	Merck, Germany	
Triton X-100	-	Amresco, USA	Total protein extraction
Sodium fluoride (NaF)	-	VWR International, Belgium EC	
Ethylenediaminetetraacetic acid (EDTA) $(C_{10}H_{16}N_2O_8)$	$99\text{-}101\ \%$	Sigma-Aldrich, USA	
Ethylene glycol-bis-(β-aminoethyl ether)-N',N',N',N'-tetraacetic acid (EGTA)	$99\ \%$	AppliChem, Germany	
Sodium Pyrophosphate	-	Santa Cruz, USA	
β-Glycerolphosphate (β-G-P)	$\geq 97\ \%$	Santa Cruz, USA	
Sodium orthovanadate (Na_3VO_4)	$99.98\ \%$	Sigma-Aldrich, USA	
Calyculin A	$\geq 98\ \%$	Santa Cruz, Dallas	
Protease Inhibitors Cocktail (PIC)	-	Sigma-Aldrich, USA	
Laemmli 6x	-	Sigma-Aldrich, USA	Total protein quantification
Glycerol	$\geq 99\ \%$	Sigma-Aldrich, USA	
Bromophenol blue	-	Santa Cruz, USA	

Sodium dodecylsulfate (SDS)	95 %	Applichem, Germany	
β-Mercaptoethanol	≥ 98 %	Sigma-Aldrich, Japan	
Tris	-	Sigma-Aldrich, USA	SDS-page Running and stacking gel preparation
Acrylamide	40 %	Fisher Bioreagents, USA	
Sodium dodecylsulfate (SDS)	95 %	Applichem, Germany	
Ammonium Persulfate (APS)	≥ 98 %	Sigma-Aldrich, Japan	
Tetramethylethylenediamine (TEMED)	≥ 99 %	Santa Cruz, USA	
Running Buffer	-	Sigma-Aldrich, USA	SDS-page Running process
Glycine	≥ 99 %	Sigma-Aldrich, Belgium	
Sodium dodecylsulfate (SDS)	95 %	Applichem, Germany	
Blue protein Marker MB 17601	-	NzyTech, Portugal	
Bradford reagent	-	NzyTech, Portugal	Total protein quantification
Coomassie Brilliant Blue	< 5 %	BIO RAD, USA	Antibody disclosure
Nitrocellulose membrane	-	Amersham, UK	Protein transfer
Methanol	20 %	VWR, France	Transfer Buffer used in protein transfer
Glycine	≥ 99 %	Sigma-Aldrich, Belgium	
Milk	-	Nestlé, Portugal	Blocking step
Green Fluorescent Protein (GFP) antibody (sc-8334)	-	Santa Cruz (8334), USA	Antibody incubation
Actin (sc-1616)	-	Santa Cruz, USA	
Glyceraldehyde 3-phosphate dehydrogenase (GAPDH) (sc-25778)	-	Santa Cruz, USA	
Anti TRIB2 antibody	-	Homemade, UAlg Portugal	Immunoprecipitation
Secondary anti rabbit antibody (NA934V)	-	Amersham, UK	Protein detection
Luminol	> 97 %	Sigma-Aldrich, USA	
p-Coumaric acid	≥ 98 %	Sigma-Aldrich, UK	
Hydrogen peroxide (H_2O_2)	30.5 %	VWR, France	
Dimethyl sulfoxide (DMSO)	≥ 99.9 %	Fisher Chemical, Portugal	

Table 3. Reagents used during this project.

2.3. Synthesis procedure

Bare Magnetic Nanoparticles

Method (A) Co-precipitation method assisted by high power ultrasound.

MNPs were synthesized using a co-precipitation method[35] enhanced by a high frequency sonochemical probe (Q700 Sonicator) equipped with a 13-mm titanium tip, that provides a maximum power of 600 W. Briefly, a stoichiometric mixture of 0.005 moles (0.99 g) of $FeCl_2 \cdot 4H_2O$ and 0.01 moles (2.70 g) of $FeCl_3 \cdot 6H_2O$ were dissolved in 50 ml of distilled water and kept under nitrogen atmosphere for 2 minutes. The mixture was directly irradiated for 2 more minutes with the sonicator probe at a frequency of 20 kHz, operated at 50% of its total amplitude under nitrogen atmosphere in order to mix the salts solution. Right after this time, 4ml of NH_3 solution were poured dropwise into the mixture producing an instant change in color. The ultrasound irradiation continued for 3 more minutes after the addition of the basic solution. The total time of the entire reaction was 5 minutes.

The black precipitate was washed with distilled water using magnetic precipitation and decantation until a neutral pH was obtained. The black precipitate was further dried in an oven at 60°C overnight.

- Optimization of method (A) using DOE.

Response surface methodology (RSM), specifically factorial design at 3 levels and 2 factors (3^2) **(See Table 4)** was used to optimize the method and minimize the response (obtain smaller particle sizes).

Since pH values and temperature can affect the system by increasing the particle size[118,119], they were kept at 11.05 and 30-38°C, respectively.

	Low Level (-1)	Centre point (0)	High level (+1)
Amplitude (%)	20	40	60
Time (min)	1	3	5

Table 4. Experimental field definition

The quantities of the reagents were kept the same as previously described. The iron salt mixture was kept under a moderate nitrogen atmosphere for 1 minute, after this time it was directly irradiated with the sonicator probe at a frequency of 20 kHz, operated at 20, 40 and 60% of its total amplitude.

Right after the ignition of the probe, 4ml of NH_3 solution were poured into the mixture within 10 seconds producing an instant change in color. The total time of the entire reaction varied as shown in **Table 4** and the final temperature of each experience was kept within 30-38°C using an ice bath from the beginning, with the initial mixture of the salt precursors. The black precipitate was cleaned as described above.

Method (B) Co-precipitation from partially reduced ferric chloride aqueous solutions.

MNPs were synthesized using a precipitation method from partially reduced ferric chloride aqueous solutions[120]. Briefly, 30 mL of a 2M $FeCl_3$ stock solution, prepared by dissolving 16.22g of iron salt in 2M HCl, were diluted with an equal volume of deionized water. Afterwards, 20 mL of a 1M Na_2SO_3 were added under stirring. Just after the mixing of Fe^{3+} and SO_3^{2-}, the color of the solution altered from light yellow to red, indicating the formation of a complex ion. Meanwhile, an ammonia solution was prepared by the dilution of 50.8 mL of concentrated ammonia to a final volume of 800 mL. The former solution was quickly poured into the diluted ammonia solution, under vigorous stirring, as soon as its color changed back from red to yellow again, as the complex decomposed to Fe^{2+} and SO_4^{2-}. A black precipitate formed immediately, but stirring was continued for 30 min. A permanent magnet was applied to the beaker containing the suspension, and a black powder could be seen to quickly settle on the bottom. The supernatant was discarded and fresh water was added to the beaker. After decantation, the precipitate was washed once with an acidic solution (pH 3-4), then with distilled water until neutral pH, once with ethanol, and finally left to air dry overnight[121].
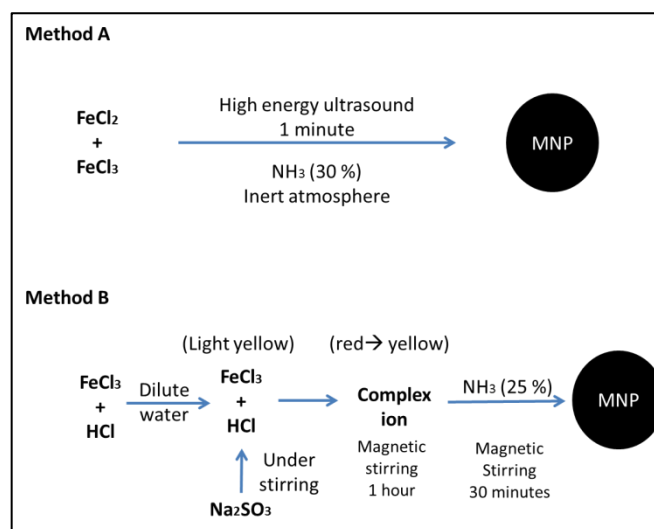
Figure 15. General syntheses schemes of method A and B performed in this research.

2.4. Functionalization of the MNPs

Different coating agents were used to functionalize the MNPs; these were polydopamine (PDA), chitosan (CS), citric acid (ACS), isonipecotic acid (ISNPA), 3-mercaptopropionic acid (MPA) and sodium citrate (SC). To make a layer of polymerized dopamine onto the MNPs surface, it was necessary to disperse 500 mg of the MNPs powder in 25 mL of a 10 mM (47 mg) solution of dopamine previously prepared in PBS (pH 8.5).

This was maintained for 3 hours under continuous agitation at 60 rpm. It is important to remove as much oxygen as possible from the PBS, putting it through an ultrasound bath before dissolving the dopamine to avoid its oxidation. After 3 hours, the cleaning process was performed with PBS (pH 8.5) using magnetic precipitation and decantation in order to remove the unreactive polydopamine. PDA@MNPs were dried for 5 days at 60°C and carefully grinded.

Chitosan was added onto the surface of the MNPs in a very similar manner to polydopamine. However, a 10 mM (42.3 mg) chitosan solution in 25 mL of water at pH 3 was prepared for 2 hours approximately and, upon complete dissolution, the pH further adjusted to 5.2. Right after the last adjustment, 500 mg of MNPs powder were immediately added into the chitosan solution, and maintained under magnetic stirring overnight. The cleaning process was carried out with distilled water until a neutral pH; then, further dried at 60°C for 5 days and equally grinded as the PDA@MNPs.

The carboxylate groups were obtained from citric acid (ACS), 3-mercaptopropionic acid (MPA), isonipecotic acid (ISNPA) and sodium citrate (SC) following a previous described methodology[122]. MNPs (400 mg) were re-suspended in 55 ml of different acid solutions (0.02g/mL, pH 5.2) of ACS, MPA, ISNPA and SC, respectively. This mixture was heated at 80°C under continuous reflux for 6 h. The final products were washed with distilled water (ISNPA, SC) and acetone (ACS, MPA) three times and collected by magnetic precipitation and decantation; further dried overnight at 60°C and carefully grinded. The general schemes of these functionalization processes are shown in **Figure 16.**
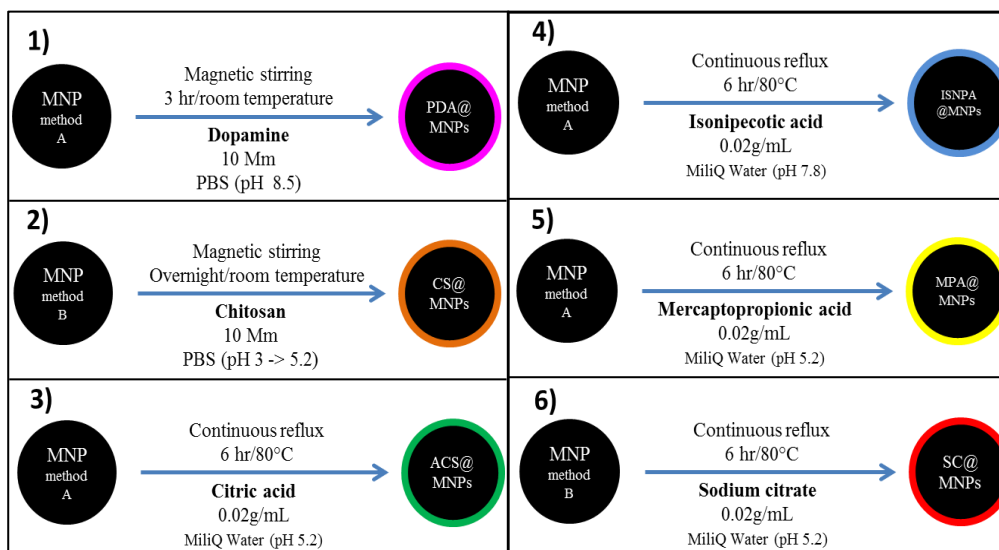
Figure 16. Functionalization schemes with the different coating agents.

2.5. Characterization of the MNPs

MNPs were synthesized using two different co-precipitation methodologies, method A and method B; and further functionalized with different coating agents. Bare MNPs synthesized by method B were characterized elsewhere[121]. CS and SC coated MNPs were characterized by FTIR. Bare MNPs synthesized by method A and further functionalized, were characterized by the following techniques:

- DLS to have a first contact regarding the size of the newly synthesized MNPs and make a proper decision on what MNPs to choose in order to continue working with. 5 mg of MNPs powder were re-suspended in 5 mL of distilled water. On one hand, 1 mL of these mixtures was directly analyzed with Microtrac Nanotrac Wave particle analyzer II Q.

- SEM to get a preliminary idea about topology and size of the MNPs and qualitative composition of the samples. This analysis was performed by a Scanning electronic microscope FEI, Nova NanoSEM 450.

  The MNPs powder was placed onto the surface of the aluminum samplers and introduced into the microscope.

- TEM to get a more accurate particle size of MNPs and determine their internal structure. The analysis was carried out with a Transmission electron microscope Talos F200X TEM (Thermo Fisher Scientific). MNPs were directly deposited from a solution onto Cu-amorphous C grids. No other preparation was needed.

- XRD to determine the composition of the phases and estimate the crystallite size. The XRD patterns were registered with Bruker-D8 Advance-A25 Twin-Twin equipment using Bragg-Brentano geometry with Lynxeye detector.

- FTIR to analyze the chemical nature of the obtained MNPs. The IR spectrums were registered in solid phase with KBr pellets, in a Shimadzu, IRAffinity-1S WL or a Bruker Tensor 27, from 4000 to 400 cm^{-1}.

- TGA to determine the fraction of volatile components of MNPs. The analysis was carried out using a TGA Q50 V20.13 with fixed parameters such as Nitrogen gas (40 mL/min), air (60 mL/min). The temperature range was stablished to be from 25 to 900°C with increments of 10°C/min and diminutions of 30°C/min at the end.

2.6. HRP. Immobilization of the enzyme onto the surface of the MNPs

Synthesized and further functionalized MNPs by method A were used to attach onto their surfaces the HRP enzyme in order to carry out enzymatic inhibition studies. 50 mg of PDA@MNPs were dispersed in 2.5 ml in a HRP solution (0.5mg/ml) prepared in PBS (pH 7.4) under gently stirring at room temperature for 3 hours.

After this time, MNPs were cleaned using magnetic precipitation and decantation with PBS (pH 7.4) in order to remove the excess of unreactive enzyme.

However, in this occasion MNPs were not dried, but re-dispersed in 1ml of PBS (pH 7.4). This dispersion was kept at 4°C and used within 2 weeks to avoid loss of activity.

2.7. Immobilization of the antibody onto the surface of MNPs.

Synthesized and further functionalized MNPs by methods A and B were used to attach onto their surfaces the antibodies in order to carry out immunoprecipitation studies. Five mg of MNPs (bare and coated MNPs) were used in each experience to test whether the antibody linked onto the surface or not. MNPs were dispersed in 500 ml of PBS (pH 5.6) and sonicated for 10 minutes. Five mg of *N*-Ethyl-*N′*-(3-dimethylaminopropyl) carbodiimide hydrochloride (EDAC) were added into the previous solution (except for the MNPs functionalized with PDA, in which case EDAC was not necessary). Finally, 50 µl of the antibody solution were poured into the prepared solution and kept under magnetic stirring at room temperature overnight. The same procedure was follow for a different experience but this time the last prepared solution was kept at 4°C under mechanical movement with a nutating mixer.

After this time, MNPs were cleaned using magnetic precipitation and decantation with PBS (pH 5.6) in order to remove the excess of unreacted antibody. However, in this occasion MNPs were not dried, but re-dispersed in 1ml of PBS (pH 5.6). This dispersion was kept at 4°C and further tested to prove the presence of the antibody onto the surface of MNPs, as it will be described on subsection 2.9.3.

2.8. Enzymatic inhibition study

These analyses were carried out using synthesized MNPs from method A coated with polydopamine. The measurements were done with a spectrophotometer model V-650 in the absorbance mode from 800 to 400 nm. For time issues it was only possible to assess PDA@MNPs. However, we plan to include the other coating results within an article we want to publish.

In first place, interferences for PBS, hydrogen peroxide and MNPs were investigated in order to avoid overlapping with the ABTS spectrum.

ABTS solution was daily prepared in PBS (pH 6) previously subjected to nitrogen stream for 10-15 minutes to remove the oxygen and avoid its oxidation.

For this purpose, different concentrations of the different components (**see Table 5**) were prepared in a total volume of 1.5 ml and further vortexed for 10 minutes. The absorbance was immediately measured in the specific range.

Component	Concentration
ABTS	0.3 mg/mL
MNPs@PDA/HRP	0.25 mg/mL
H_2O_2	0.3 % v/v

Table 5. Concentration of the different components used to measure their interferences

The second part of the enzymatic study aimed to create a calibration curve by adding mercury in successive concentrations (0.06, 0.05, 0.04 and 0.03 ppm) with the other components as shown in **Table 6**.

	Blank	0.03	0.04	0.05	0.06
$HgCl_2$	-	2.9 µL	3.8 µL	4.83 µL	5.80 µL
PBS	1027.5 µL	1024.6 µL	1023.7 µL	1022.7 µL	1021.7 µL
MNPs@PDA/HRP	7.5 µL				
ABTS	450 µL				
H_2O_2	15 µL				
Total Volume	1500 µL				

Table 6. Different solutions and their specific quantities used to perform the calibration curve

To complete this part of the study ABTS, H_2O_2 and PDA/HRP@MNPs were mixed in the same concentration as described in **Table 6** in a total volume of 1.5 mL.

The mixture was first sonicated for 2 minutes with an ultrasonic bath and further mixed with the desired mercury volume and vortexed for 8 minutes. Right after this time MNPs were magnetically precipitated and the supernatant was analyzed, using a cell with Milli-Q water as a reference.

2.9. Immunoprecipitation.

Immunoprecipitation (IP) is one of the most useful immunological techniques in which we can determine the presence and quantity of an antigen, the relative molecular weight of a polypeptide chain, its synthesis and degradation, the interaction with proteins, nucleic acids or other ligands. During this research project, the immunoprecipitation assays using different coated MNPs, were performed on an osteosarcoma cell line (U2OS) that has been manipulated to overexpress exogenous TRIB2 protein coupled to a Green Fluorescent Protein (GFP) on the N-terminus, as well as a parental cell line which did not contain the TRIB2 protein. The formed immune complexes were then denatured and resolved using SDS-PAGE and further analyzed with tools that include western blot[123].

2.9.1. Total protein extraction

To obtain the total cell protein extract we used two confluent 10cm plates of each cell line (U2OS parental cell line and U2OS-TRIB2-GFP). We collected the cell pellet, washed with PBS 1X and centrifuged at 1100 rotations per minute (rpm) for 4 minutes. We discarded the supernatant and the following procedures were always performed on ice to preserve the integrity of the extracted proteins.

Protein extraction was made using Cell Signalling Buffer buffer-CST (1M Tris pH 7,5M NaCl), 5% Triton X-100, 1M NaF, 0.5M EDTA, 0.5M EGTA, 200mM Sodium Pyrophosphate, 1M β-G-P, 100mM OVO4, 0.1 mg/μL Calyculin A and 0.1 mg/μL Protease inhibitor cocktail). 200 uL of CST was added to the cell pellet and the samples were homogenized by pipetting up-and-down and with vortex. Next, the samples were incubated for 20 minutes on a nutating mixer at 4 ℃. Afterwards, they were centrifuged at 15000 rpm for 20 minutes at 4 ℃. Lastly, the supernatant was transferred to a new Eppendorf tube.

2.9.2. Total protein quantification

The total amount of protein present in our samples was accessed using the Bradford method which is a very sensitive, simple and fast technique based on a colorimetric shift that is measured by absorbance.

By comparing the absorbance of our samples with the absorbance of a protein with a known concentration (Bovine Serum Albumine - BSA), we can determine the protein concentration of our samples using a linear standard protein curve. Serial dilutions on **Figure 17** were obtained from a BSA stock solution at 2000µg/µL.
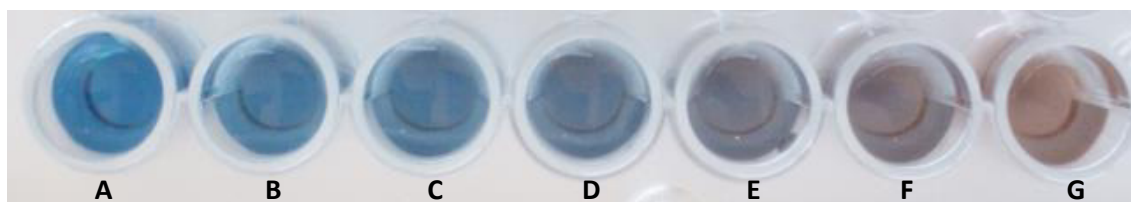
Figure 17. Standard curve BSA serial dilutions.
Letters **A** to **G** refer to seven different BSA concentrations namely A (2mg/mL), B (1.00 mg/mL), C (0.8 mg/mL), D (0.6 mg/mL), E (0.3 mg/mL), F (0.15 mg/mL) and G (0 mg/mL). These serial dilutions were used to create a stantard curve in order to calculate the concentration of the extracted protein. The measurements were performed in the absorbance mode.

We prepared a set of tubes containing a 1:10 dilution (5µL of sample in 45µl of H_2O) of our samples. Following, we loaded 5µL of each test sample (1:10 dilution) and standard curve sample into a 96 well plate (in duplicated) and added 250µL of Bradford to each well.

The absorbance was measured on a microplate reader using I-control software. Using the absorbance and the linear standard curve: $y = mx + b$, where y = absorbance at 595 nm and x = protein concentration; protein concentration was calculated for each of our test samples. Following, the protein concentration was normalized for all test samples using the extraction buffer to ensure that we load the same amount of protein in all samples for the following procedures. Additionally we added Laemmli 6x (0.2M TrisHCl), pH 6.8, 40% glycerol, 0.04% Blue Bromophenol, 0.3M SDS, 20% β-Mercaptoethanol. Laemmli is a protein-loading buffer that allows the visualization of the samples during the run (due to the presence of Blue Bromophenol) and simultaneously increases sample density for proper loading (due to glycerol) allowing the migration across the gel. The SDS present in the Laemmli charges the samples negatively, so the proteins can migrate to the positive pole, being separated according to their size. Lastly, we heated the samples at 95 ºC in a thermo shaker for 5 minutes.

This step allowed for denaturation of the proteins so that they can migrate on the gel when applying an electric stimulus. Samples were immediately loaded on a gel or stored at -20 ºC.

2.9.3. SDS-page

SDS-PAGE is a very high resolution method for protein separation and categorization, routinely used for the estimation of protein subunit molecular weights. The fundamental concept relies on the basis that charged particles migrate toward the electrode of opposite sign under the influence of an externally applied electric field. The movements of the particles are retarded by interactions with the surrounding gel matrix, which acts as a molecular sieve. The opposing interactions of the electrical force and molecular sieving result in differential migration rates for the constituent proteins of a sample[124,125].

In this regard, SDS-PAGE was performed to detect the presence of the antibody on the surface of MNPs and, as the assessment process by the Western Blot technique.

In general, all the gels were made in the same manner, as described in the next paragraph.

Proteins were separated according to their molecular weight, in a SDS-PAGE; 0.4M Tris pH 8.8, 10% acrylamide, 0.1% SDS, 0.1% Ammonium Persulfate (APS), 0.15% TEMED).

To obtain optimal protein resolution, a stacking gel was placed over the top of the running gel. This allowed proteins in a loaded well to be concentrated into one tight band during the first few minutes of electrophoresis, before entering the running portion of the gel. The stacking gel was prepared with 0.1M Tris pH 6.5, 3.8% acrylamide, 0.08% SDS, 0.1% APS, 0,1% TEMED. The stacking gel had large sized pores allowing proteins to migrate freely and get stacked at the interface between the stacking and the running gel. This allows proteins to start migration at the same time.

A 10% running gel was used since the size of the proteins of interest was within the separation range of this gel (70 to 20 kDa). The percentage of acrylamide present in the gel determines the speed of migration and the degree of separation between the proteins. Three microliters of the blue protein marker was loaded directed onto the gel. All other samples volume was adjusted with laemmli and CST buffer to a total of 25ul. The first sample was the positive antibody control in a mixture of 0.2µL of antibody, 4µL of Laemmli and 21µL CST. The second sample was the negative control of the Bare MNPs.

This mixture was prepared from 200µL of MNPs dispersion (5mg/mL); the supernatant of MNPs was removed using an external magnetic field, and MNPs were re-suspended in 21µL of CST buffer and 4µL of Laemmli were also added. Sample number three and four were prepared in the same manner than sample number two; the difference among them was the temperature used to attach the antibody onto the MNPs. Sample number three refers to functionalized MNPs whose antibodies were attached at room temperature, whilst antibodies of functionalized MNPs of sample four, were attached at 4°C. After this preparation, samples were heated to 95°C for 5 minutes and finally loaded into their respective wells in the gel. After loading the samples, the electrophoresis was performed in SDS-PAGE running buffer (0.02M Tris, 0.025M Glycine, and 0.003M SDS) using the BIO-RAD power source initially at 75V until proteins enter the running gel and then at 150V.

Once the electrophoresis was completed, the gels were removed from the plates and washed with tap water three times for five minutes each. We incubated the gels with 50mL of commasie brilliant blue for one hour. The gels were washed with tap water for three times, five minutes each, and the final washing step was left overnight. We imaged the gels using a molecular imager, Chemidoc.

2.9.4. Immunoprecipitation

For the immunoassays, 200µL of three different dispersed MNPs (SC/Ab@MNPs, PDA/Ab@MNPs and CS/Ab@MNPs) from a previous solution (5mg/mL; see subsection 2.7) were incubated with two different protein extracts at two different concentrations from different cell lines (U2OS parental and TRIB2-GFP). The immunoprecipitations were performed separately for each of the different coated MNPs and for the different protein concentrations, in two different Eppendorf Tubes of 2mL and, the general scheme is represented on **Figure 18.**
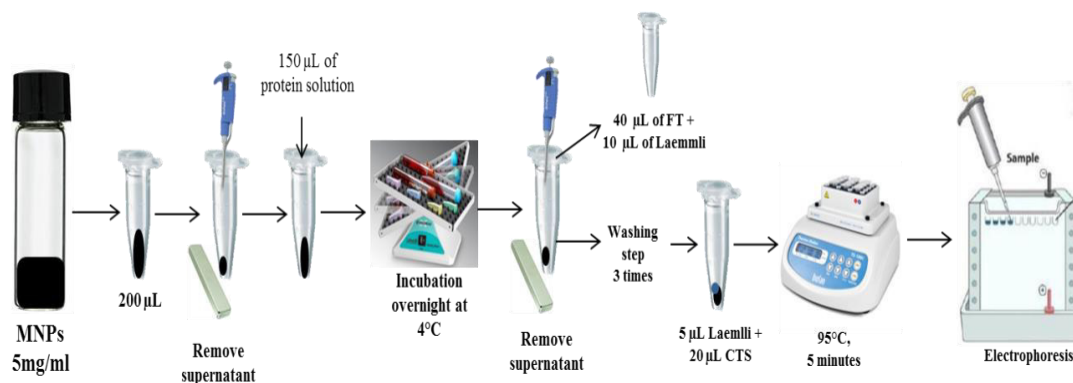

Figure 18. General scheme of the immunoprecipitation process.

The first immunoprecipitation was performed using the SC/Ab@MNPs with a protein solution 4μg/mL. The other two immunoassays were done using PDA/Ab@MNPs and CS/Ab@MNPs with a protein solution 2μg/mL each.

Initially, the supernatant of MNPs contained in the 200μL was carefully removed with a pipet using an external magnetic field. Right after, 150μL of the respective protein solution were added to the precipitated MNPs and incubated at 4 ºC using a nutating mixer overnight to allow an appropriate interaction. The following day, we pipetted 40μL of supernatant and mixed with 10μL of Laemmli 6x (0,2M TrisHCl pH 6.8, 40% glycerol, 0.04% Blue Bromophenol, 0.3M SDS, 20% β-Mercaptoethanol). This fraction corresponds to the flow through (FT). The rest was removed using an external magnetic field. Through this process the TRIB2-GFP molecules linked to the nanoparticles surface by means of the antibody–antigen interaction were collected at the Eppendorf's surface, close to the external magnet, and separated from the extract. MNPs were washed with 250μL of CST for three times.

Once the supernatant was removed, MNPs were mixed with 5μL of Laemmli 6x and 20μL of extraction buffer CST in order to have a proper mixture to perform the SDS-PAGE. Finally, 50μL of the initial extracted protein solution were placed in duplicate in two different Eppendorf tubes and mixed with 10μL of Laemmli. This fraction refers to the whole extract (WE). The previous prepared samples were heated at 95ºC for 5 minutes, loaded and ran on a 10% polyacrylamide gel.

2.9.5. Western blot

Western blot is often used to identify specific proteins from a complex mixture of proteins extracted from cells separated according to their molecular weight.

After the immunoprecipitation and electrophoresis were completed, the Western Blot was performed as follows.

2.9.5.1. Protein transfer

A wet-transfer was performed into a nitrocellulose membrane. The SDS-PAGE transfer buffer contained 20% methanol, 0.05M Tris and 0.05% Glycine. The transference was performed using a BIO-RAD power source at 75V for 90 minutes.

2.9.5.2. Blocking step

The blocking step prevents the binding of the antibodies to unspecific proteins existing in the membrane surface. We used a 5% non-fat milk solution made in TBS-Tween. The proteins present in this solution blocked the unoccupied sites on the membrane, thus reducing background at detection time and improving the signal-to-noise ratio of the

assay. This incubation was made at room temperature for one hour with agitation.

2.9.5.3. Antibody incubation

After blocking, the membrane was incubated overnight at 4 ℃ using a roller mixer with primary rabbit antibodies such as Green Fluorescent Protein (GFP) that binds to the target TRIB2-GFP protein; and other two primary antibodies, actin and Glyceraldehyde 3-phosphate dehydrogenase (GAPDH).

2.9.5.4. Protein detection

This step allows the detection of the relative abundance of the target protein -TRIB2. Once the primary antibody incubation was done, the membrane was washed with TBS tween three times, five minutes each to remove the excess of unreactive primary antibody. Then, the membrane was incubated with a secondary rabbit antibody for one hour which was previously prepared in 5% non-fat milk dissolved in TBS tween. Following, the membrane was washed again with TBS tween three times, five minutes each to remove the excess of unreactive secondary antibody. The membrane was further incubated for 5 minutes in enhanced chemiluminescence (ECL; 1.25mM Luminol) diluted in Dimethyl Sulfoxide (DMSO), 0.2mM p-coumaric acid diluted in DMSO, 0.1M Tris pH 8.5, 0.01% H_2O_2. The enzyme coupled to the secondary anti rabbit antibody is oxidized in the presence of peroxide, producing and excited state product that emits luminescence, which was detected using the software Image Lab 4.0 of Chemidoc.

3. Results and discussion

3.1. Synthesis

As stated in subsection 1.1, the common co-precipitation method has some drawbacks when synthesizing MNPs. This was the main reason why this research group decided to improve the procedure by assisting it with high power ultrasound (Method A), which is based on the decomposition of a solution containing the precursors and reducing or stabilizing agents with ultrasound irradiation. This methodology provides a unique medium in which reactions take place in a more efficient and effective way.

This was positively confirmed through the syntheses carried out during this research: the applied energy was minimized and better used, the synthesis time was drastically reduced to one single minute, the simplicity of the synthesis increased by using the high power ultrasound approach (see **Figure 19**) what leads us to save time, and the amount of reagents employed was enormously decreased being able to reduce costs and protect the environment.

Besides all these advantages, it was possible to obtain uniform particle size distributions of 10 ± 3 nm according to predefined factors which will be discussed in the next subsection. On the other hand, method "B", provided good particle sizes of 15 nm[121] very close to those obtained by method "A".

As conclusion, it can be said that traditional techniques are very good for producing large amounts of MNPs; however they are time-consuming, they need much more reagent volumes and the energy requirement is higher. That is the reason new methodologies such as methods A and B are being developed. Both of these techniques are good and useful when synthesizing MNPs with some differences among them, but at the end those differences try to fulfill the same objective. A clear example of this is that both methodologies aim to avoid the oxidation of iron, but method A does it through the use of nitrogen flow whilst in method B sulfite is used to provide a reductive environment, thus preventing oxidation. At the end, despite both of them have proved to be useful in synthesizing MNP, method A minimized the use of time, reagents, energy and thus their cost.

Figure 19. Simple comparison between a traditional co-precipitation method (left picture) and co-precipitation assisted by high power ultrasound (right picture)

3.2. Optimization of method A.

Based on the RSM, 3^2 factorial design for two independent factors, 18 experimental syntheses were performed. This design implied 9 experiments in duplicate, carried out in random order to eliminate any potential source of error. **Table 4** and **7** demonstrates the experimental field definition and experimental matrix, respectively.

The MNPs obtained from the 18 syntheses were characterized by DLS technique, which has been demonstrated to be a useful technique for this purpose (immediate and routine analysis)[60]. The size distributions showed Gaussian shape; however the weighted mean which refers to the hydrodynamic radio was used [size (nm)]; due to it was necessary to obtain a unique value as the response instead of a size distribution.

Experiment	Amplitude (%)	Time (min)
1	+1 (60)	+1 (5)
2	-1 (20)	-1 (1)
3	0 (40)	0 (3)
4	1 (60)	-1 (1)
5	-1 (20)	1 (5)
6	1 (60)	0 (3)
7	0 (40)	1 (5)
8	-1 (20)	0 (3)
9	0 (40)	-1 (1)

Table 7. Experimental matrix

The hydrodynamic radio represented as size duplicate mean [x (nm)] and its corresponding %RSD are shown in **Table 8.** In this regard, MNPs with different sizes from 33 to 60 nm were synthesized.

The highest mean values (60 and 58 nm) were obtained in Exp.3 (A: 40%, t: 3min.) and 1 (A: 60%, t: 5min) with also high values of RSD (7 and 9%, respectively). On the other hand, the smallest mean values were for Exp.9 (A: 40%, t: 1min) and 4 (A: 60%, t: 1min); however Exp.4 had a big RSD (9%) as in Exp. 1, where the same amplitude of 60% was used, what can lead to think that this amplitude is so strong that produces a wide variation in the nanoparticle sizes distribution, which is also confirmed with Exp. 6 (A: 60, t: 3min, RSD: 17%). This aspect could be further supported due the fact that experiments 2, 5, 7 and 9 with amplitudes of 20 and 40 % had good reproducibility of 4%.

Regarding Exp.9, which had the smallest value for particle size and the same amplitude than Exp. 3, which had the biggest value, it can result strange. Nevertheless, reaction time among these two experiments was different. Exp.3 was performed for 3 minutes whilst Exp.9 for only 1 single minute, what could be the influential factor between these 2. The difference in sizes despite of the same amplitude might be due to the reason that the more time the reaction last, the more the nanoparticles agglomerate.

Experiment	Replicate 1 (size, nm)	Replicate 2 (size, nm)	x ± SD (nm)	RSD (%)
1	61	54	58 ± 5	9
2	47	50	49 ± 2	4
3	63	57	60 ± 4	7
4	34	38	36 ± 3	9
5	40	38	39 ± 2	4
6	37	47	42 ± 7	17
7	37	39	38 ± 2	4
8	49	56	53 ± 5	9
9	34	32	33 ± 2	4

Table 8. Experimental design results

Thus, according to these results which were used to have a first contact regarding how these variables affected the particle size distribution; if small particle size is wanted by this novel approach (high power ultrasound), slow amplitude and short periods of time should be selected. The experimental design allows comparing effects with more than one factor, as well as the effects of each factor separately. When comparing effects with more than one factor, if results are statistically different, an interaction between the analyzed factors takes place[126,127]. Once the particle sizes were obtained (response

value), an influence study of the different factors over this response was performed. Such study is shown on **Table 9.**

Source	Sum of squares	Half square	F	p-value
A:amplitude	60.75	60.75	2.41	0.1486
B:time	96.3333	96.3333	3.83	0.0763
AA	110.25	110.25	4.38	0.0604
AB	480.5	480.5	19.09	0.0011
BB	961	961	38.17	0.0001
Total error	276.944	25.1768		
Total correlation	1988.5			

Table 9. ANOVA results, 95% confidence value

Those variables whose p-value is below 0.05 are considered statistically significant with 95% confidence value. It can be observed how two interactions, AB (amplitude and time) and BB (quadratic interaction of time) are considered statistically significant. On the other hand amplitude, time and quadratic interaction of amplitude have p-values above 0.05, which are considered to not affect the response value.

The fourth column shows the F-value, a quotient between the different half squares and the mean error of the analysis. Because this parameter consists of a quotient between variances, the most significant effects will be those whose ratio between variances is much greater than the unit, while F values close to one imply little difference between variances[126]. It is proved how the strongest effects according to this column, AB and BB, match with the reasoned ones from the column of the p statistical parameter.

The analysis of variance (ANOVA) was performed at a significance level of 95 %. The results of ANOVA are represented in **Figure 20**.

This figure shows the standardized effects of the principal factors and its interactions from the most to the less important factor. To evaluate which of them are statistically significant, a t-value of 2.0796 is critical (vertical line in **Figure 20**).
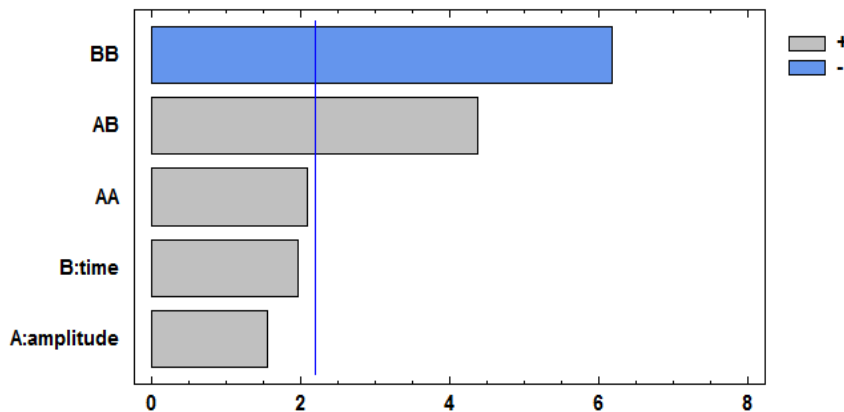

Figure 20. Standardized Pareto Diagram for particle size.

ANOVA results also verified once again that AB and BB were the factors that influence the most over the particle size. The quadratic relation of time showed a negative correlation in the response, which means that the longer the reaction time, the bigger the particle size whereas the interaction between amplitude and time showed a positive correlation, meaning that this interaction minimize the response value.

ANOVA also allows calculating the adjustment of the mathematical model generated from the experimental data. For this case, 86.07% of the system total variance was explained by the mathematical model generated from factors variance.

The present research was done for a unique response (R_1), which was to minimize the particle size. According to experimental data of this response, the regression equation was presented to predict the relationship of response value and the amount of defined factors. The fitted model on the particle size of samples can be presented as follows:

$$R_1 = 54.625 - 1.51875*A + 16.9167*B + 0.013125*AA + 0.19375*AB - 3.875*BB$$

Where R_1 is the particle size (nm) of the synthesized MNPs, *A* and *B* are the defined factors amplitude (%) and time (minutes), respectively; *AA* and *BB* are the quadratic interactions of amplitude and time, respectively; and *AB* is the interaction between amplitude and time. All these factors can take any value between the low and high levels according the experimental matrix (see **Tables 4** and **7**).

The optimum calculated values for amplitude and time from this equation were 50.50% and 1 min, respectively. Nevertheless, it must be remembered that there was still a 13.93 % of the system total variance that the mathematical model could not explain.

In this regard, the independent effects presented by amplitude and time were also studied. **Figure 21** shows the two different profiles where, the particle size is represented on the "Y" axis and each of the different tested values for amplitude and time on the "X" axis.
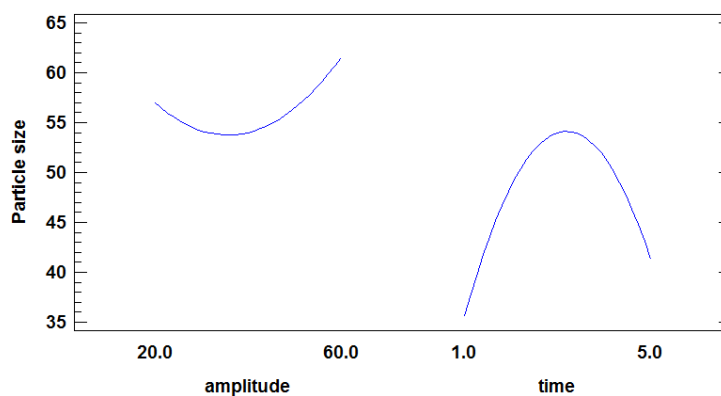

Figure 21. Main effects for particle size.

The right negative parable on **Figure 21** shows how one minute of reaction time produces smaller particle size than five minutes, which was predicted by the mathematical model and fitted well with the experimental data. The left positive parable refers to the different amplitude values used in the syntheses.

These results matched well to the experimental data previously discussed; higher amplitude values resulted in bigger particle sizes and lower values in smaller particle sizes. However, it can be observed that before the center of the parable there was a possibility to decrease a little bit more the particle size, what apparently does not match well with the amplitude value of 50.50 % from the mathematical model.

Since results from the previously described paragraph did not seem to match with the mathematical model, it was decided to study the interaction among these two main factors. **Figure 22** represents the estimated response profile obtained for minimum and maximum time values, over the range of amplitude values. This figure proves once again how 5 minutes reaction time had a continuous and increasing important effect over the particle size as amplitude was elevated. On the other hand, high amplitude values around 50% for one minute seemed to provide smaller particle sizes and as the amplitude was decreasing the particle size was increasing.

However, it is noteworthy to observe the intersection point, between amplitude values around 35 to 40, which lead us to think that the optimum amplitude value is around this range. In this sense, it was decided to perform extra syntheses with an amplitude value stablished at 50% according to the suggestion of the mathematical model; and further characterized in order to compare particle sizes obtained from syntheses with amplitude values of 40 and 50%. The discussion of these results is described in subsections 3.3.1 and 3.3.2.
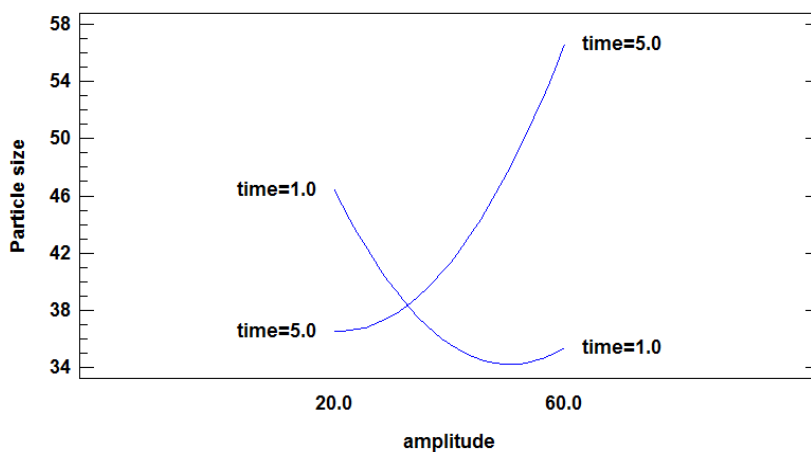

Figure 22. Interaction plot among time and amplitude, for particle size.

3.3. Characterization of the MNPs

3.3.1. DLS

Several syntheses with different conditions during the optimization of method A were performed in order to test whether these conditions influence the particle size of the synthesized MNPs. Such MNPs were measured in first place with DLS to have a first idea of their particle sizes, using this technique as fast and routine analysis[60]. From **Table 8**, experiment number 9 (amplitude: 40%, time: 1 minute) gave the smallest particle size (33±2nm) with a good relative standard error of 4 percent. Thus, during the first contact these conditions seemed to be the best ones; however DOE was suggesting amplitude: 50.50% and time: 1 minute. For that reason two more syntheses were performed with such conditions. Further characterization was also performed in order to compare hydrodynamic radios and be sure about the previous results among particles sizes obtained by different amplitudes within 1 minute. **Figure 23** shows their different particle size distributions by DLS.
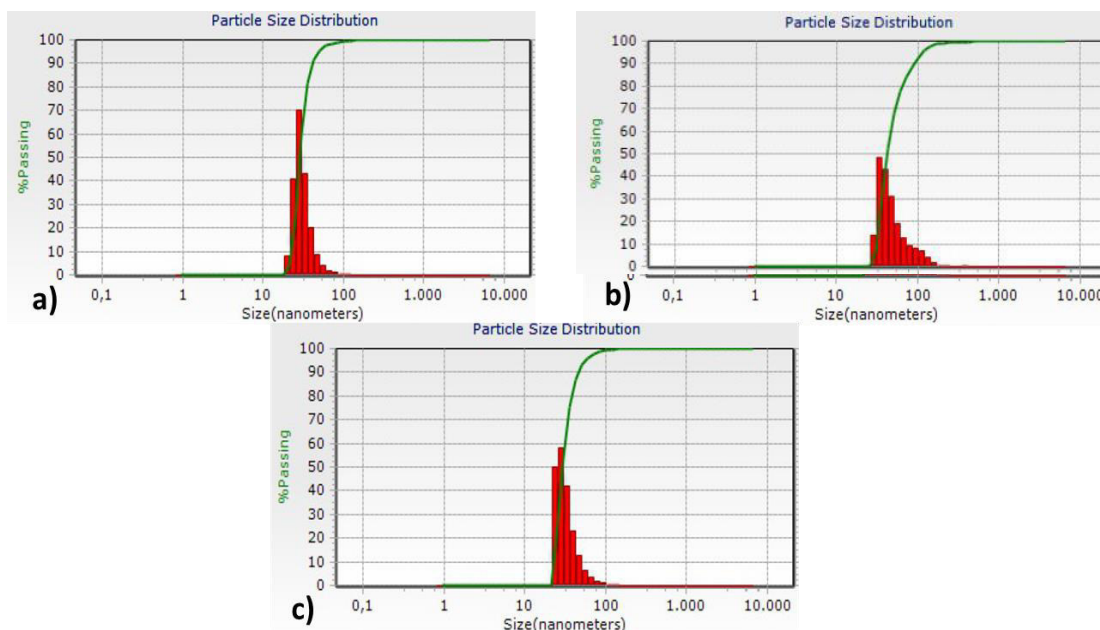

Figure 23. Different particle size distributions of MNPs with their respective mean size and standard deviation; synthesized each of them for 1 minute but with different amplitudes.
a) Amplitude: 40%; x: 33 ± 2 nm, **b)** Amplitude: 50%; x: 54 ± 13 nm, **c)** Amplitude: 60%; x: 36 ± 3 nm.

When comparing the results of the new synthesis with amplitude: 50% versus the others previously stablished, it came out that synthesis with amplitude of 40% (a) had a better Gaussian distribution than b) and c), and besides that, smaller mean particle size, as expected. The new synthesis (b) had the highest mean particle size and highest SD (54 ± 13 nm) when it was expected to be at least between them or below synthesis with amplitude value of 40% due to DOE suggested that the optimum amplitude value was 50%; however, it must be remembered that DLS it is just an approximate technique and that is why, electron microscopy should be used in most of the studies.

3.3.2. EM

Electron Microscopy is a powerful tool in the study of nanostructured materials; from there the importance to analyze by EM the bare MNPs synthesized by method A.

DOE explained the 86.07 % of the system total variance during the optimization of the synthesis. It suggested that the optimum amplitude value was 50%. Thus, its synthesis was properly carried out and firstly characterized by DLS. This result, from the last subsection did not match well compared with the others two (40 and 60%). In this sense, MNPs synthesized with different amplitudes values of 40, 50 and 60% were analyzed through SEM in order to assess which one of them gave the smaller particle size and if these values fitted well with the mathematical model.

3.3.2.1. SEM results

Figure 24 shows the images and histograms with their statistician charts (N: number of counted particles, x: average size of the population and SD: standard deviation) of the different syntheses previously described. The obtained statistics from the SEM images were performed by measuring as many MNPs as possible with Digital Micrograph software, in order to have more representative results. In most of the cases more than 100 counts were done.

From **Figure 24,** it can be observed SEM images (**a.1, b.1** and **c.1**) with very well defined and spherical MNPs obtained through co-precipitation method assisted by high power ultrasound. However the size distribution and mean particle size is different in all of them, being the best one the represented by histogram a.2 whose synthesis was performed with an amplitude value of 40%, producing uniform size distribution around 13 ± 3 nm. The other two histograms (b.2 and c.2) show wider distribution and bigger particle size around 14 and 15 ± 3 nm, respectively. In this sense, and clarifying the results of DOE and DLS (subsections 3.2 & 3.3.1, respectively) previously discussed

regarding the optimum amplitude value, it can be said that by a minimum difference of 1 nm, the amplitude value that produces smaller particle sizes is the amplitude 40%. In this regard, the mathematical model presented in this work (subsection 3.2) is considered to properly explain the 86.07 % of the system total variance. However, it was decided to keep the amplitude value = 40% for future syntheses due to a more uniform size distribution is achievable, less energy is consumed during the synthesis and smaller particle sizes are obtained.
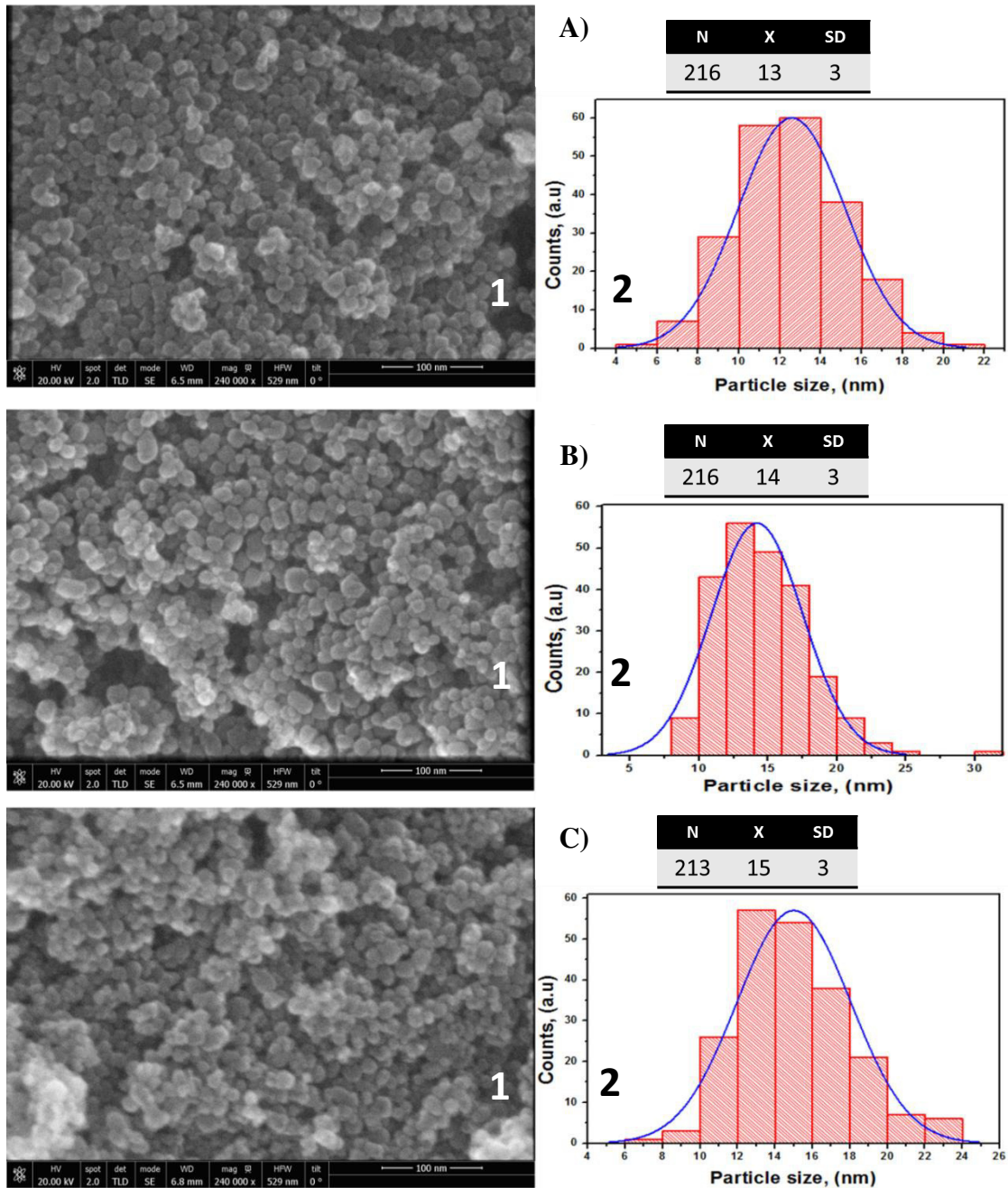

Figure 24. SEM images of MNPs synthesized at different values of amplitude and 1 min of time: **a.1) 40% b.1) 50%** and **c.1) 60%.** Corresponding histograms and statistician charts are showed for each of them in **a.2), b.2)** and **c.2)**, respectively. (N: counts, X: average size, SD: standard deviation)

MNPs synthesized under conditions of amplitude: 40% and time: 1 min, were functionalized with PDA, ACS, MPA and ISNPA as described in subsection 2.4. Once again and in order to make sure they have been functionalized, coated MNPs were analyzed by SEM to test if there was an increment in their sizes. Images, histograms and statistician charts are shown in **Figure 25**.

It must be remembered from **Figure 24**, **a.2**, that the mean particle size obtained for bare MNPs is 13 ± 3 nm. Histograms **a.2, b.2, c.2** and **d.2** from **Figure 25** show higher mean particle sizes of functionalized MNPs (16, 16, 15 & 14nm, respectively) and uniform size distribution. These increments on size are attributed to the correct coating process where the corresponding functional groups of each coating agent linked onto the surface of the bare MNPs, which also produces a good stability among them.

SEM images **a.1, b.2, c.2** and **d.2** from **Figure 25** still show well defined and spherical MNPs, a bit bigger though, due to their coating layer.

The SEM images of MNPs synthesized by method B are shown somewhere else [121]. Nevertheless, the produced MNPs had diameters of about 15 nm with regular shape. Moreover some agglomeration is also shown what can be explained due to the large reaction time of the synthesis. Nonetheless, the size of such MNPs is within the range of sizes obtained by method A (13 ± 3 nm).

In conclusion, it was possible to corroborate by SEM means, what amplitude gave the best particle sizes and size distributions (amplitude: 40%). It was also confirmed that the coating step or functionalization was performed properly due to an increment of the initial size of bare MNPs (from 13 to 16, 16, 15 and 14 ± nm). And finally, both synthesis methods are comparable. However method A possesses interesting and useful advantages, mainly related to saving time and cost significantly.
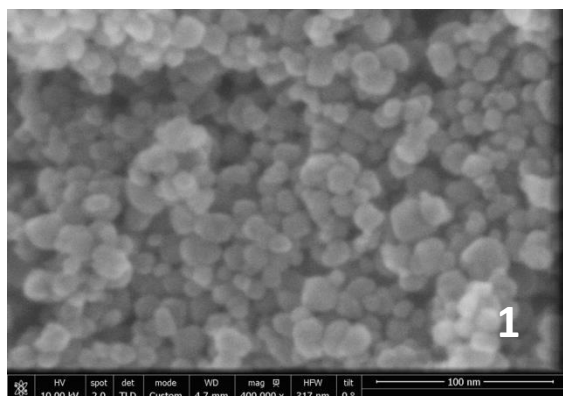
A) PDA@MNP

N	X	SD
136	16	3
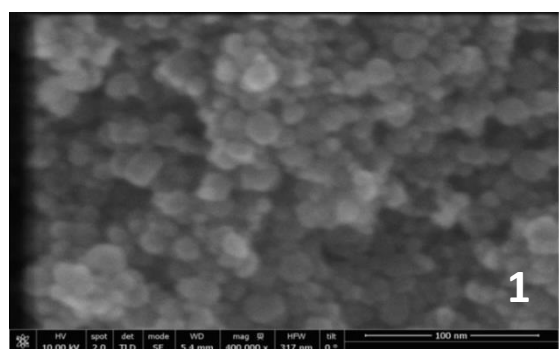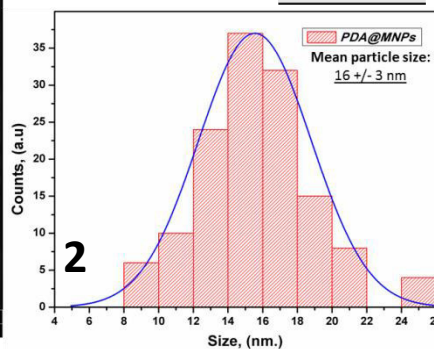
B) ACS@MNP

N	X	SD
102	16	3
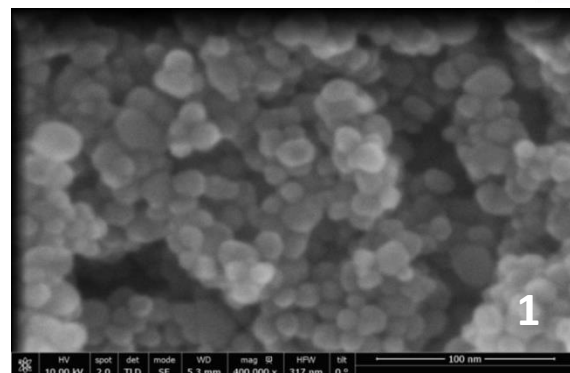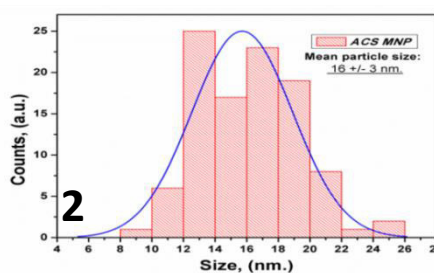
C) MPA@MNP

N	X	SD
133	15	3
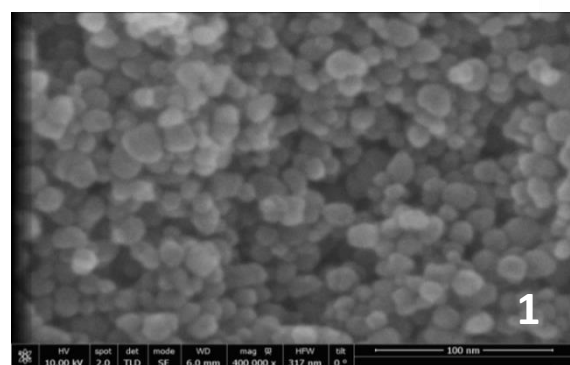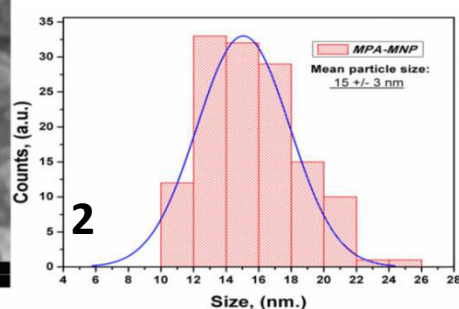
D) ISNPA@MNP

N	X	SD
159	14	3
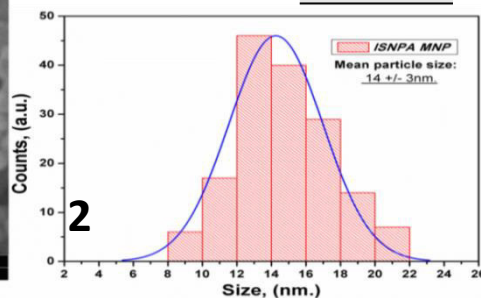
Figure 25. SEM images of different functionalized MNPs synthesized at amplitude 40% and 1 min of time. A.1)PDA@MNPs, **B.1)**ACS@MNPs, **C.1)**MPA@MNPs and **D.1)**ISNPA@MNPs. Corresponding histograms and statistician charts are showed for each of them in **A.2), B.2), C.2)** and **D.2),** respectively. (N: counts, X: average size, SD: standard deviation).

3.3.2.2. STEM and TEM results

Transmission electron microscope Talos F200X TEM equipment was employed for taking TEM micrographs at 200 kV using the scanning/transmission (STEM) mode with a high-angle annular dark-field (HAADF) detector and the high resolution mode (HREM). Scanning-transmission electron microscopy (STEM) characterization was performed with FEI Nova NANOSEM 450 (resolution = 1 nm). However, in this case, the micrographs were taken at 30 kV, with the sample previously deposited onto a copper-carbon grid, and at several modes: high-angle annular dark-field (HAADF), bright field (BF) and dark field (DF) modes. For these studies only bare MNPs and PDA@MNPs were analyzed by both methodologies due to time issues. **Table 10** contains the data extracted from STEM images in **Figure 26** as well as from TEM images in **Figures 28** and **30**.

Nanostructures	Average size (nm)	SD (nm)	Distribution range (nm)	Range with more %	Variance of sample
Bare MNPs (STEM)	10	2	4-13	6-13 (90%)	3.63
PDA@MNPs (STEM)	11	2	7-18	9-16 (94%)	4.69
Bare MNPs (TEM)	11	2	7-16	8-15 (94%)	4.23
PDA@MNPs (TEM)	11	2	6-20	8-16 (94%)	6.05

Table 10. Comparative table of particle sizes.

As it can be seen, in all cases, independently of the measuring technique employed, MNPs possess an average size of about 10 ± 2 nm, being more than 90% of the particles with a size between 6 and 13 nm. Besides, STEM technique does not provide information regarding the covering of MNPs with PDA, since the size obtained for both EM techniques is similar to the size obtained for non-covered MNPs. The small differences in the distribution range can be attributed to variability during measurements. It is noteworthy to mention that the size of MNPs and PDA@MNP nanostructures is very difficult to be measured in some cases due to agglomeration of the nanoparticles for their magnetic character.

Regarding morphology, from SEM and STEM micrographs on **Figures 24, 25 and 26**, MNPs are predominantly spherical.
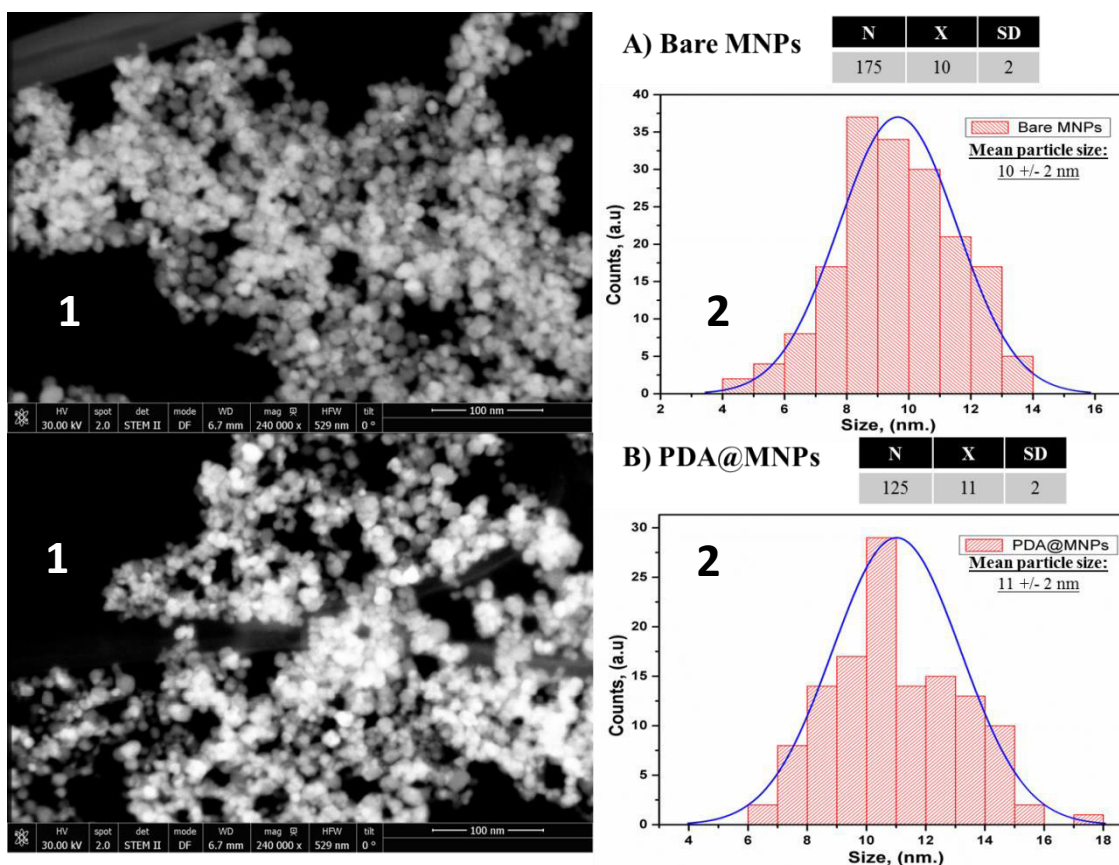
Figure 26. STEM images of bare MNPs and PDA@MNPs using DF mode
A.1) Bare MNPs and **B.1)**PDA@MNPs. Corresponding histograms and statistician charts are showed for both of them in **A.2)** and **B2)**, respectively. (N: counts, X: average size, SD: standard deviation)

Regarding TEM analysis, the first analyzed sample was bare MNPs. HREM image on **Figure 27 (A)** shows its planar distance, which was about 2.99 Å. Moreover, the Digital Diffraction Patterns (DDP) built from the previous HREM image allowed us to corroborate the composition of the magnetic nanoparticles. The distance between planes (interplanar spacing) in the reciprocal lattice was about 2.40Å and 3.385Å for planes [222] and [220], respectively, as seen in **Figure 27 (B)**, which are very close to the typical planes of magnetite phase (Fe_3O_4)[128]. The HAADF image on **Figure 28 (A)** represents a MNPs cluster, whose compositional mapping is reported in same figure with letter **B**. In this map, the green dots represent O atoms, while Fe atoms can be seen as red dots. As it can be observed from both images, they can be clearly overlapped, corroborating the composition of the MNPs.
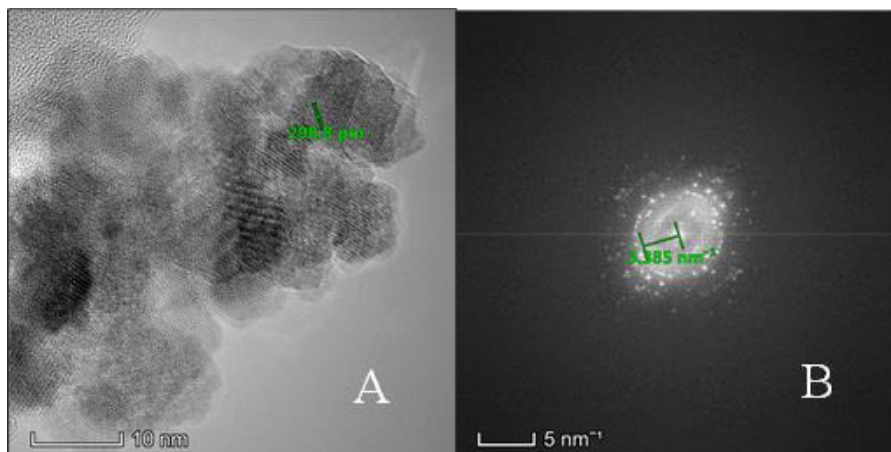
Figure 27. A) TEM micrograph of MNPs taken at HREM mode, B) Digital Diffraction Pattern (DDP) built from A.

Concerning EDS analyses, **Figure 28 (C)**, it can be seen that the composition of the sample is: C, Cu, O and Fe; the first two associated to the grid, and the last two to the sample (Fe_3O_4 MNPs).
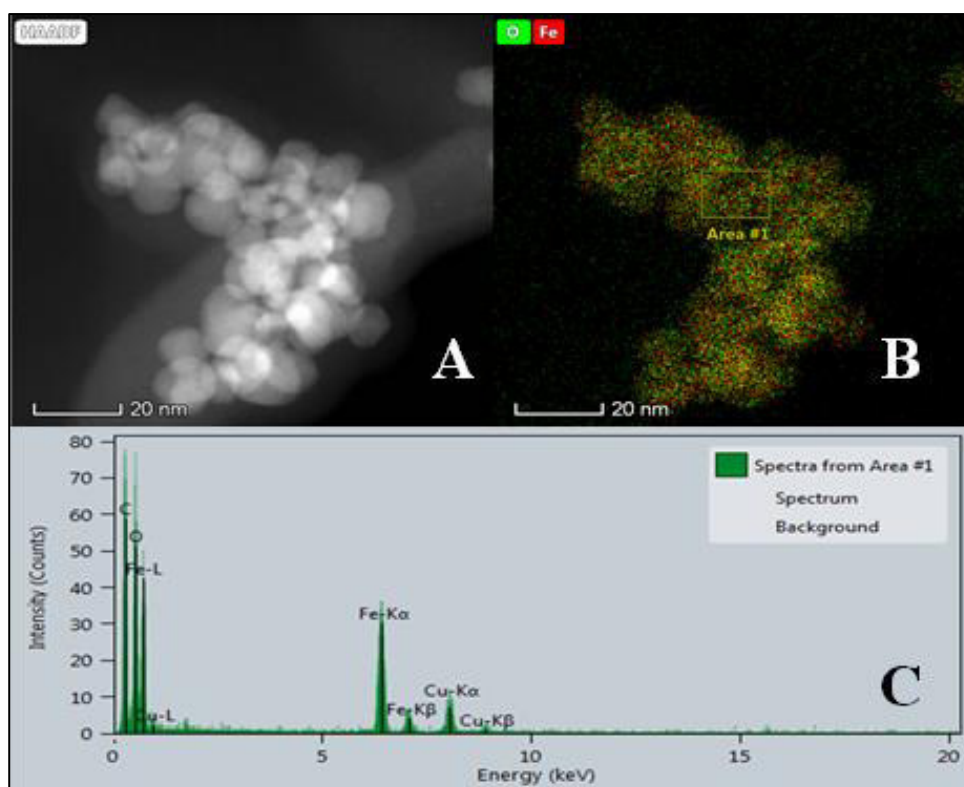
Figure 28. TEM analysis of bare MNPs. A) TEM micrograph of a MNPs cluster taken at HAADF mode, **B)** Compositional mapping from image A and **C)** EDS spectrum of image letter A

PDA@MNPs were the second sample analyzed through TEM. The micrograph at HREM mode was taken first, and consequently the DDP was built from the previous micrograph. The planar distance measured from the HREM image was about 2.94Å as shown in **Figure 29 (A),** whilst the interplanar spacing was about 3.388Å for plane [220] as observed in **Figure 29 (B)**, which is very close to the distance of 2.97Å corresponding to the [2 2 0] family planes of face-centered cubic (FCC) crystals from magnetite phase (Fe_3O_4)[128].
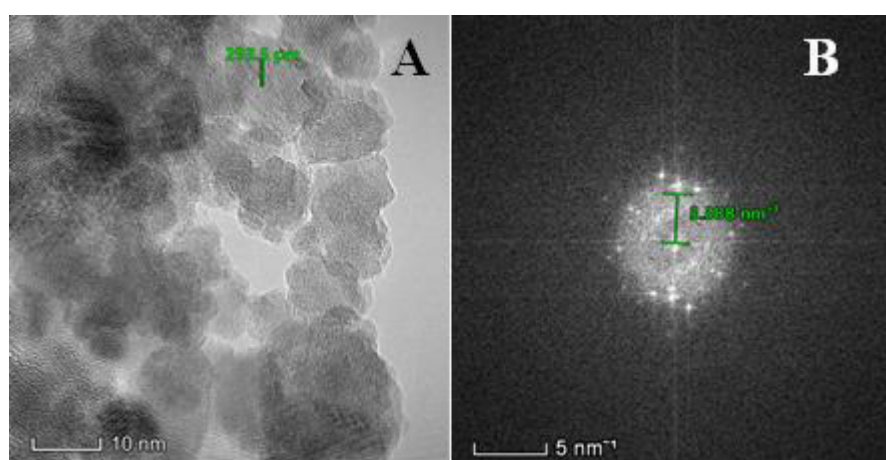
Figure 29. A) TEM micrograph of PDA@MNPs taken at HREM mode,
B) Digital Diffraction Pattern (DDP) built from A

The HAADF image letter **A** on **Figure 30** represents a MNPs cluster, whose compositional mapping is reported in same figure with letter **B**. In this map, the green dots represent O atoms, while Fe atoms can be seen as red dots and C as blue dots. Origin of C atoms can be either contamination or PDA cover. As it can be observed from both images, they can be clearly overlapped, corroborating the composition of the MNPs. The EDS spectrum of this sample represented by letter **C** on **Figure 30**, shows that the composition of C and O (semi-quantitatively) seems to be higher than for bare MNPs, since the peaks corresponding to these two atoms are more intense, suggesting that in this case, the excess of C and O atoms belong to the PDA cover surrounding the clusters of MNPs.
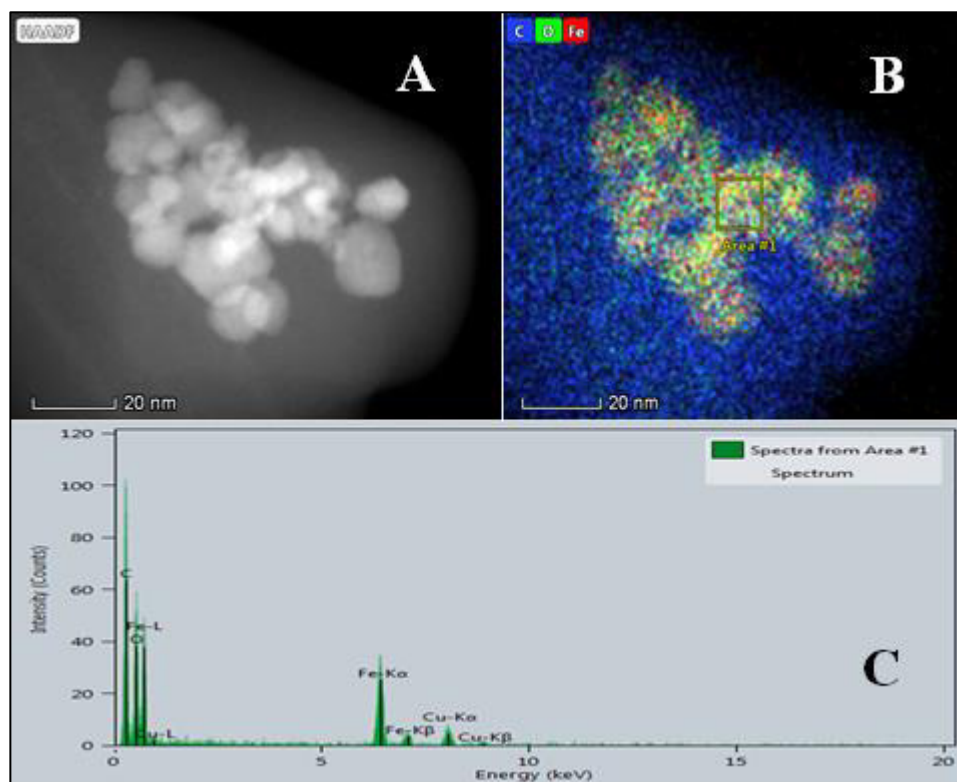
Figure 30. TEM analysis of PDA@MNPs. A) TEM micrograph of a MNPs cluster taken at HAADF mode, **B)** Compositional mapping from image A and **C)** EDS spectrum of image letter A

3.3.3. XRD

The crystalline arrangements of the bare and coated MNPs were characterized by XRD. All diffractograms showed a similar aspect (number and position of the peaks) as can be appreciated in **Figure 31**. The diffraction peaks of {220}, {311}, {400}, {422}, {511} and {440} reflect the MNPs crystal with a cubic inverse spinel structure with oxygen forming a face centering closed (fcc) packing and Fe cations occupying interstitial tetrahedral and octahedral sites[40] as can be observed in **Figure 32**; and they match well with those of the bulk Fe_3O_4 (Powder Diffraction File (PDF) No. 88-0315, 2002[129]).

Their main reflections are shown in **Table 10**, proving that all the synthesized particles were magnetic and that after the functionalization of the particles, they did not change their structure.
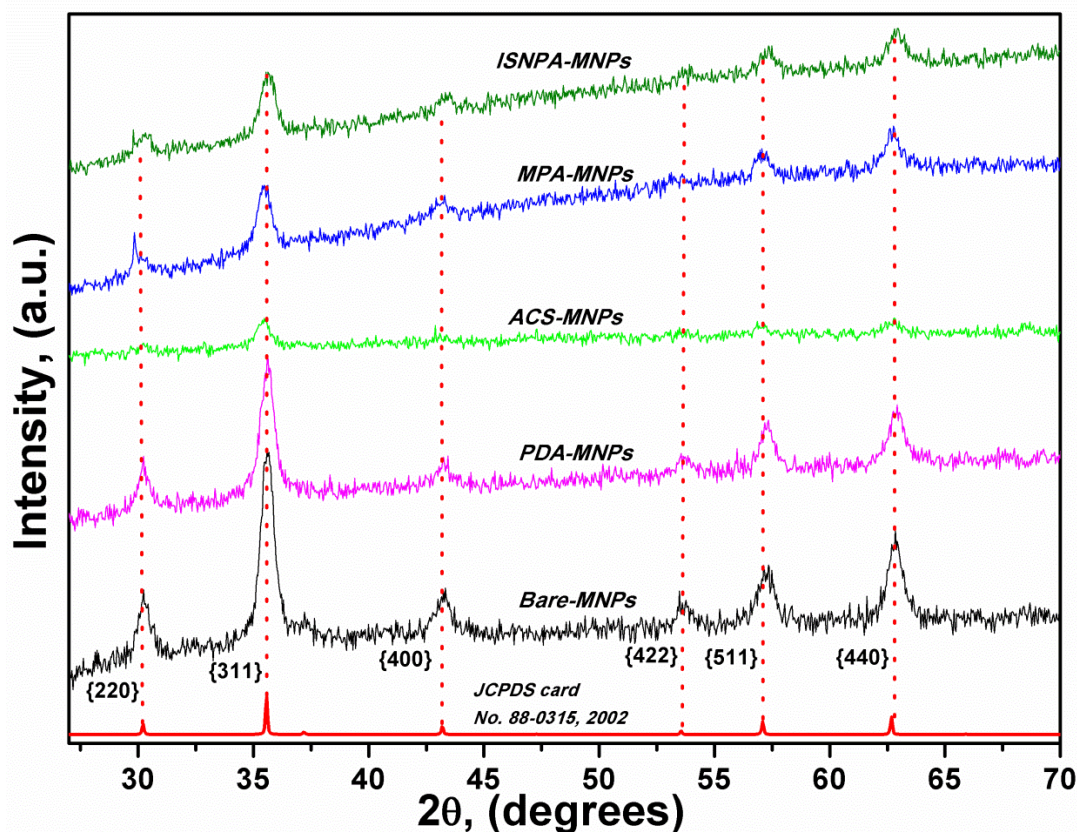
Figure 31. Diffractograms of the synthesized and functionalized MNPs, and the pattern card
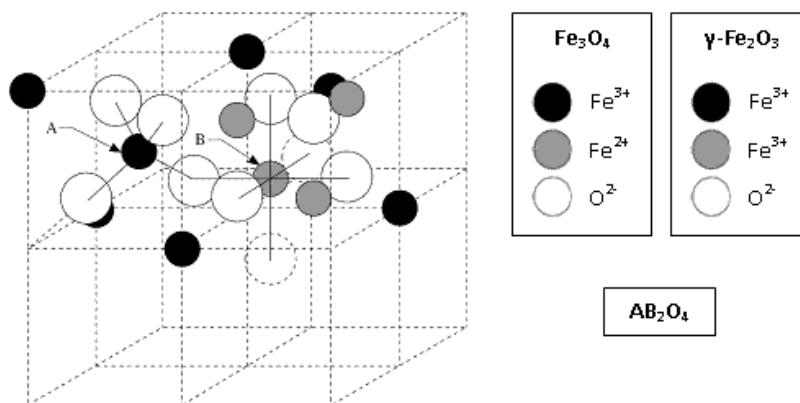
Figure 32. Structure of Magnetic Nanoparticles.

The particle diameter can be estimated using Scherrer equation. The sizes were calculated from the most intense reflection (Bragg angle, $2\theta \approx 35.5°$) shown in **Table 10**.

Sample	h k l	220	311	400	422	511	440
PDF No. 88-0315, 2002.	2Θ (degrees)	30.1	35.5	43.1	53.5	57.1	62.7
Bare MNPs	2Θ (degrees)	30.2	35.6	43.2	53.5	57.2	62.8
PDA@ MNPs	2Θ (degrees)	30.2	35.6	43.2	53.6	57.2	62.9
ACS@ MNPs	2Θ (degrees)	30.3	35.4	43.1	53.4	57.0	62.6
MPA@ MNPs	2Θ (degrees)	30.1	35.5	43.1	53.6	57.1	62.7
ISNPA@ MNPs	2Θ (degrees)	30.2	35.6	43.3	53.7	57.3	62.8

Table 10. Main reflections of MNPs (Pattern and different samples).

As observed in **Table 11**, the particle sizes obtained from **Figure 31** through Scherrer equation fit well with that obtained from SEM analyses. Sizes are almost the same in all of them, except for bare MNPs, which is exactly the same, what could suggest a predominantly monocrystalline structure of the synthesized MNPs.

 It can also be proved until now by XRD means, as well as with SEM, that bare MNPs have a similar particle size and were properly functionalized without losing their superparamagnetic properties and can be used in the proposed applications.

 Nevertheless, further characterization with FTIR and TGA were performed to evaluate whether the expected ligands of the coating agents could be found or not.

Sample	K Dimensionless Shape factor	λ X-ray wavelength (nm)	β FWHM (degrees)	2θ Bragg angle (degrees)	Particle size (nm)	
					τ (Scherrer equation)	SEM
Bare MNPs			0.65	35.63	13	13
PDA@MNPs			0.59	35.62	14	16
ACS@MNPs	0.9	0.15406	0.54	35.46	15	16
MPA@MNPs			0.65	35.47	14	15
ISNPA@MNPs			0.64	35.63	13	14

Table 31. Different particle sizes for the synthesized and functionalized MNPs obtained by XRD and SEM analyses.

3.3.4. FTIR

FTIR absorption spectra were performed to investigate the composition of the synthesized MNPs, in addition to examine and prove the proper coating of their surfaces detecting the functional groups due to ligands. **Figure 33** shows the FTIR spectrum of bare MNPs where a broad band can be observed in the zone of low frequencies (600 cm^{-1}) corresponding to the characteristic vibrations of Fe-O (570-600[20,121,130]). It is noteworthy the splitting-up of this peak what is attributed to the symmetry degeneration on the octahedral B sites[130] and the split of the energy levels of the quantized MNPs[131].

Moreover, the bands appearing at 3433 and 1629 cm^{-1} are assigned to the stretching and bending vibrations, respectively, of the surface hydroxyl groups and adsorbed water molecules[121,132].

On the other hand **Figure 34** represents the FTIR spectra of coated MNPs with the different acids, where the objective was to find the characteristic bands of the carboxylic groups. In fact, two bands around 1400-1420 and 1580-1600 cm^{-1} can be observed in all spectra, which can be assigned to the specific symmetric and asymmetric stretching vibrations of the carboxylate group (COO-)[133], respectively. However, in the spectra of ACS and MPA there is a small band at 1713 cm^{-1}, which may be attributed to the presence of some protonated carboxylic groups (COOH)[134], since the pKa´s of ACS are 3.13, 4.76, and 6.40, and that of MPA is 4.34, and the final pH of the solutions where these functionalization were performed were 5.4 and 5.2, respectively. Additionally the characteristic broad band of MNPs is kept in the zone of low frequencies, what demonstrates that the coating agents were bonded to the surface of the MNPs as the esterification occurs between the carboxyl group from acid molecules and the hydroxyl groups on the surface of the MNPs, without transforming them.
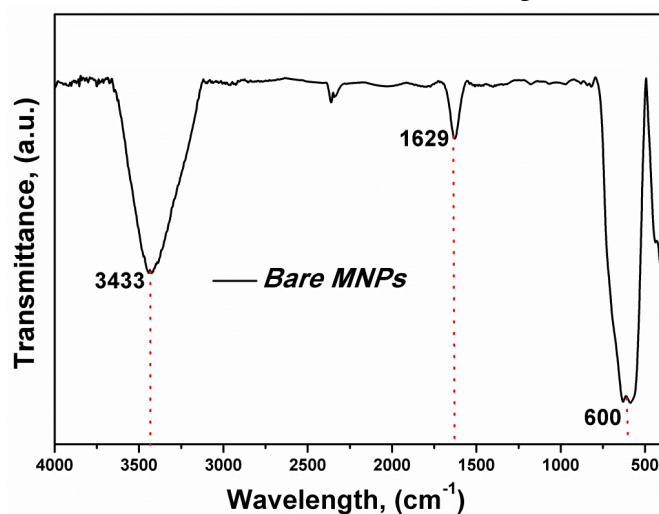
Figure 33. IR spectrum of the synthesized bare MNPs.
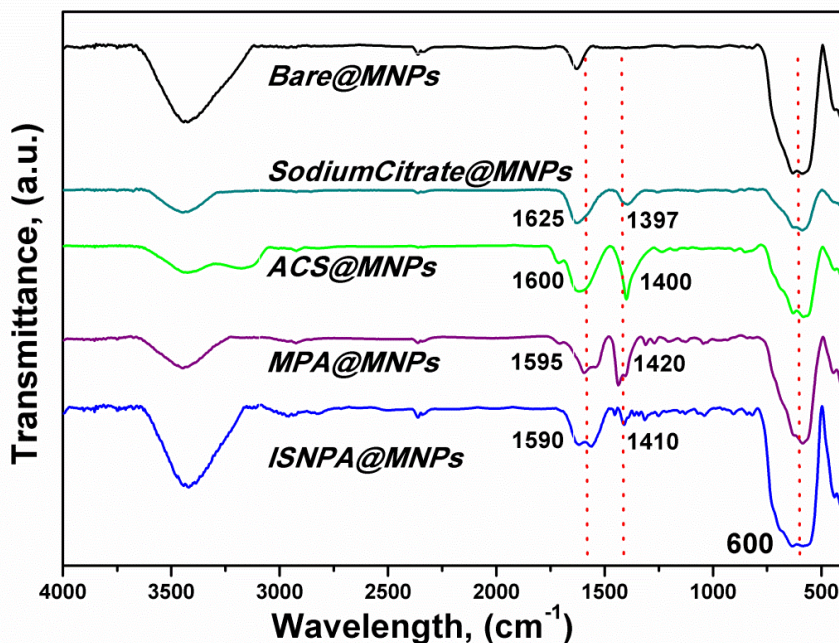
Figure 34. IR spectra of bare and functionalized MNPs with carboxyl groups. (SC@MNPs, ACS@MNPs, MPA@MNPs and ISNPA@MNPs).

The last two evaluated coating agents were PDA and CS. Their spectrum are presented in **Figure 35** where the characteristic broad bands of MNPs still appears at 600 cm^{-1} in both the functionalized MNPs. Colored in violet, the PDA@MNPs spectrum shows three more bands apart from the band at 600 cm^{-1}. The band at 1047 cm^{-1} is assigned to the ring breathing of ortho-disubstituted benzene rings, while the bands at 1490 and 1630 cm^{-1} are considered to be present due to the indoline structure of the polydopamine[135] as exemplified in **Figure 4**. On the other hand, colored in orange, the CS@MNPs spectrum presents three more bands as well, but attributed to different groups. The bands at 3427-3423 and 1633 cm^{-1} are assigned to the stretching and bending vibrations of the surface hydroxyl groups and adsorbed water molecules, respectively.[121]Additionally, the band at 1385 cm^{-1} was associated to water crystallization. According to these results, it was not possible to observe the characteristic bands of chitosan which were expected around at 1652 and 1594 cm^{-1} for amides I and II, respectively, as well as at 1080 cm^{-1} which represents the glycosidic linkage[121,136].

The presence of the characteristic band due to the specific vibrations of Fe-O were observed around the 600 cm^{-1} in all FTIR analyzed samples, as well as the characteristic bands for each of the coating agents except for chitosan, concluding and affirming, that

the obtained nanoparticles were properly synthesized and functionalized with PDA, ACS, MPA, ISNPA and SC.
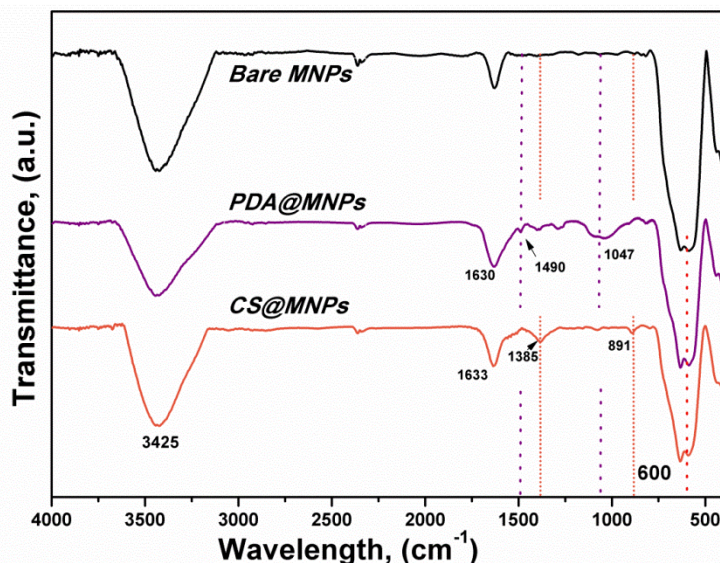
Figure 35. . IR spectra of bare and functionalized MNPs with polydopamine (PDA@MNPs) and chitosan (CS@MNPs)

3.3.5. TGA

In order to study the thermal stability of the synthesized nanomaterials, thermogravimetric analyses were performed and measured by percent mass loss as temperature increased as shown in the thermogram from **Figure 36**. It is observed that bare MNPs around 13 ± 3 nm, had a minimum mass loss of 4%, mainly attributed to desorption of water molecules within the crystallite structure[137]. Thus, it was expected to have mass losses above 4% in each of the following samples, since particle sizes obtained by SEM and XRD analyses were higher for the coated MNPs than the uncoated ones; the bigger the particle size the bigger mass loss should be.
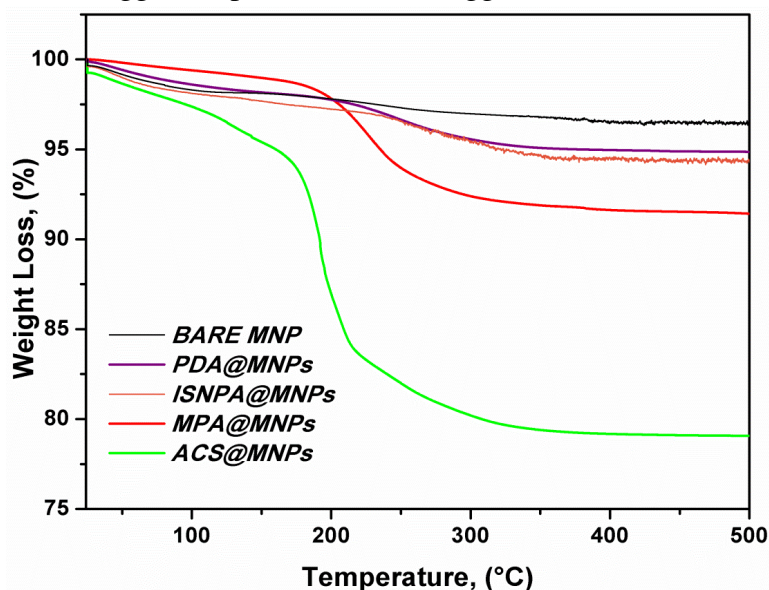
Figure 36. Thermograms of bare and functionalized MNPs. PDA, ISNPA, MPA and ACS.

According to **Table 12 and Figure 36**, ACS@MNPs presented a mass loss of 21% what indicates once again that MNPs were functionalized properly with this coating agent and fits well with the particle size previously obtained by SEM and XRD studies (16 and 15 nm, respectively). The same occurs for MPA@MNPs but in fewer amounts. It presented a mass loss about 9% which is also attributed to the covering agent, and as expected the mass loss was less than the obtained by ACS@MNPs as well as the particle size (SEM 15nm, XRD 14nm).

MNP	% Mass loss
Bare MNP	4
PDA-MNP	6
ISNPA-MNP	6
MPA-MNP	9
ACS-MNP	21

Table 12. Weight loss (%) from the different samples obtained by TGA analysis.

The particle size obtained by SEM once the MNPs were functionalized with ISNPA was 14 nm which was the smallest after the coating step; therefore a smaller mass loss was expected. In fact, that happened; ISNPA@MNPs only had a mass loss of 6% what fits well with the previous result. On the other hand, PDA@MNPs were expected to have a similar mass loss to ACS@MNPs since their particle sizes after the functionalization was practically the same (see **Figure 25 a.2** & **b.2**); however this did not occur, PDA@MNPs only had 6% mass loss what could be attributed to the high porosity of such coating agent according to the literature; obtaining large thickness but with high porosity[138].

These mass losses occurred mainly within the temperature range from 100 to 400°C where some effects take place such as decomposition of the physisorption (120-300°C) and the chemisorption (>440°C) of the coating agent on the surface of the MNPs[132].

3.4. Enzymatic inhibition study

The first aim of this study was to test if there was any interference among the different compounds used in the assays which may overlapped with the main signal. The absorbance had to be in a lineal range, and its value below 1.

The absorbance spectrums of all the compounds are shown in **Figure 37**. Either the PBS or H_2O_2 did not influence in the total absorbance.

The concentration of the MNPs was 0.25 mg/mL in order to avoid interferences, keeping a significant concentration of enzyme.

On the other hand the concentration of ABTS was 0.3 mg/mL to maintain the absorbance value within the linearity. Its absorbance spectrum in **Figure 37** shows two main peaks at 417 and 736 nm.
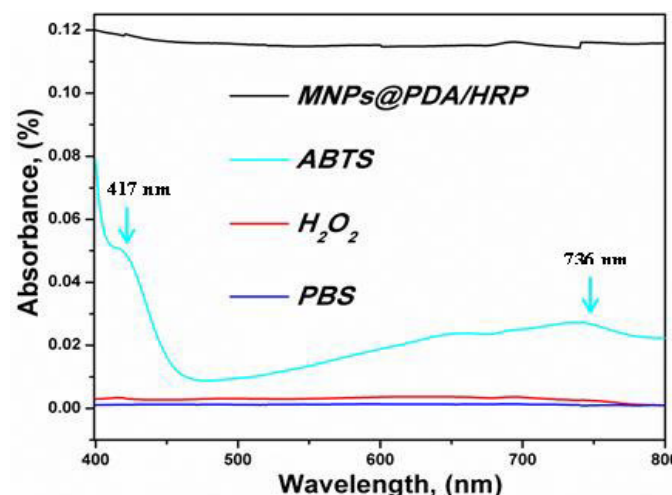
Figure 37. Absorbance spectrums of the different components, measured to test whether there was interferences among them or not.

The second objective of this inhibition enzymatic study was to prove how mercury is capable to inhibit the activity of HRP enzyme attached onto the surface of the functionalized PDA@MNPs. A possible inhibition scheme is presented by **Figure 38.**
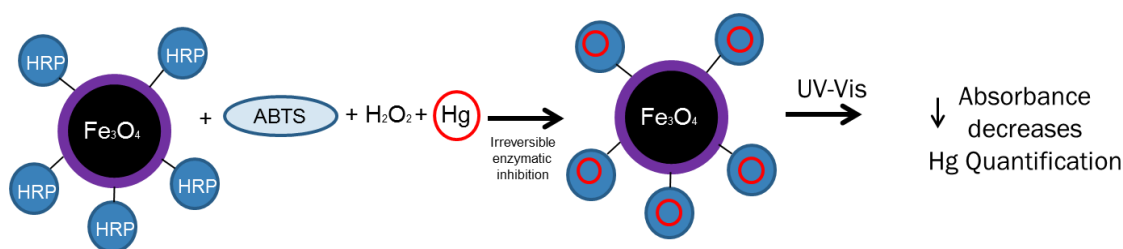
Figure 38. Inhibition of HRP enzyme attached onto the surface of MNPs caused by mercury.

To address these experiments, in first place, the ABTS signal (blank) was measured after 10 minutes of reaction (ABTS, H_2O_2 and PDA/HRP@ MNPs). **Figure 39** shows an intense signal on the absorbance (light blue line) due to an oxidation of ABTS molecules. Secondly, mercury (0.060 ppm) was introduced into the system in a different solution. After the same ten minutes when mercury was introduced into the reaction system, the absorbance of such solution was measured. On **Figure 39** it is possible to appreciate how the absorbance value of the ABTS signal is decreased.

Considering this result, it is evident how mercury affects the reaction, what indicates that this harmful metal is a peroxide enzyme inhibitor reducing irreversibly and significantly its catalytic activity.
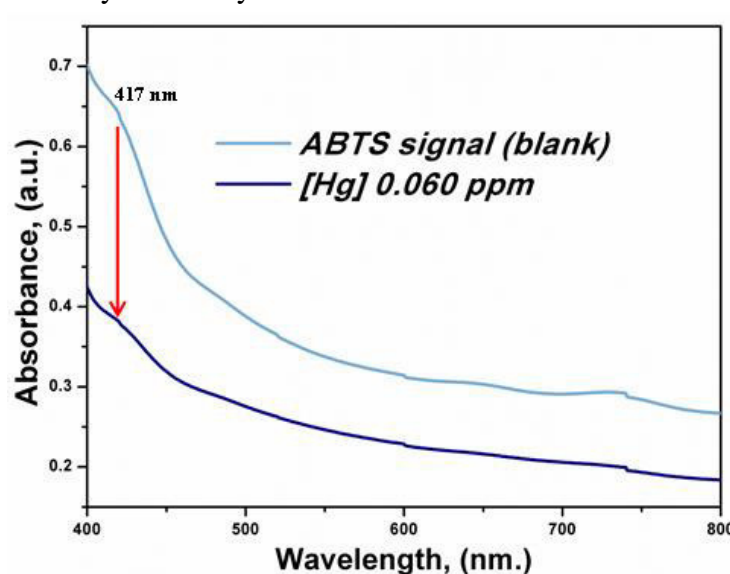
Figure 39. Reduction of the ABTS signal due to irreversible inhibition of HRP enzyme by mercury.

In this sense, different absorbance measurements at 417 nm were carried out according to **Table 6** to elaborate a calibration curve which can be appreciated in **Figure 40**.

	Blank	0.03	0.04	0.05	0.06
HgCl₂	-	2.9 µL	3.8 µL	4.83 µL	5.80 µL
PBS	1027.5 µL	1024.6 µL	1023.7 µL	1022.7 µL	1021.7 µL
PDA/HRP@MNPs			7.5 µL		
ABTS			450 µL		
H₂O₂			15 µL		
Total Volume			1500 µL		

Table 6. Different solutions and their specific quantities used to perform the calibration curve

Concentration of each sample was represented on the "x" axis, and the absorbance difference with respect to the reference value (blank) on the "y" axis.

Once the calculations were done, it came out that the correlation coefficient (R^2) is 0.9936 what it means that the lineal adjustment is quite good. The Limit of Detection and Quantification (LOD and LOQ) were also calculated with values of 0.004 and 0.013 ppm, respectively, which are very close to the official limit according to EPA (2ppb = 0.002 ppm). Hence, this methodology is rather interesting and after improvement, can be proposed to determine mercury in natural waters.
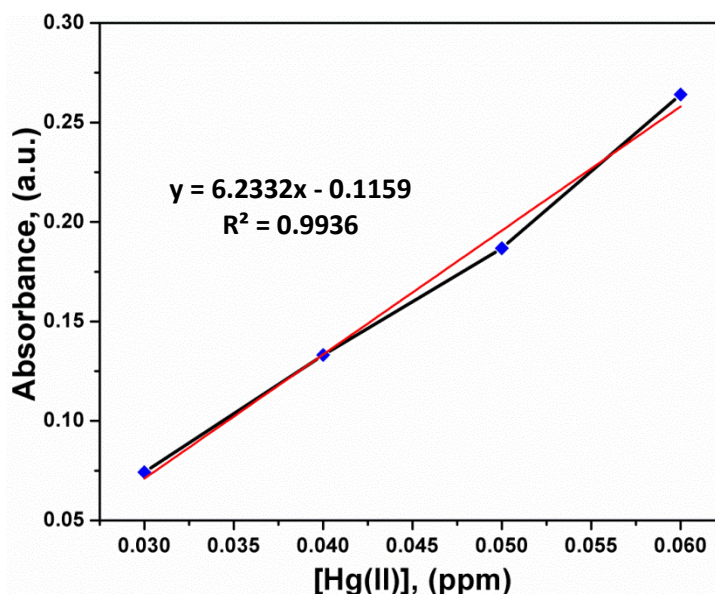
Figure 40. Calibration curve created from the enzymatic inhibition study at wavelength 417nm.

3.5. MNPs and Biomedicine

Another important aspect of this research was to apply the various MNPs synthesized and functionalized along this project to biomedical studies, in order to assess if they were able to detect a specific protein-TRIB2. In this context, MNPs were first coated with a specific homemade anti-TRIB2 antibody, analyzed to confirm the antibody attachment onto the MNPs and further applied to an immunoprecipitation assay. These results are presented in the next subsections.

3.5.1. Immobilization of the antibody onto the surface of MNPs

This part consisted on the attachment of the anti-TRIB2 antibody onto the surface of diverse MNPs (described on subsection 2.7) and their further corroboration through SDS-PAGE using Commasie brilliant blue. It is remarkable to remember from subsections 2.7 and 2.9.3, that all the attachment processes were performed in duplicate, one at room temperature and the other one at 4°C. In this context, **Figure 41** represents the binding evaluation of all the functionalized MNPs, which were coated during this project as described on subsection 2.4. The numbers on the left of each gel represent the pattern of the blue protein marker (with protein sizes taken from **Figure 42**). The first column refers to the band of the anti-TRIB2 polyclonal antibody. Lane 2 refers to the negative control for the MNPs where nothing should be observed due to the inexistence of antibody.
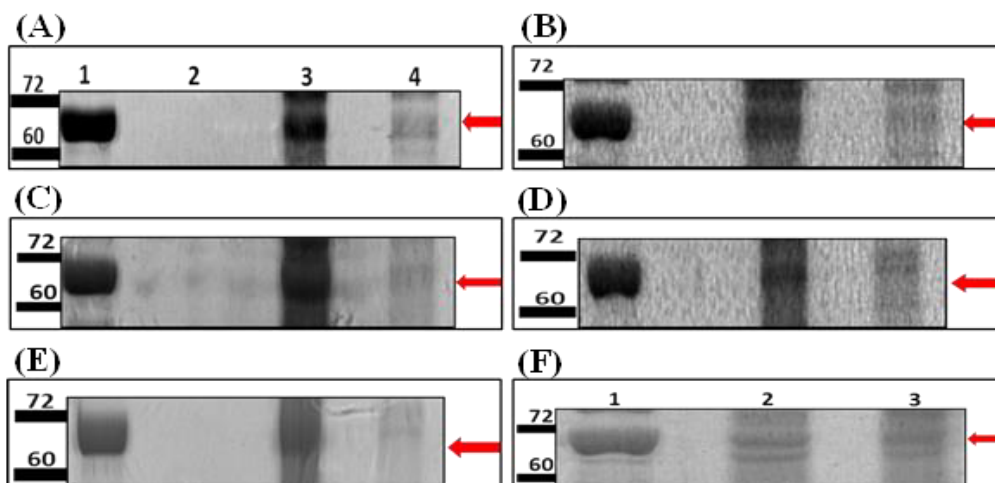
Figure 41. SDS-PAGE with Coomassie brilliant blue for the evaluation of the antibody attachment over different functionalized MNPs. Different coated MNPs were used to bind anti-TRIB2 antibody onto their surfaces. (A) Polydopamine@MNPs, (B) Citric acid@MNPs, (C) Mercaptopropionic acid@MNPs, (D) Isonipecotic acid@MNPs, (E) Chitosan@MNPs and (F) Sodium cirate@MNPs. Lane 1 refers to the polyclonal TRIB2 antibody. Lane 2 refers to the negative control in which bare MNPs were used. Lane 3 and 4 from gels A to E refer to MNPs conjugated with TRIB2 antibody. The linking process from lane 3 was carried out at room temperature and the one from lane 4 at 4°C. Thus, bands appearing on these two columns of each gel are attributed to the anti-TRIB2 antibody attached onto the MNPs surface. Lane 2 from gel F refers to bare MNPs employed to make the linking process whilst MNPs employed on column number five were SC@MNPs. Both of them presented antibody attachment at room temperature. Numbers on the left of each gel make reference to the blue protein marker.
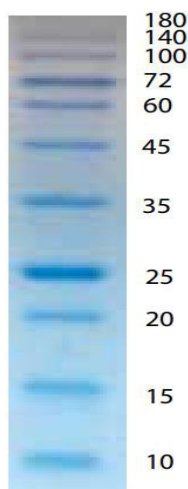
Figure 42. Blue protein marker pattern.

Lane 3 and 4 represent the band of the polyclonal antibody attached at different temperature over different coated MNPs. Analyzing lane 1 from **Figure 41** we can observe that the antibody has an intense band between 72 and 60 kDa. Thus, bands on lanes 3 and 4 which are at the same level were attributed to the antibody. Nonetheless, bands on lane three are somehow more intense than those on lane four. This same behavior was present in all of the evaluations as shown in the same **Figure 41**.

Figure 41 (F), shows binding efficiency of TRIB2 antibody to bare MNPs and SC@MNPs. This experiment was performed in order to assess whether the homemade anti-TRIB2 antibodies were able or not to attach onto the surface of uncoated MNPs. It was found that the antibody could also attach onto the surface of MNPs with any sort of coating agent. This might be due to the hydroxyl groups negatively charged present onto the surface of MNPs which interacts with a positive area of the antibody producing the union. However, it was also found that the amount of antibody attached onto the coated MNPs, in this case SC@MNPs, was more intense than the amount present onto the uncoated ones. Thus, the coating agents can significantly increase the attachment of the antibody to the MNPs.

With these results, it was found that this specific homemade TRIB2 polyclonal antibody is stable and binds better to coated MNPs at room temperature than to uncoated MNPs at 4°C. For this reason, the following immunoprecipitation experiments were performed with TRIB2-MNPs obtained at room temperature.

3.5.2. Immunoprecipitation reactions results

After certifying the antibody was present onto the surface of the different MNPs, three immunoassays were performed. The first one was employing SC/Ab@MNPs and a protein solution 4µg/mL, the second and third ones were using PDA/Ab@MNPs and CS/Ab@MNPs with protein solutions 2µg/mL each. The reason for using these different MNPs and different protein concentrations was to compare the behavior of the three different coating agents which had different composition and to assess if the MNPs could still detect the suppressor protein by decreasing the initial concentration 50%. The results of the immunoassays are shown in **Fig. 43.**
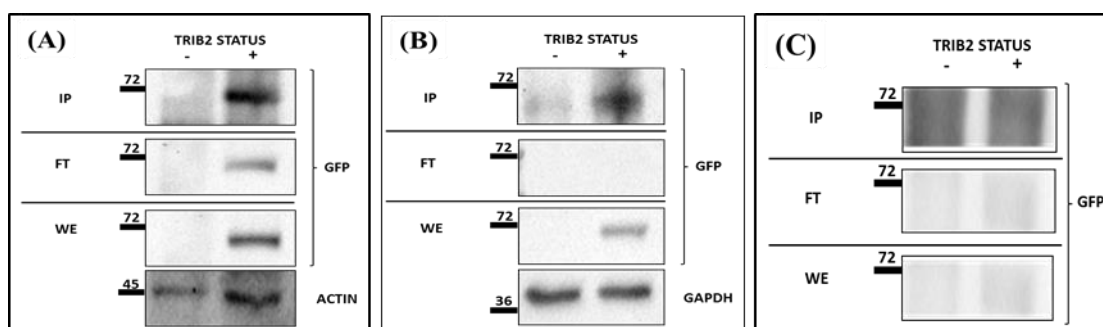
Figure 43. IP-WB assays results for three independent immunoprecipitation experiments employing different coated MNPs.
A, B and C refer to three independent immunoassays. Sodium citrate/Antibody coated MNPs were used in A. Polydopamine/Antibody coated MNPs were used in B. Chitosan/Antibody coated MNPs were used in C. Two different cell lines were tested (U2OS parental and TRIB2-GFP). Three primary antibodies (GFP, Actin and GAPDH) and fractions were evaluated. "IP" fraction makes reference to immunoprecipitation, "FT" to flow through and "WE" to whole extract. The signal of these fractions was at 72kDa for GFP antibody whilst the signal of Actin and GAPDH were at 45 and 36kDa, respectively. IPs A and B expressed the target protein while IP C did not. The WE results confirmed the high selectivity presented by the homemade antibody.
.

The previous IP-WB confirmed the identity of the IP bands corresponding to the antibody-antigen complex components. The tested samples by IP-WB were two protein extracts from two isogenic cell lines; an osteosarcoma cell line which expressed the target protein (TRIB2-GFP) and the parental cell line which did not overexpressed the target protein.   In addition to the immunoprecipitated fraction, we also collected two more fractions for each of the three IPs. The flow-though (FT) and the whole cell lysate extract (WE).

We used the GFP antibody as an alternative method to detect TRIB2 presence, since TRIB2 is fused to GFP in this cell line. Actin and GAPDH proteins refer to housekeeping genes which protein levels are stably expressed. The expression analysis of these proteins allowed us to confirm that the same amount of protein is loaded in each lane and variations on the binding affinity of TRIB2 to the different MNPs are significant.

In this context, **Figure 43** displays the outcomes for the three IPs, FT and WE. IP coded with letter C did not show the corresponding band at 72 kDa attributed to the presence of TRIB2 antigen, which might be explained as a matter of human error during the managing of the Western Blot. However, on IPs A and B it is possible to observe the expected band at 72 kDa. In fact, we can appreciate how the band of the IP A is a bit more intense than the one from the IP B. This is perfectly understandable due to the different concentration in the initial protein solution. In the same regard, it is also noticeable how the band which is showed up on FT from IP A is less intense than the one from the IP fraction, what lead us to think that most of the TRIB2 was detected by SC/Ab@MNPs and the excess was removed, which is the one that appears on the FT. A similar thing occurred in IP B; nonetheless the FT section from this experiment did not present the band which is attributable to a complete TRIB2 detection by PDA/Ab@MNPs that is possibly explained by virtue of having less concentration of this suppressor protein and more antibodies to react with. The last evaluated fraction is the WE. Three primary antibodies were employed, GFP, actin and GAPDH which interacted with their specific proteins from the protein extract. Using GFP antibodies we demonstrated that TRIB2 reacted with our polyclonal antibodies, due to these two proteins were linked. On the other hand, with the use of actin and GAPDH we showed that both protein extracts had the same molecules and that our antibodies were able to differentiate and react selectively with TRIB2 no matter the content of the extract. With this final evaluation it was possible to demonstrate how the antibody attached on the coated MNPs was able to detect in a selective and specific manner with high efficiency the target protein –TRIB2.

4. Conclusions

❖ During this project, conventional co-precipitation method was assisted by high power ultrasound, optimizing the reaction time that, to the best of our knowledge, this was the first time in which MNPs are synthesized within one single minute with great properties and with very low energy requirements ($\approx$2840J, 47.33W, and 0.87W/cm^3).

❖ The design of experiment permitted us to find out the best conditions (amplitude 40%, time: 1 min.) that affect the size and the size distribution of the nanoparticles. The presence of interactions between factors has also been shown.

❖ It was also possible to obtain very uniform magnetite particle sizes through this high power ultrasound-based approach (10 ± 2 nm).

❖ Proper functionalization of the MNPs has been successfully carried out using different molecules: polydopamine, citric acid, 3-mercaptopropionic acid, isonipecotic acid, and sodium citrate.

❖ Several characterization techniques were employed, such as DLS, SEM, TEM, STEM, TGA, DRX and FTIR which confirmed the attainment of a novel synthesis process producing excellent MNPs.

❖ Regarding the analytical application of this novel HRP-functionalized MNPs, it is noteworthy to mention that despite of time issues, it was possible to find a linear relationship between inhibitor concentration and absorbance that allowed showing a decrease in the enzyme catalytic activity in the presence of the analyte. It was shown that HRP is irreversibly inhibited by mercury being able to have some promising results aligned to those from EPA.

❖ The immunoprecipitation assays allowed us to confirm the efficacy of the MNPs binding to TRIB2 antibody and validate their functionality. From the three coated MNPs (SC,PDA,CS@MNPs) two of them (SC,PDA@MNPs) efficiently immunoprecipitated TRIB2 in our biological system.

❖ We have been successful on imunoprecipitating TRIB2 in cell lines that exogenously overexpress TRIB2, which means that TRIB2 protein levels are far more abundant than in normal biological setting.

Some future studies, which could be interesting to develop, might be the standardization of the proposed mercury detection method by the irreversible inhibition of HRP enzyme. It would be a good idea to continue these inhibition studies by the same element but with the other coated MNPs (ACS, MPA and ISNPA), since time was not enough for those experiments. In the same direction, a different analyte could be assessed with the different MNPs or a different enzyme could also be used for the irreversible inhibition. Moreover, further characterization with a vibrating-sample magnetometer (VSM) and through Mösbouer spectroscopy could be done in order to gather even more information about our MNPs.

It would be also of great interest to continue testing the efficacy of these MNPs in the endogenous TRIB2 protein. Additionally, these set of experiments have been performed with high concentration of TRIB2 antibody. It would be very important to titrate the amount of TRIB2 antibody needed as well as the amount of MNPs used in each IP experiment to reduce costs associated with this procedure. With this approach we would find the minimum detectable concentration of TRIB2 that the MNPs can react with.

5. Bibliography

(1)   H.A. Hassan, M. Small Things and Big Changes in the Developing World. *Science (80).* **2005**, *309*, 65–66.

(2)   Di Sia, P. An Analytical Transport Model for Nanomaterials. *J. Comput. Theor. Nanosci.* **2011**, *8* (1), 84–89.

(3)   Definition-Nanomaterials-Environment-European-Commission
        http://ec.europa.eu/environment/chemicals/nanotech/faq/definition_en.htm (accessed Jul 10, 2019).

(4)   Nowack, B.; Bucheli, T. D. Occurrence, Behavior and Effects of Nanoparticles in the Environment. *Environ. Pollut.* **2007**, *150* (1), 5–22.

(5)   Touri, R.; Moztarzadeh, F.; Sadeghian, Z.; Bizari, D.; Tahriri, M.; Mozafari, M. The Use of Carbon Nanotubes to Reinforce 45S5 Bioglass-Based Scaffolds for Tissue Engineering Applications. *Biomed Res. Int.* **2013**, 1–8.

(6)   Mozafari, M.; Moztarzadeh, F.; Seifalian, A. M.; Tayebi, L. Self-Assembly of PbS Hollow Sphere Quantum Dots via Gas–bubble Technique for Early Cancer Diagnosis. *J. Lumin.* **2013**, *133*, 188–193.

(7)   Rezvani, Z.; Venugopal, J. R.; Urbanska, A. M.; Mills, D. K.; Ramakrishna, S.; Mozafari, M. A Bird's Eye View on the Use of Electrospun Nanofibrous Scaffolds for Bone Tissue Engineering: Current State-of-the-art, Emerging Directions and Future Trends. *Nanomedicine Nanotechnology, Biol. Med.* **2016**, *12* (7), 2181–2200.

(8)   Zarzuela, R.; Luna, M. J.; Gil, M. L. A.; Ortega, M. J.; Palacios-Santander, J. M.; Naranjo-Rodríguez, I.; Delgado, J. J.; Cubillana-Aguilera, L. M. Analytical Determination of the Reducing and Stabilization Agents Present in Different Zostera Noltii Extracts Used for the Biosynthesis of Gold Nanoparticles. *J. Photochem. Photobiol. B Biol.* **2018**, *179*, 32–38.

(9)   Saleh, T. A.; Gupta, V. K. *Nanomaerial and Polymer Membranes: Synthesis , Classification , and Properties of Nanomaterials*; Elsevier; **2016**; Vol. 101, p 284.

(10)   Huang, J.; Han, B.; Yue, W.; Yan, H. Magnetic Polymer Microspheres with Polymer Brushes and the Immobilization of Protein on the Brushes. *J. Mater. Chem.* **2007**, *17* (36), 3812–3818.

(11)   US EPA, O. National Primary Drinking Water Regulations https://www.epa.gov/ground-water-and-drinking-water/national-primary-drinking-water-regulations#one (accessed Jul 11, 2019).

(12)   Calnan, D. R.; Brunet, A. The FoxO Code. *Oncogene* **2008**, *27* (16), 2276–2288.

(13)   Van Der Heide, L. P.; Hoekman, M. F. M.; Smidt, M. P. The Ins and Outs of FoxO Shuttling: Mechanisms of FoxO Translocation and Transcriptional Regulation. *Biochem. J.* **2004**, *380* (Pt 2), 297–309.

(14)   Eyers, P. A.; Keeshan, K.; Kannan, N. Tribbles in the 21st Century: The Evolving Roles of Tribbles Pseudokinases in Biology and Disease. *Trends Cell Biol.* **2017**, *27* (4), 284–298.

(15)   Xu, H.-L.; Mao, K.-L.; Huang, Y.-P.; Yang, J.-J.; Xu, J.; Chen, P.-P.; Fan, Z.-L.; Zou, S.; Gao, Z.-Z.; Yin, J.-Y.; Xiao, J.; Lu,C.-T.; Zhang, B.-L.; Zhao, Y.-Z. Glioma-Targeted Superparamagnetic Iron Oxide Nanoparticles as Drug-Carrying Vehicles for Theranostic Effects. *Nanoscale* **2016**, *8* (29), 14222–14236.

(16)   Jeon, H.; Kim, J.; Lee, Y. M.; Kim, J.; Choi, H. W.; Lee, J.; Park, H.; Kang, Y.; Kim, I.-S.; Lee, B.-H.; Hoffman, A.S.; Kim, W.J. Poly-Paclitaxel/Cyclodextrin-spion Nano-Assembly for Magnetically Guided Drug Delivery System. *J. Control. Release* **2016**, *231*, 68–76.

(17)   Massart, R. Preparation of Aqueous Magnetic Liquids in Alkaline and Acidic Media. *IEEE Trans. Magn.* **1981**, *17* (2), 1247–1248.

(18)   Faiyas, A. P. A.; Vinod, E. M.; Joseph, J.; Ganesan, R.; Pandey, R. K. Dependence of PH and Surfactant Effect in the Synthesis of Magnetite (Fe$_3$O$_4$) Nanoparticles and Its Properties. *J. Magn. Magn. Mater.* **2010**, *322* (4), 400–404.

(19)   Cabrera, L.; Gutierrez, S.; Menendez, N.; Morales, M. P.; Herrasti, P. Magnetite Nanoparticles: Electrochemical Synthesis and Characterization. *Electrochim. Acta* **2008**, *53* (8), 3436–3441.

(20)   Shen, L.; Qiao, Y.; Guo, Y.; Meng, S.; Yang, G.; Wu, M.; Zhao, J. Facile Co-Precipitation Synthesis of Shape-Controlled Magnetite Nanoparticles. *Ceram. Int.* **2014**, *40*, 1519–1524.

(21)   Cheng, J. P.; Ma, R.; Chen, X.; Shi, D.; Liu, F.; Zhang, X. B. Effect of Ferric Ions on the Morphology and Size of Magnetite Nanocrystals Synthesized by Ultrasonic Irradiation. *Cryst. Res. Technol.* **2011**, *46* (7), 723–730.

(22)   Slavov, L.; Abrashev, M. V; Merodiiska, T.; Gelev, C.; Vandenberghe, R. E.; Markova-Deneva, I.; Nedkov, I. Raman Spectroscopy Investigation of Magnetite Nanoparticles in Ferrofluids. *J. Magn. Mater.* **2010**, *322* (14), 1904-1911.

(23)   Casula, M. F.; Floris, P.; Innocenti, C.; Lascialfari, A.; Marinone, M.; Corti, M.; Sperling, R. A.; Parak, W. J.; Sangregorio, C. Magnetic Resonance Imaging Contrast Agents Based on Iron Oxide Superparamagnetic Ferrofluids. *Chem. Mater.* **2010**, *22* (5), 1739–1748.

(24)   Kim, E. H.; Ahn, Y.; Lee, H. S. Biomedical Applications of Superparamagnetic Iron Oxide Nanoparticles Encapsulated within Chitosan. *J. Alloys Compd.* **2007**, *434–435*, 633–636.

(25)   Karami, H. Heavy Metal Removal from Water by Magnetite Nanorods. *Chem. Eng. J.* **2013**, *219*, 209–216.

(26)   Johannsen, M.; Gneveckow, U.; Eckelt, L.; Feussner, A.; Waldöfner, N.; Scholz, R.; Deger, S.; Wust, P.; Loening, S. A.; Jordan, A. Clinical Hyperthermia of Prostate Cancer Using Magnetic Nanoparticles:

Presentation of a New Interstitial Technique. *Int. J. Hyperth.* **2005**, *21* (7), 637–647.

(27) Arruebo, M.; Fernández-Pacheco, R.; Ibarra, M. R.; Santamaría, J. Magnetic Nanoparticles for Drug Delivery. *Nano Today* **2007**, *2* (3), 22–32.

(28) Gu, H.; Xu, K.; Xu, C.; Xu, B. Biofunctional Magnetic Nanoparticles for Protein Separation and Pathogen Detection. *Chem. Commun.* **2006**, (9), 941.

(29) Cheng, J. P.; Zhang, X. B.; Yi, G. F.; Ye, Y.; Xia, M. S. Preparation and Magnetic Properties of Iron Oxide and Carbide Nanoparticles in Carbon Nanotube Matrix. *J. Alloys Compd.* **2008**, *455* (1–2), 5–9.

(30) Chin, K. C.; Chong, G. L.; Poh, C. K.; Van, L. H.; Sow, C. H.; Lin, J.; Wee, A. T. S. Large-Scale Synthesis of Fe₃O₄ Nanosheets at Low Temperature. *J. Phys. Chem. C* **2007**, *111* (26), 9136–9141.

(31) Cai, W.; Wan, J. Facile Synthesis of Superparamagnetic Magnetite Nanoparticles in Liquid Polyols. *J. Colloid Interface Sci.* **2007**, *305* (2), 366–370.

(32) T. J. Daou; G. Pourroy; S. Bégin-Colin; J. M. Grenèche; C. Ulhaq-Bouillet; P. Legaré; P. Bernhardt; C. Leuvrey; Rogez, G. Hydrothermal Synthesis of Monodisperse Magnetite Nanoparticles. *Chem. Mater.* **2006**, *18*, 4399–4404.

(33) Zou, G.; Xiong, K.; Jiang, C.; Li, H.; Wang, Y.; Zhang, S.; Qian, Y. Magnetic Fe₃O₄ Nanodisc Synthesis on a Large Scale via a Surfactant-Assisted Process. *Nanotechnology* **2005**, *16* (9), 1584–1588.

(34) Regazzoni, A. E.; Urrutia, G. A.; Blesa, M. A.; Maroto, A. J. G. Some Observations on the Composition and Morphology of Synthetic Magnetites Obtained by Different Routes. *J. Inorg. Nucl. Chem.* **1981**, *43* (7), 1489–1493.

(35) Peternele, W. S.; Monge Fuentes, V.; Fascineli, M. L.; Rodrigues da Silva, J.; Silva, R. C.; Lucci, C. M.; Bentes de Azevedo, R. Experimental Investigation of the Coprecipitation Method: An Approach to Obtain Magnetite and Maghemite Nanoparticles with Improved Properties. *J. Nanomater.* **2014**, *2014*, 1–10.

(36) Yazdani, F.; Seddigh, M. Magnetite Nanoparticles Synthesized by Co-Precipitation Method: The Effects of Various Iron Anions on Specifications. *Mater. Chem. Phys.* **2016**, *184*, 318–323.

(37) Sun, S.; Zeng, H. Size-Controlled Synthesis of Magnetite Nanoparticles. *J. Am. Chem. Soc.* **2002**, *124* (28), 8204–8205.

(38) Liang, X.; Wang, X.; Zhuang, J.; Chen, Y.; Wang, D.; Li, Y. Synthesis of Nearly Monodisperse Iron Oxide and Oxyhydroxide Nanocrystals. *Adv. Funct. Mater.* **2006**, *16* (14), 1805–1813.

(39) Ristić, M.; Kuzmann, E.; Homonnay, Z.; Musić, S. Synthesis and Properties of 1D Manganese-Doped Hematite Particles. *J. Alloys Compd.* **2018**, *767*, 504–511.

(40) Cornell, R. M.; Schwertmann, U. *The Iron Oxides : Structure, Properties, Reactions, Occurrences, and Uses*, , Wiley-VCH, **2003**, second edition, p 664.

(41) Mason, T. J. *Sonochemistry*; Oxford University Press, **1999**.

(42) Mason, T. J. Sonochemistry and Sonoprocessing: The Link, the Trends and (Probably) the Future. *Ultrason. Sonochem.* **2003**, *10* (4–5), 175–179.

(43) Cravotto, G.; Cintas, P. Forcing and Controlling Chemical Reactions with Ultrasound. *Angew. Chemie Int. Ed.* **2007**, *46* (29), 5476–5478.

(44) Suslick, K. S.; Hammerton, D. A.; Cline, R. E. Sonochemical Hot Spot. *J. Am. Chem. Soc.* **1986**, *108* (18), 5641–5642.

(45) Flint, E. B.; Suslick, K. S. The Temperature of Cavitation. *Science.* **1991**, *253* (5026), 1397–1399.

(46) Suslick, K. S. Sonochemistry. *Science* **1990**, *247* (4949), 1439–1445.

(47) Akbay, E.; Ölmez, T. G. Sonochemical Synthesis and Loading of PbS Nanoparticles into Mesoporous Silica. *Mater. Lett.* **2018**, *215*, 263–267.

(48) Acar Bozkurt, P. Sonochemical Green Synthesis of Ag/Graphene Nanocomposite. *Ultrason. Sonochem.* **2017**, *35*, 397–404.

(49) Sankar, S.; Kaur, N.; Lee, S.; Kim, D. Y. Rapid Sonochemical Synthesis of Spherical Silica Nanoparticles Derived from Brown Rice Husk. *Ceram. Int.* **2018**, *44* (7), 8720–8724.

(50) Yadav, R. S.; Kuřitka, I.; Vilcakova, J.; Havlica, J.; Kalina, L.; Urbánek, P.; Machovsky, M.; Skoda, D.; Masař, M.; Holek, M. Sonochemical synthesis of Gd³⁺ doped CoFe₂O₄ spinel ferrite nanoparticles and its physical properties. *Ultrason. Sonochem.* **2018**, *40*, 773–783.

(51) Wu, K.; Liu, D.; Lu, W.; Zhang, K. One-Pot Sonochemical Synthesis of Magnetite reduced Graphene Oxide Nanocomposite for High Performance Li Ion Storage. *Ultrason. Sonochem.* **2018**, *45*, 167–172.

(52) Bang, J. H.; Suslick, K. S. Applications of Ultrasound to the Synthesis of Nanostructured Materials. *Adv. Mater.* **2010**, *22* (10), 1039–1059.

(53) Harnchana, V.; Phuwongkrai, A.; Thomas, C.; Amornkitbamrung, V. Facile and Economical Synthesis of Superparamagnetic Magnetite Nanoparticles Coated with Oleic Acid Using Sonochemical Route. *Mater. Today Proc.* **2018**, *5* (6), 13995–14001.

(54) Cubillana-Aguilera, L. M.; Franco-Romano, M.; Gil, M. L. A.; Naranjo-Rodríguez, I.; Hidalgo-Hidalgo de

Cisneros, J. L.; Palacios-Santander, J. M. New, Fast and Green Procedure for the Synthesis of Gold Nanoparticles Based on Sonocatalysis. *Ultrason. Sonochem.* **2011**, *18* (3), 789–794.

(55) Anastas, P. T.; Heine, L. G.; Williamson, T. C. Green Chemical Syntheses and Processes: Introduction; **2000**; *ACS Stmposium Series,* Vol 767. pp 1–6.

(56) Gałuszka, A.; Migaszewski, Z.; Namieśnik, J. The 12 Principles of Green Analytical Chemistry and the significance Mnemonic of Green Analytical Practices. *TrAC Trends Anal. Chem.* **2013**, *50*, 78–84.

(57) Koel, M. Do We Need Green Analytical Chemistry? *Green Chem.* **2016**, *18* (4), 923–931.

(58) Franco-Romano, M.; Gil, M. L. A.; Palacios-Santander, J. M.; Delgado-Jaén, J. J.; Naranjo-Rodríguez, I.; Hidalgo-Hidalgo de Cisneros, J. L.; Cubillana-Aguilera, L. M. Sonosynthesis of Gold Nanoparticles from a Geranium Leaf Extract. *Ultrason. Sonochem.* **2014**, *21* (4), 1570–1577.

(59) Gil Montero, M. L. A.; Luna Aguilera, M. J.; Zarzuela Sánchez, R.; Cubillana Aguilera, L. M.; Palacios Santander, J.M.; Naranjo Rodriguez, I.; Hidalgo Hidalgo de Cisneros, J. L.; Garrido Crespo, C.; Carbu Espinosa de los Monteros, M.; Gonzalez Rodriguez, V.E.; Cantoral Fernandez, J.M. Síntesis de Nanopartículas de Oro Empleando Extracto Envejecido de Hojas de Drago (Dracanea Draco L): Procedimiento de Fabricación y Utilización, ES 2580009 B2, Dec, 15, **2016**.

(60) González-Álvarez, R. J.; Naranjo-Rodríguez, I.; Hernández-Artiga, M. P.; Palacios-Santander, J. M.; Cubillana-Aguilera, L.; Bellido-Milla, D. Experimental Design Applied to Optimisation of Silica Nanoparticles Size Obtained by Sonosynthesis. *J. Sol-Gel Sci. Technol.* **2016**, *80* (2), 378–388.

(61) Lopez Iglesias, D.; Garcia Romero, M.; Cubillana-Aguilera, L. M.; Palacios-Santander, J. M.; Naranjo-Rodríguez, I.; Bellido-Milla, D. Materiales Compuestos Sonogel-Carbono-Polimeros Conductores y Sus Variantes: Procedimiento de Fabricacion y Su Aplicacion En La Constitucion de (Bio) Sensores Electroquimicos, ES 2670985 B2, Nov 13, **2018**.

(62) Laurent, S.; Roch, A.; Robic, C.; Forge, D.; Vander Elst, L.; Muller, R. N.; Port, M. Magnetic Iron Oxide Nanoparticles: Synthesis, Stabilization, Vectorization, Physicochemical Characterizations, and Biological Applications. *Chem. Rev.* **2008**, *108* (4), 2064–2110.

(63) Laurent, S.; Forge, D.; Port, M.; Roch, A.; Robic, C.; Elst, L. Vander; Muller, R. N. Magnetic Iron Oxide Nanoparticles : Synthesis , Stabilization , Vectorization , Physicochemical Characterizations , and Biological Applications. *Chem. Rev* **2008**, *108*, 2064–2110.

(64) Hurley, M. J.; Jenner, P. What Has Been Learnt from Study of Dopamine Receptors in Parkinson's Disease? *Pharmacol. Ther.* **2006**, *111* (3), 715–728.

(65) Giovanni, D. G.; Matteo, B. Di; Esposito, E. *Serotonin-Dopamine Interaction: Experimental, Clinical and Therapeutic Evidence*; Elsevier; **2008**; Vol. 172. p 650.

(66) Lee, H.; Rho, J.; Messersmith, P. B. Facile Conjugation of Biomolecules onto Surfaces via Mussel Adhesive Protein Inspired Coatings. *Adv. Mater.* **2009**, *21* (4), 431–434.

(67) Lee, H.; Dellatore, S. M.; Miller, W. M.; Messersmith, P. B. Mussel-Inspired Surface Chemistry for Multifunctional Coatings. *Science* **2007**, *318* (5849), 426–430.

(68) Ashrafi, H.; Azadi, A. Chitosan-Based Hydrogel Nanoparticle Amazing Behaviors during Transmission Electron Microscopy. *Int. J. Biol. Macromol.* **2016**, *84*, 31–34.

(69) Moss, G. P.; Smith, P. A. S.; Tavernier, D. Glossary of Class Names of Organic Compounds and Reactivity Intermediates Based on Structure (IUPAC Recommendations 1995). *Pure Appl. Chem.* **1995**, *67* (8–9), 1307–1375.

(70) Tombácz, E.; Szekeres, M.; Hajdú, A.; Tóth, I. Y.; Andrea Bauer, R.; Nesztor, D.; Illés, E.; Zupkó, I.; Vékás, L. Colloidal Stability of Carboxylated Iron Oxide Nanomagnets for Biomedical Use. *Chem. Eng. J.* **2014**, *58*, 3–10.

(71) Jiménez-Hernández, L.; Estévez-Hernández, O.; Hernández, M. P.; Díaz, J. A.; Farías, M. F.; Reguera, E. On the State of Mn in MnxZn1−xO Nanoparticles and Their Surface Modification with Isonipecotic Acid. *J. Solid State Chem.* **2017**, *247*, 43–52.

(72) Venkateswarlu, S.; Himagirish Kumar, S.; Jyothi, N. V. V. Rapid Removal of Ni(II) from Aqueous Solution Using 3-Mercaptopropionic Acid Functionalized Bio Magnetite Nanoparticles. *Water Resour. Ind.* **2015**, *12*, 1–7.

(73) Müller-Schulte, D.; Füssl, F.; Lueken, H.; De Cuyper, M. A New Aids Therapy Approach Using Magnetoliposomes. In *Scientific and Clinical Applications of Magnetic Carriers*; Springer US: Boston, MA, **1997**; pp 517–526.

(74) Microtrac Europe GmbH. *Nanotrac Wave Particle Size, Zeta Potential and Molecular Weight Analyzer*; Meerbusch Germany.

(75) Pennycook, S. J.; Nellist, P. D. *Scanning Transmission Electron Microscopy: Imaging and Analysis*; Stephen J Penycook, Peter D Nellis, Eds.; Springer Science & Business Media, **2011**.

(76) Muller, D. A.; Grazul, J. *Optimizing the Environment for Sub-0.2 Nm Scanning Transmission Electron*

Microscopy; **2001**; Vol. 50.

(77) Patterson, A. L. The Scherrer Formula for X-Ray Particle Size Determination. *Phys. Rev.* **1939**, *56* (10), 978–982.

(78) Vitha, M. F. *Spectroscopy : Principles and Instrumentation*; John Wiley & Sons, Ltd, **2018**.

(79) Sun, D.-W. *Infrared Spectroscopy for Food Quality Analysis and Control*; Academic Press/Elsevier, **2009**.

(80) Rajisha, K. R.; Deepa, B.; Pothan, L. A.; Thomas, S. Thermomechanical and Spectroscopic Characterization of Natural Fibre Composites. *Interface Eng. Nat. Fibre Compos. Maximum Perform.* **2011**, 241–274.

(81) Dahima, R.; Gupta, A.; Rathore, D. Quality by Design (QbD) Approach for Formulation Development of Hydralazine Hydrochloride Tablets. *J. Chem. Pharm. Res.* **2016**, *8* (5), 336–341.

(82) Lawson, J. *Design and Analysis of Experiments with R*; CRC press; **2014**; p 620.

(83) Causton, D. Grafen, A., Hails, R. Modern Statistics for the Life Sciences. *Ann. Bot.* **2002**, *90* (6), 776–777.

(84) Mead, R. *The Design of Experiments : Statistical Principles for Practical Applications*; Cambridge University Press, **1988**.

(85) Moyaho, A.; Beristain-Castillo, E. Experimental Design: Basic Concepts. *Encyclopedia of Animal Behavior*; Academic Press/Elsevier, **2019**; pp 471–479.

(86) Cohen, J.; Medley, G. *Stop Working & Start Thinking : A Guide to Becoming a Scientist*; Taylor & Francis Group, **2005**.

(87) Ruxton, G. D.; Colegrave, N. *Experimental Design for the Life Sciences*; Oxford University Press, **2016**.

(88) Güvenç, A.; Kapucu, N.; Kapucu, H.; Aydoğan, Ö.; Mehmetoğlu, Ü. Enzymatic Esterification of Isoamyl Alcohol Obtained from Fusel Oil: Optimization by Response Surface Methodolgy. *Enzyme Microb. Technol.* **2007**, *40* (4), 778–785.

(89) Almeida e Silva, J.; Lima, U.; Taqueda, M. E.; Guaragna, F. Use of Response Surface Methodology for Selection of Nutrient Levels for Culturing Paecilomyces Variotii in Eucalyptus Hemicellulosic Hydrolyzate. *Bioresour. Technol.* **2003**, *87* (1), 45–50.

(90) Hao, J.; Fang, X.; Zhou, Y.; Wang, J.; Guo, F.; Li, F.; Peng, X. Development and Optimization of Solid Lipid Nanoparticles Formulation for Ophtalmic Delivery of Chloramphenicol Using Box-Behnken Design. *Int. J. Nanomedicine* **2011**, *6*, 683–692.

(91) Vasti, C.; Pfaffen, V.; Ambroggio, E.; Galiano, M. R.; Rojas, R.; Giacomelli, C. E. A Systematic Approach to the Synthesis of LDH Nanoparticles by Response Surface Methodology. *Appl. Clay Sci.* **2017**, *137*, 151–159.

(92) Liu, X.; Liu, W.; Wang, C.; Zheng, Z. Optimization and Modeling for One-Step Synthesis Process of Ag–Cu Nano-Particles Using DOE Methodology. *J. Mater. Sci. Mater. Electron.* **2016**, *27* (5), 4265–4274.

(93) Vázquez-González, M.; Carrillo-Carrion, C. Analytical Strategies Based on Quantum Dots for Heavy Metal Ions Detection. *J. Biomed. Opt.* **2014**, *19* (10), 1–12.

(94) Sharma, B.; Singh, S.; Siddiqi, N. J. Biomedical Implications of Heavy Metals Induced Imbalances in Redox Systems. *Biomed Res. Int.* **2014**, *2014*, 1–26.

(95) Farzin, L.; Shamsipur, M.; Sheibani, S. A Review: Aptamer-Based Analytical Strategies Using the Nanomaterials for Environmental and Human Monitoring of Toxic Heavy Metals. *Talanta* **2017**, *174*, 619–627.

(96) Katz, E.; Willner, I.; Wang, J. Electroanalytical and Bioelectroanalytical Systems Based on Metal and Semiconductor Nanoparticles. *Electroanalysis* **2004**, *16* (12), 19–44.

(97) Malitesta, C.; Di Masi, S.; Mazzotta, E. From Electrochemical Biosensors to Biomimetic Sensors Based on Molecularly Imprinted Polymers in Environmental Determination of Heavy Metals. *Front. Chem.* **2017**, *5*, 1–6.

(98) Yamada, H.; Yamazaki, I. Proton Balance in Conversions between Five Oxidation-Reduction States of Horseradish Peroxidase. *Arch. Biochem. Biophys.* **1974**, *165* (2), 728–738.

(99) Ostojić, J.; Herenda, S.; Bešić, Z.; Miloš, M.; Galić, B. Advantages of an Electrochemical Method Compared to the Spectrophotometric Kinetic Study of Peroxidase Inhibition by Boroxine Derivative. *Molecules* **2017**, *22* (7), 1120–1129.

(100) Miller', N. J.; Rice-Evans, C.; Davies2, M. 1; Gopinathan', V.; Milner', A. A Novel Method for Measuring Antioxidant Capacity and Its Application to Monitoring the Antioxidant Status in Premature Neonates. *Clin. Sci.* **1993**, *84*, 407–412.

(101) Wahajuddin; Arora, S. Superparamagnetic Iron Oxide Nanoparticles: Magnetic Nanoplatforms as Drug Carriers. *Int. J. Nanomedicine* **2012**, *7*, 3445–3471.

(102) Gabbasov, R.; Cherepanov, V.; Chuev, M.; Polikarpov, M.; Nikitin, M.; Deyev, S.; Panchenko, V. Biodegradation of Magnetic Nanoparticles in Mouse Liver From Combined Analysis of Mössbauer and Magnetization Data. *IEEE Trans. Magn.* **2013**, *49* (1), 394–397.

(103) Polikarpov, D.; Cherepanov, · V; Chuev, · M; Gabbasov, · R; Mischenko, · I; Nikitin, · M; Vereshagin, · Y; Yurenia, · A; Panchenko, · V. Mössbauer Evidence of 57 Fe 3 O 4 Based Ferrofluid Biodegradation in the Brain. *Hyperfine Interact* **2014**, *226*, 421–430.

(104) Xu, F.; Geiger, J. H.; Baker, G. L.; Bruening, M. L. Polymer Brush-Modified Magnetic Nanoparticles for His-

Tagged Protein Purification. *Langmuir* **2011**, *27* (6), 3106–3112.

(105) Hayashi, K.; Ono, K.; Suzuki, H.; Sawada, M.; Moriya, M.; Sakamoto, W.; Yogo, T. High-Frequency, Magnetic-Field-Responsive Drug Release from Magnetic Nanoparticle/Organic Hybrid Based on Hyperthermic Effect. *ACS Appl. Mater. Interfaces* **2010**, *2* (7), 1903–1911.

(106) Xie, J.; Liu, G.; Eden, H. S.; Ai, H.; Chen, X. Surface-Engineered Magnetic Nanoparticle Platforms for Cancer Imaging and Therapy. *Acc. Chem. Res.* **2011**, *44* (10), 883–892.

(107) Li, Z.; Yi, P. W.; Sun, Q.; Lei, H.; Li Zhao, H.; Zhu, Z. H.; Smith, S. C.; Lan, M. B.; Lu, G. Q. M. Ultrasmall Water-Soluble and Biocompatible Magnetic Iron Oxide Nanoparticles as Positive and Negative Dual Contrast Agents. *Adv. Funct. Mater.* **2012**, *22* (11), 2387–2393.

(108) Varshosaz, J.; Hassanzadeh, F.; Aliabadi, H. S.; Khoraskani, F. R.; Mirian, M.; Behdadfar, B. Targeted Delivery of Doxorubicin to Breast Cancer Cells by Magnetic LHRH Chitosan Bioconjugated Nanoparticles. *Int. J. Biol. Macromol.* **2016**, *93*, 1192–1205.

(109) Dhavale, R. P.; Waifalkar, P. P.; Sharma, A.; Dhavale, R. P.; Sahoo, S. C.; Kollu, P.; Chougale, A. D.; Zahn, D. R. T.; Salvan, G.; Patil, P. S.; Patil, P.B. Monolayer Grafting of Aminosilane on Magnetic Nanoparticles: An Efficient Approach for Targeted Drug Delivery System. *J. Colloid Interface Sci.* **2018**, *529*, 415–425.

(110) World Health Organization. *Press Release N° 263 Latest Global Cancer Data*; Geneva, **2018**.

(111) Baptista, I.; Gure, A. O.; Ferreira, B.; Ugurel, S.; Liu, N.; Adrienn, A.; Isbilen, M.; Dopazo, A.; Madureira, P. A.; Kiss-Toth, E.; Isbilen, M.; Gure, A.O.; Link, W. TRIB2 Confers Resistance to Anti-Cancer Therapy by Activating the Serine/Threonine Protein Kinase AKT. *Nat. Commun.* **2017**, *8*, 1–9.

(112) Cohen, P.; Tcherpakov, M. Will the Ubiquitin System Furnish as Many Drug Targets as Protein Kinases? *Cell* **2010**, *143* (5), 686–693.

(113) Liang, K.; Paredes, R.; Carmody, R.; Eyers, P.; Meyer, S.; McCarthy, T.; Keeshan, K. Human TRIB2 Oscillates during the Cell Cycle and Promotes Ubiquitination and Degradation of CDC25C. *Int. J. Mol. Sci.* **2016**, *17* (9), 1378.

(114) Zanella, F.; Renner, O.; García, B.; Callejas, S.; Dopazo, A.; Peregrina, S.; Carnero, A.; Link, W. Human TRIB2 Is a Repressor of FOXO That Contributes to the Malignant Phenotype of Melanoma Cells. *Oncogene* **2010**, *29* (20), 2973–2982.

(115) Grandinetti, K. B.; Stevens, T. A.; Ha, S.; Salamone, R. J.; Walker, J. R.; Zhang, J.; Agarwalla, S.; Tenen, D. G.; Peters, E. C.; Reddy, V. A. Overexpression of TRIB2 in Human Lung Cancers Contributes to Tumorigenesis through Downregulation of C/EBPα. *Oncogene* **2011**, *30* (30), 3328–3335.

(116) Wang, J.; Park, J.-S.; Wei, Y.; Rajurkar, M.; Cotton, J. L.; Fan, Q.; Lewis, B. C.; Ji, H.; Mao, J. TRIB2 Acts Downstream of Wnt/TCF in Liver Cancer Cells to Regulate YAP and C/EBPα Function. *Mol. Cell* **2013**, *51* (2), 211–225.

(117) Keeshan, K.; He, Y.; Wouters, B. J.; Shestova, O.; Xu, L.; Sai, H.; Rodriguez, C. G.; Maillard, I.; Tobias, J. W.; Valk, P.; Carrol, M.; Aster, J.C.; Delwel, R.; Pear, W.S. Tribbles Homolog 2 Inactivates C/EBPα and Causes Acute Myelogenous Leukemia. *Cancer Cell* **2006**, *10* (5), 401–411.

(118) Faiyas, A. P. A.; Vinod, E. M.; Joseph, J.; Ganesan, R.; Pandey, R. K. Dependence of PH and Surfactant Effect in the Synthesis of Magnetite (Fe_3O_4) Nanoparticles and Its Properties. *J. Magn. Magn. Mater.* **2010**, 400–404.

(119) Gnanaprakash, G.; Mahadevan, S.; Jayakumar, T.; Kalyanasundaram, P.; Philip, J.; Raj, B. Effect of Initial pH and Temperature of Iron Salt Solutions on Formation of Magnetite Nanoparticles. *Mater. Chem. Phys.* **2007**, *103* (1), 168–175.

(120) Qu, S.; Yang, H.; Ren, D.; Kan, S.; Zou, G.; Li, D.; Li, M. Magnetite Nanoparticles Prepared by Precipitation from Partially Reduced Ferric Chloride Aqueous Solutions. *J. Colloid Interface Sci.* **1999**, *215* (1), 190–192.

(121) El-Guendouz, S.; Aazza, S.; Lyoussi, B.; Bankova, V.; Lourenço, J. P.; Rosa Costa, A. M.; Mariano, J. F.; Miguel, M. G.; Faleiro, M. L. Impact of Biohybrid Magnetite Nanoparticles and Moroccan Propolis on Adherence of Methicillin Resistant Strains of Staphylococcus Aureus. *Molecules* **2016**, *21* (9), 1–18.

(122) Figueroa-Espí, V.; Alvarez-Paneque, A.; Torrens, M.; Otero-González, A. J.; Reguera, E. Conjugation of Manganese Ferrite Nanoparticles to an Anti Sticholysin Monoclonal Antibody and Conjugate Applications. *Colloids Surfaces A Physicochem. Eng. Asp.* **2011**, *387* (1–3), 118–124.

(123) Xie, Y.; Kang, R.; Tang, D. Assessment of Posttranslational Modifications of ATG Proteins. *Methods Enzymol.* **2017**, *587*, 171–188.

(124) Bier, M.; Palusinski, O. A.; Mosher, R. A.; Saville, D. A. Electrophoresis: Mathematical Modeling and Computer Simulation. *Science* **1983**, *219* (4590), 1281–1287.

(125) Garfin, D. E. One-Dimensional Gel Electrophoresis. In *Methods in Enzymology*; Academic Press, **2009**; Vol. 463, pp 497–513.

(126) Morgan, E. Chemometrics: Experimental Design. *J. Chemom.* **1996**, *10* (4), 349–349.

(127) Montgomery, D. C. *Diseño y Análisis de Experimentos*; Limusa Wiley, **2003**.

(128) Martínez-Mera, I.; Espinosa-Pesqueira, M. E.; Pérez-Hernández, R.; Arenas-Alatorre, J. Synthesis of Magnetite

(Fe_3O_4) Nanoparticles without Surfactants at Room Temperature. *Mater. Lett.* **2007**, *61* (23–24), 4447–4451.

(129) International Centre for Diffraction Data (ICDD). Powder Diffraction File (PDF) No. 88-0315, 2002. ICDD **2002**.

(130) Khalil, M. I. Co-Precipitation in Aqueous Solution Synthesis of Magnetite Nanoparticles Using Iron(III) Salts as Precursors. *Arab. J. Chem.* **2015**, *8* (2), 279–284.

(131) Ma, M.; Zhang, Y.; Yu, W. Preparation and Characterization of Magnetite Nanoparticles Coated by Amino Silane. *A Physicochem. Eng. Asp.* **2003**, *212*, 219–226.

(132) Petcharoen, K.; Sirivat, A. Synthesis and Characterization of Magnetite Nanoparticles via the Chemical Co-Precipitation Method. *Mater. Sci. Eng. B Solid-State Mater. Adv. Technol.* **2012**, *177*, 421–427.

(133) Yang, K.; Peng, H.; Wen, Y.; Li, N. Re-Examination of Characteristic FTIR Spectrum of Secondary Layer in Bilayer Oleic Acid-Coated Fe_3O_4 Nanoparticles. *Appl. Surf. Sci.* **2010**, *256* (10), 3093–3097.

(134) Hay, M. B.; Myneni, S. C. B. Structural Environments of Carboxyl Groups in Natural Organic Molecules from Terrestrial Systems. Part 1: Infrared Spectroscopy. *Geochim. Cosmochim. Acta* **2007**, *71*, 3518–3532.

(135) Dreyer, D. R.; Miller, D. J.; Freeman, B. D.; Paul, D. R.; Bielawski, C. W. Elucidating the Structure of Poly(Dopamine). *Langmuir* **2012**, *28*, 6428–6435.

(136) Fernandes Queiroz, M.; Melo, K.; Sabry, D.; Sassaki, G.; Rocha, H. Does the Use of Chitosan Contribute to Oxalate Kidney Stone Formation? *Mar. Drugs* **2014**, *13* (1), 141–158.

(137) Chang, S.; Lin, K.-Y. A.; Lu, C. Efficient Adsorptive Removal of Tetramethylammonium Hydroxide (TMAH) from Water Using Graphene Oxide. *Sep. Purif. Technol.* **2014**, *133*, 99–107.

(138) Lee, Y.; Ryou, M.-H.; Seo, M.; Choi, J. W.; Lee, Y. M. Effect of Polydopamine Surface Coating on Polyethylene Separators as a Function of Their Porosity for High-Power Li-Ion Batteries. *Electrochim. Acta* **2013**, *113*, 433–438.

XI JORNADAS DE JÓVENES INVESTIGADORES EN FÍSICA ATÓMICA Y MOLECULAR

CÁDIZ, DEL 26 AL 29 DE MARZO DE 2019 / CÁDIZ, FROM 26TH TO 29TH MARCH 2019

XI Jornadas de Jóvenes Investigadores en Física Atómica y Molecular
Programa de conferencias

Martes, 26 de marzo

14:00 – 15:30	**Recepción de participantes**
15:30 – 16:00	**Inauguración de las XI J²IFAM**
16:00 – 17:00 | KT1	*Keynote Talk – A look at half a century of theoretical calculations of molecular properties: from HMOs to DFT* **Manuel Fernández Núñez (Universidad de Cádiz)** Catedrático de Química Física
17:00 – 17:30	**Sesión de pósteres & coffee-break**
17:30 – 18:50	**Sesión 01 | FQ Teórica & FQ Nuclear | Chairman: Iván Carrillo Berdugo**
17:30 – 17:50 | C01	*Correlation between new models for the calculation of reactivity indices in the conceptual DFT framework* Jesús Sánchez Márquez (Universidad de Cádiz)
17:50 – 18:10 | C02	*A novel SBO basis set for the theoretical calculation of physicochemical properties in large scale systems* Víctor García Hernández (Universidad de Cádiz)
18:10 – 18:30 | C03	*Structural and optoelectronic properties of lead chalcogenide nanoparticles including spin-orbit coupling and dispersion forces effects* Javier Amaya Suárez (Universidad de Sevilla)
18:30 – 18:50 | C04	*TRITIUM: A real-time tritium monitor system for water quality assessment* Marcos Martínez Roig (IFIC, Universidad de Valencia-CSIC)

XI Jornadas de Jóvenes Investigadores en Física Atómica y Molecular
Programa de conferencias

Miércoles, 27 de marzo

10:00 – 10:40 | IS1	*Invited Speech – Biomolecules and Interstellar molecules: Structure, Interactions and Spectroscopic Characterization* **Elena Alonso Alonso (Universidad de Valladolid)** Premio GEFAM 2018 a la mejor tesis doctoral en Química Física Atómica y Molecular
10:40 – 11:40	**Sesión 02 | Espectroscopia (I) | Chairman: Roberto Gómez Villarejo**
10:40 – 11:00 | C05	*Circumstellar discs: an approach to their understanding via IR excesses* Nuria Fonseca Bonilla (Centro de Astrobiología, CSIC-INTA)
11:00 – 11:20 | C06	*Exploring hydrogen bonding in aromatic alcohols by mass-resolved excitation spectroscopy* Ander Camiruaga Leza (Universidad del País Vasco)
11:20 – 11:40 | C07	*Angle-resolved X-ray photoelectron spectroscopy on a (100)-oriented H-terminated diamond* Gonzalo Alba Muñoz (Universidad de Cádiz)
11:40 – 12:10	**Sesión de pósteres & coffee-break**
12:10 – 13:30	**Sesión 03 | Espectroscopia (II) | Chairman: Roberto Gómez Villarejo**
12:10 – 12:30 | C08	*Spectroscopy method and electrochemical sensor for detection of alpha amylase and glucosidase inhibition by medicinal plants* Dounia El Fadil (Universidad de Hassan II)
12:30 – 12:50 | C09	*High adsorption performance of Mo-Cu co-doped TiO_2 for the removal of organic pollutants from wastewater* Sara Chahid (Universidad de Cádiz)
12:50 – 13:10 | C10	*Cesium role as structural stabilizer in triple cation perovskite solar cells* Marta Barea Sepúlveda (Universidad de Cádiz)
13:30 – 15:30	**Almuerzo**
15:30 – 16:10	**Sesión 04 | Espectroscopia (III) & Biomoléculas | Chairman: Paloma Martínez Merino**
15:30 – 15:50 | C11	*Application of Raman spectroscopy and a "second-order lumped parameter mathematical model" for estimating temperature in active layer of DSSC.* Juan Jesús Gallardo Bernal (Universidad de Cádiz)
15:50 – 16:10 | C12	*MALDI Imaging Mass Spectrometry profiling of Proteins and Lipids on the same tissue* Lucía Martín Saiz (Universidad del País Vasco)
17:30 – 19:00	**Visita cultural por el Casco Antiguo de Cádiz** con punto de partida en Plaza España

XI Jornadas de Jóvenes Investigadores en Física Atómica y Molecular
Programa de conferencias

Jueves, 28 de marzo

10:00 – 10:40 | IS2	*Invited Speech – Molecular Dynamics of aqueous $[UO_2]^{2+}$ diffusion and free energy in clays* **Sergio Pérez Conesa (Universidad de Sevilla)** Premio GEFAM 2017 al mejor artículo de un investigador joven en Química Física Atómica y Molecular
10:40 – 11:40	**Sesión 05 | Mod. Computacional & Info. Cuántica | Chairman: Estefanía Torres Ávila**
10:40 – 11:00 | C13	*DFT investigation of Cathode Materials for rechargeable Ca Batteries* Arturo Torres Gutiérrez (Universidad Complutense de Madrid)
11:00 – 11:20 | C14	*Drag reduction in the flow around a cylinder: A Bayesian optimization approach* Anthony Larroque (Universidad de Cádiz)
11:20 – 11:40 | C15	*Complexity measures for a confined hydrogen atom* Milagros F. Morcillo Arencibia (Universidad de Córdoba)
11:40 – 12:10	**Sesión de pósteres & coffee-break**
12:10 – 13:10	**Sesión 06 | Clústeres y Nanoestructuras (I) | Chairman: Estefanía Torres Ávila**
12:10 – 12:30 | C16	*Analysis of hydrogen spillover from Pd clusters onto Graphene* Alejandra Granja del Río (Universidad de Valladolid)
12:30 – 12:50 | C17	*Novel ultrasound Synthesis of Magnetic Nanoparticles optimized through design of experiments* Christian H. Pérez Beltrán (Universidad de Cádiz)
12:50 – 13:10 | C18	*Combination of magnetic molecularly imprinted polymers with UV-Vis Spectrophotometry for the selective and sensitive determination of sulfonamide* Abderrahman Lamaoui (Universidad de Cádiz)

13:30 – 15:30	**Almuerzo**
15:30 – 16:10 | IS3	*Invited Speech – Tuning the formation of MoS_2 nanosheets/nanowire to prepare nanofluids with enhanced thermal properties for use in Concentrating Solar Power* **Paloma Martínez Merino (Universidad de Cádiz)** Premio GEFAM 2018 al mejor artículo de un investigador joven en Química Física Atómica y Molecular
16:10 – 16:50	**Sesión 07 | Clústeres y Nanoestructuras (II) | Chairman: Paloma Martínez Merino**
16:10 – 16:30 | C19	*2D $MoSe_2$-based nanofluids prepared with interesting applications for Concentrated Solar Power* Miriam Teruel Sibón (Universidad de Cádiz)
16:30 – 16:50 | C20	*Nanofluids for Concentrated Solar Power* Francisco Javier Navas Pineda (Universidad de Cádiz)
16:50 – 17:20	**Sesión de pósteres & coffee-break**
17:20 – 18:00	**Sesión 08 | Clústeres y Nanoestructuras (III) | Chairman: Paloma Martínez Merino**
17:20 – 17:40 | C21	*Recent advances in the modification of electrochemical biosensors by using nanomaterials* Juan José García Guzmán (Universidad de Cádiz)
17:40 – 18:00 | C22	*Alignment as a key factor for the development of scaffolds with potential application in Tissue Engineering* Víctor Manuel Pérez Puyana (Universidad de Sevilla)
22:00 – (···)	**Cena de gala**

XI Jornadas de Jóvenes Investigadores en Física Atómica y Molecular
Programa de conferencias

Viernes, 29 de marzo

10:00 – 11:00 | KT2	*Keynote Talk – Modelling and simulation of materials, what can we do?* **Norge Cruz Hernández (Universidad de Sevilla)** Profesor Titular de Física Aplicada
11:00 – 12:00	**Sesión 09 | Fotónica y Optoelectrónica & Femtoquímica y Control Láser | Chairman: Teresa Aguilar Sánchez**
11:00 – 11:20 | C23	*Lorenz-Haken laser dynamics in nanophotonic devices* Luis Cerdán Pedraza (IQFR-CSIC)
11:20 – 11:40 | C24	*Ultrafast Evolution of Azaindoles after Electronic Excitation* Iker Lamas Frejo (Universidad del País Vasco)
11:40 – 12:00 | C25	*Femtosecond predissociation dynamics of ethyl iodide in the B band* Marta Murillo Sánchez (Universidad Complutense de Madrid)
12:00 – 12:30	**Sesión de pósteres & coffee-break**
12:30 – 13:30	**Sesión 10 | Catálisis & Superficies | Chairman: Teresa Aguilar Sánchez**
12:30 – 12:50 | C26	*Construction of electrochemical immunosensors based on polypyrrol for food control* Narjiss Seddaoui (Universidad de Hassan II)
12:50 – 13:10 | C27	*CO_2 Activation on Cu/TiO_2 Surfaces Promoted by Potassium* Elena Rodríguez Remesal (Universidad de Sevilla)
13:10 – 13:30 | C28	*Visible light photodegradation of organic compounds with cesium tin halide perovskite* Francisco José Reyes Pérez (Universidad de Cádiz)
13:30 – 13:40	**Receso**
13:40 – 14:00	**Entrega de premios y clausura de las XI J²IFAM**

Novel ultrasound synthesis of magnetite-based nanoparticles optimized through experimental design

Christian Pérez[a], Juan José García Guzmán[a], Osvaldo L. Estévez Hernández[b], David López Iglesias[a], Laura Cubillana Aguilera[a], José María Palacios Santander[a]

[a]Institute of Research on Electron Microscopy and Materials (IMEYMAT), Department of Analytical Chemistry, Faculty of Sciences, Campus de Excelencia Internacional del Mar (CEIMAR), University of Cadiz, Campus Universitario de Puerto Real, Polígono del Río San Pedro, S/N, 11510 Puerto Real, Cadiz, Spain

[b]Instituto de Ciencia y Tecnología de Materiales (IMRE), Universidad de La Habana, Zapata y G, Vedado, 10400, La Habana, Cuba

Magnetic nanoparticles (MNPs) have been widely studied for a very long time, leading to know their importance and potential applications in many fields due to their special properties such as superparamagnetic, high field irreversibility, high saturation field, extra anisotropy contributions or shifted loops after field cooling, biocompatibility, long durability, low toxicity and cost [1-2].

All these properties have promoted their use in magnetic recording media, ferrofluids, magnetic resonance imaging, heavy metals ions removal and biomedicine (specifically in the hyperthermic treatment of malignant cells, site-specific drug delivery and separation of proteins and cell population [3]). Among the techniques employed for the synthesis of magnetite the most common are chemical vapor deposition, thermal oxidation, polyol process, iron salts co-precipitation, hydrothermal and solvothermal methods [4-5]. Co-precipitation is the most usual way for magnetite production due to its simplicity, low cost, high yield and efficiency. However, it presents some difficulties, such as the particle size control, broad size distribution, high time consuming and the non-unique nanoparticle phases obtained, which can be ferrihydrite, akagenite (FeOOH), Fe(OH), hematite or maghemite.

On the other hand, the use of high power ultrasound has gained much attraction for many applications [6], especially in the sonochemical syntheses. Through using this green approach, a more uniform size distribution can be achieved, as well as, higher surface area and improved phase purity.

Therefore, this study is focused on the synthesis via co-precipitation method of magnetic nanoparticles by using a high power sonochemical approach, where MNPs of about 13 nm are obtained within one minute with all its enhanced characteristics.

Experimental design has been used in order to optimize the preparation process from hours to just one single minute. The composition, structure, size and morphology analyses of these MNPs have been carried out through X-ray diffraction, Fourier transform infrared spectroscopy, thermogravimetric analysis and scanning electron microscopy showing the correct achievement of the desired MNPs. Moreover, different coating agents have been tested in order to functionalize MNPs surface. The attachment of the enzyme horse radish peroxidase and of the antibody against a suppressor protein is tested and evaluated to detect mercury on water and to detect TRIB2.

References

[1] X. Batlle, A. Labarta, J. Phys. D: *Appl. Phys*. **35** (2002) R15-R42.

[2] L. Cabrera, S. Gutiérrez, N. Menéndez, M. P. Morales, P. Herrasti, *Electrochim. Acta* **53** (2008) 3436-3441.

[3] H. Gu, K. Xu, C. Xu, B. Xu, *Chem. Commun*. (2006) 941-949.

[4] A.E. Regazzoni, G.A. Urrutia, M.A. Blesa, A.J.G. Maroto, *J. Inorg. Nucl. Chem.* **43** (1981) 1489-1493.

[5] W.S. Peternele, V.M. Fuentes, M.L. Fascineli, J. Rodrigues, R. Carvalho, C. Madeira, R. Bentes, *J. Nanomater.* **2014** (2014) 1-10.

[6] R.J. González-Álvarez, I. Naranjo-Rodríguez, M.P. Hernández-Artiga, J.M. Palacios-Santander, L. Cubillana-Aguilera, D. Bellido-Milla, *J. Sol-Gel Sci. Technol* **80** (2016) 378-388.